Alma Mater Studiorum - Università di Bologna

DOTTORATO DI RICERCA IN

INGEGNERIA ELETTRONICA, TELECOMUNICAZIONI E TECNOLOGIE DELL'INFORMAZIONE

Ciclo 34

Settore Concorsuale: 09/F2 - TELECOMUNICAZIONI

Settore Scientifico Disciplinare: ING-INF/03 - TELECOMUNICAZIONI

ENABLING 5G AND BEYOND: MILLIMETER WAVE PROPAGATION AND CLOUD RAN EVOLUTION

Presentata da: Leonardo Possenti

Coordinatore Dottorato	**Supervisore**
Aldo Romani	Alessandro Vanelli Coralli

Esame finale anno 2022

Abstract

In the last few years, mobile wireless technology has gone through a revolutionary change. Web-enabled devices have evolved into essential tools for communication, information, and entertainment. The fifth generation (5G) of mobile communication networks is envisioned to be a key enabler of the next upcoming wireless revolution. Millimeter wave (mmWave) spectrum and the evolution of Cloud Radio Access Networks (C-RANs) are two of the main technological innovations of 5G wireless systems and beyond. Because of the current spectrum-shortage condition, mmWaves have been proposed for the next generation systems, providing larger bandwidths and higher data rates. Consequently, new radio channel models are being developed. Recently, deterministic ray-based models such as Ray-Tracing (RT) are getting more attractive thanks to their frequency-agility and reliable predictions. A modern RT software has been calibrated and used to analyze the mmWave channel. Knowledge of the electromagnetic properties of materials is therefore essential. Hence, an item-level electromagnetic characterization of common construction materials has been successfully achieved to obtain information about their complex relative permittivity. A complete tuning of the RT tool has been performed against indoor and outdoor measurement campaigns at 27 and 38 GHz, setting the basis for the future development of advanced beamforming techniques which rely on deterministic propagation models (as RT). C-RAN is a novel mobile network architecture which can address a number of challenges that network operators are facing in order to meet the continuous customers' demands. C-RANs have already been adopted in advanced 4G deployments; however, there are still some issues to deal with, especially considering the bandwidth requirements set by the forthcoming 5G systems. Open RAN specifications have been proposed to overcome the new 5G challenges set on C-RAN architectures, including synchronization aspects. In this work it is described an FPGA implementation of the Synchronization Plane for an O-RAN-compliant radio system.

Contents

List of Figures

List of Tables

Introduction

Over the past decades the demand for higher data rates has been continuously growing to satisfy users' desire for a faster, safer and more reliable wireless network. Wireless communications went through a great progress in the improvement of telecommunication systems, from analog to digital systems, from circuit-switched to packet-switched networks, from limited to very evolved services. Starting from the early 1980s, wireless and mobile communications begun their relentless evolution which led to the present day a cutting edge technology. In forty years, four generations of mobile communications took place where each generation has been motivated by the need to address the challenges not overcome by its predecessor. Although this evolution has been continuous, approximately every ten years a new generation of mobile technology was introduced that delivers a big leap in performance, efficiency and capability.

The current fourth generation LTE technology, initiated in 2010 following in the steps of HSPA provided faster and better mobile broadband. LTE has continued to evolve since then, bringing new technology inventions such as MIMO, carrier aggregation, and higher-order modulation to deliver blazing-fast wireless performance, as well as solutions to efficiently grow network capacity to address the surge in data traffic which has grown over 4,000 times in the past 10 years.

The availability of a such advanced architecture has dramatically increased the number of services and applications requiring network coverage. The huge growth in the number and variety of connected devices, the substantial increase in user traffic volume along with the performance limitations of LTE have motivated research and industry toward defining, developing, and deploying systems for a fifth generation (5G) of mobile networks. The forthcoming 5G technology has to face new arising challenges, which can be condensed into three main aspects: the massive growth in the number of connected devices, the massive growth in traffic volume and the wide range of applications with diverse quality of service. The various types of devices and applications need more sophisticated networks that not only can support high throughput, but also provide low latency in data delivery, efficient energy consumption scheme, high scalability to accommodate a large number of devices, ubiquitous connectivity for users, improved reliability for services and improved devices' security. In this scenario, a significant paradigm shift is required to further enhance wireless communication networks, in order to overcome the actual spectrum-shortage situation, which makes it difficult to improve performance.

For the above reasons, exploitation of millimeter wave (mmWave) frequencies for 5G standards has started to gain considerable attraction within the wireless industry and academia. This is because mmWave frequency bands can provide greater bandwidths than current cellular allocations and therefore, a significant increase in achievable data rates. However, even though mmWave systems have many benefits based on the ultrawide bandwidths, the propagation of mmWave wireless links is highly directional and is also highly attenuated due to its high carrier frequency. Recent trends have encouraged the consideration of the viability of mmWave cellular systems, especially for multiantenna systems. In fact, at these higher frequencies, due to the very small wavelengths, large-scale antenna arrays can be deployed - especially at the base stations - leading to the design of massive MIMO (mMIMO) systems, which are envisioned to be key enablers for 5G systems. To overcome the mmWave coverage challenge, advanced beamforming with very narrow beams can be used to address much of the path loss associated with mmWave. In particular, analog beamforming is expected to be a key solution for 5G systems.

Moreover, since the propagation at mmWaves is naturally affected by physics that reduces coverage to shorter ranges, network densification is a direct consequence of the choice of higher frequencies and will lead to a tremendous increase in capacity over the covered area. For this reason, already starting from LTE systems, cellular networks have been evolving towards smaller radii, in particular with support for pico- and femto-cell heterogeneous networks. The primary challenge of network densification is the increase in costs and consumptions, as mobile operators must deploy many more mmWave small cells than LTE in order to achieve similar wide-area coverage. In view of this, traditional Radio Access Networks (RANs) evolved towards a centralized architecture. With the advantages in softwarization and virtualization, Cloud RAN have become an essential component in wireless systems architecture. However, with the forthcoming 5G technology, current Cloud RAN are facing a problem of higher bandwidth requirements at their interfaces, which are not affordable anymore. New advanced “Open” RAN specifications have been proposed to overcome the bandwidth problem and to enable multi-vendor RAN, that is the possibility to connect different network components coming from different vendors.

The present thesis is the result of a three-years high apprenticeship PhD program at TEKO Telecom company, part of the JMA group, in collaboration with the University of Bologna. This work will focus on these two aspects of 5G systems: the exploitation of mmWave spectrum in the first part and the further RAN’s evolution in the second part. In order to track the logic progression of the thesis everything is organized as follows. The introduction is followed by a first part targeting the adoption of the new mmWave spectrum.

Chapter 1 outlines the background in which 5G emerges, the main motivations which led to its development along with the ITU activity on standardization and the minimum performance requirements that it is expected to satisfy. Here, it is given a brief overview of the main physical layer elements and a quick focus on multiantenna techniques which are envisioned to be extensively exploited in 5G systems. Finally, the main challenges that 5G has to face are highlighted, leading to the main topic of the next chapter.

Chapter 2 introduces the mmWave spectrum with its particular propagation characteristics and benefits. Since the propagation characteristics differ a lot from those at traditional sub-6 GHz frequencies, it is important to develop new channel models which incorporate the new features. Hence, this chapter includes a brief history, previous and current work in literature on radio channel modelling in view of 5G systems focusing on map-based models, projected to be widely used in mmWave channels.

Chapter 3 describes a new method for the evaluation of electromagnetic characteristics of materials. The knowledge of the electromagnetic properties of construction materials is crucial for the design of future wireless systems, especially in relation to the map-based propagation models and tools for radio channel characterization in 5G and beyond systems. Such models are based on both geometric and electromagnetic description of the environment, therefore the evaluation of the electromagnetic properties of materials is essential. Here, it is presented the development of the method, its validation in terms of precision and accuracy and its validation against literature. Finally, it is provided the collection of electromagnetic parameters computed at mmWave frequencies.

Chapter 4 addresses an in-depth directional analysis of a 27 GHz and 38 GHz channel, based on two measurement campaigns performed at the University of Bologna compared with Ray-Tracing simulations. Here, Ray-Tracing is used as an analysis tool in order to understand and investigate the new mmWave channel, giving an in-depth analysis of the principal propagation mechanisms involved. This work provides an essential starting point to evaluate Ray-Tracing as a prediction channel tool to assist future beamforming techniques, which the forthcoming 5G systems are envisioned to rely on. In particular, the progresses of environment digitalization and localization techniques will allow the development of advanced beamforming techniques which rely on deterministic propagation models such as RT to perform real-time prediction of the channel's directional characteristics. Chapter 4 also concludes the first part of this work.

The next part accounts the evolution of RAN architectures and the adoption of the Open RAN specification for the new 5G RANs. Chapter 5 provides an overview of the evolution of radio access networks, highlighting the challenges of current architectures, due to the strict requirements set by the forthcoming 5G systems. This leads to the new concept of functional split, which is described in this chapter. The heterogeneous situation resulted from the definition of a number of functional split options by different organizations, along with the current CPRI-based Cloud RANs limitations, creates a need for interoperability, which sets the basis for the work of the next final chapter.

Chapter 6 addresses the FPGA project on the synchronization plane for an O-RAN-compliant Remote Unit. After a brief overview of the O-RAN specification, it is described the problem of synchronization in packet-switched networks and the consequent adoption of the Precision Time Protocol (PTP), also described in this chapter. The new proposed O-RAN specifications set a specific framework to provide time and frequency synchronization in new 5G RANs, which is considered in the project.

Each chapter begins with a very brief description of the discussed topics.

Part I

Millimeter wave propagation characterization

Chapter 1

A new radio access technology

In this chapter it is outlined the background in which 5G emerges and the main motivations which led to its development. Here, it is also presented the ITU activity on 5G standardization, its vision and the minimum performance requirements that the new technology is expected to satisfy. In order to give and idea of how such requirements are met, it is given a brief overview of the main physical layer elements. A quick focus on multiantenna techniques is done, since 5G will extensively based on these. To conclude, the main challenges that 5G has to face are highlighted, leading to the main topic of the next chapter.

1.1 Contex and background

Mobile devices have become a fixture of every-day life for millions of people. Across the globe, web-enabled devices such as smartphones and tablets have evolved into essential tools for communication, information, and entertainment alike. Wireless traffic demand is growing extremely rapidly due to new services such as Ultra-High Definition videos, virtual and augmented reality, cloud gaming, smart cities, etc. and an increase of 1000-fold of the wireless traffic is expected [1][2][3]. The resulting demand for higher mobile network performances, in terms of data rates, latency, and reliability has created a bottleneck in current spectrum utilization which makes it difficult to enhance performance in the limited available bandwidth [4][5]. Moreover, current 4G LTE technology, which nowadays has reached a very mature state, has to deal with new arising challenges which might be summarized into three main aspects: the massive growth in the number of connected devices; the massive growth in traffic volume; the wide range of applications requiring different quality of service.

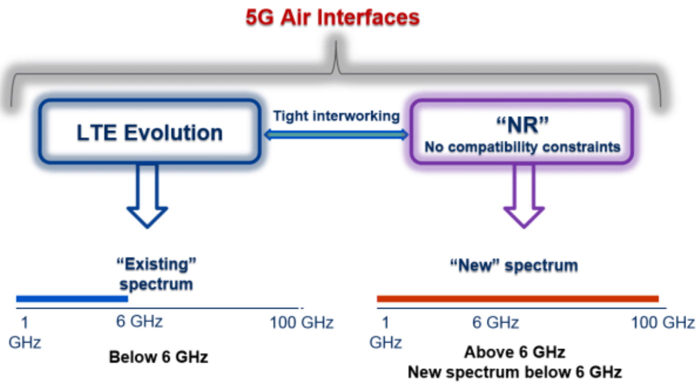

Figure 1.1: 5G NR wireless access vision [6]

Such context has motivated research and industry efforts - and investments - toward defining, developing, and deploying systems for the fifth generation (5G) of mobile networks. In particular, it is required a significant paradigm shift to further improve current wireless communication technologies. Currently, the progresses in wireless communications go towards two main directions: on one hand the evolution of today's 4G LTE networks; on the other the addition of a new, globally standardized, radio access technology: the 5G New Radio (NR). 5G NR is expected to reuse many of the structures and features of LTE, which is currently evolved into a very capable and refined technology. However, being a *New Radio* technology means that NR, unlike the LTE evolution, is not restricted by a need to retain backwards compatibility. The vision of 5G wireless access is shown in Fig. 1.1 and it will comprise both 5G NR development and LTE evolution. LTE is continuously evolving to meet a growing part of the 5G requirements. Such evolution of LTE towards 5G is referred to as the *LTE Evolution* [6]. In Fig. 1.1 it is also pointed out that - in order to serve more users with such improved performances - along with a more efficient exploitation of current spectrum, new spectrum resources are required to be allocated.

1.2 Standardization for 5G NR

Like previous generations of cellular systems, the development of 5G NR is a coordinated, global effort based on the requirements defined by the International Telecommunication Union (ITU) through the International Mobile Telecommunications (IMT) documents. The IMTs are not specific technologies, but rather specifications and requirements for high-speed mobile broadband services. ITU defines the process of evaluation of which proposed candidate technologies meet the IMT criteria and the subsequent selection as a standardized mobile technology. The ITU Radiocommunication Sector (ITU-R), which regulates the international radio frequency spectrum, is responsible to turn technical specifications from standardization bodies, e.g. 3GPP, into global standards. ITU-R identifies, in the Recommendation ITU-R M.2083, the framework and the overall objectives of development of IMT for 2020 and beyond (IMT-2020) [7]. The IMT-2020 systems are envisioned as mobile systems that include new radio interfaces which support the new capabilities of systems beyond IMT-2000 (3G systems) and IMT-Advanced (4G systems).

The ITU-R activities on IMT-2020 started with the development of the framework and the objectives presented in the Recommendation ITU-R M.2083. This was followed by the definition of more detailed requirements for IMT-2020 that candidate technologies must fulfill. With the requirements finalized, candidate technologies can be submitted to ITU-R. The proposed candidate technologies will be evaluated against the IMT-2020 requirements and those that fulfill the requirements will be approved and published as part of the IMT-2020 specifications. ITU-R M.2412-0 report [8] provides the guidelines for the procedure, the methodology and the criteria (technical, spectrum and service) to be used in evaluating the candidate IMT-2020 radio interface technologies for a number of test environments. As mentioned above, ITU-R does not produce the detailed technical specifications but defines IMTs in cooperation with regional standardization bodies. The actual technology is developed by others and submitted to ITU-R as a candidate IMT technology.

The standardization work for 5G NR started with a study item phase in Release 14 by the 3rd Generation Partnership Project (3GPP) and continued with development of a first set of specifications through a work item in Release 15 with the aim of making it commercially available before 2021. 3GPP made a first submission of NR as an IMT-2020 candidate to the ITU-R in February 2018. Unlike previous generations, for 5G it is not expected that competing technologies will be submitted as candidates for IMT-2020: only 3GPP-based technologies are anticipated.

1.2.1 IMT-2020 vision

IMT-2020 specifications can be considered from multiple perspectives, including the users, manufacturers, application developers, network operators, and service and content providers. Therefore, technologies for IMT-2020 can be applied in a variety of deployment scenarios and can support a range of environments, service capabilities, and technology options. ITU-R M.2083 [7] identifies the objectives and the capabilities of IMT-2020, aiming to make IMT-2020 more flexible, supporting the new emerging use cases, with highly complex requirements going from applications demanding very high data rate communications, to a large number of connected devices, passing through ultra-low latency and high reliability applications. The IMT-2020 vision is to embrace, next to the conventional human-centric communications, also the newest innovative machine-centric communications. The identified scenarios include three main use cases: with respect to the human-centric communications, the *Enhanced Mobile Broadband* (eMBB); in the context of machine-centric communications, the *Massive Machine Type Communications* (mMTC) and the *Ultra-Reliable and Low-Latency Communications* (URLLC). The eMBB addresses the human-centric use cases for access to improved multimedia content, services and data, coming with new application areas and requirements in addition to existing ones such as extremely high-data rate file transfers, 4K videos, work and play in cloud, augmented reality and so on. The eMBB use case covers a range of scenarios including hotspot connectivity - characterized by a high user density and extremely high data rates, and low mobility - and wide-area coverage, where the user density and data rates are lower, but the mobility is higher. The URLLC scenario has stringent requirements for both latency and reliability. Some examples include wireless control of industrial manufacturing or production processes, remote medical surgery, distribution automation in a smart grid, transportation safety, vehicular automation, mission critical services, self driving cars, etc. The mMTC use case, especially driven by the growth of Internet of Things (IoT), corresponds to services that are characterized by a very large number of connected devices, typically transmitting a relatively low volume of non-delay sensitive data, such as remote sensors, actuators, monitoring equipment, smart city cameras, voice services, sensor networks, etc. Typically, such devices are low cost, and have a very long battery life. The mMTC devices are expected to have a very long battery lifetime and they will be extremely heterogeneous in terms of capabilities, cost, energy consumption, and transmission power. The classification of 5G use cases into these three distinctive classes is primarily aiming to simplify the definition of requirements for the technology specification which, as stated before, can be also very contraddictory. Of course, there will be use cases that may not exactly fit into one of these classes: there may be services that require very high reliability but for which the latency requirements are not that critical; use cases requiring devices of very low cost but where the possibility for very long device battery life may be less important.

1.2.2 IMT-2020 minimum technical performances

Different usage scenarios along with the current and future trends will result in a great variety of requirements. In M.2410-0 report [9], ITU-R defines a set of capabilities needed for an IMT-2020 technology to support the 5G use cases and usage scenarios. The ITU-R M.2410-0 report describes the key requirements related to the minimum technical performance of IMT-2020 which the future 5G technologies are required to satisfy. Such technical requirements are for the purpose of consistent definition, specification, and evaluation of the candidate

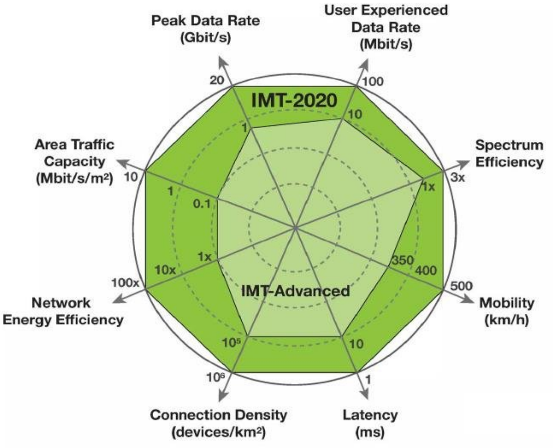

Figure 1.2: Enhancement of key capabilities from IMT-Advanced to IMT-2020 [7]

IMT-2020 radio interface technologies. The intent of these requirements is to ensure that IMT-2020 technologies are able to fulfill the objectives of IMT-2020 and to set a specific level of performance that each proposed technology needs to achieve in order to be considered by ITU-R for IMT-2020. Of course, the key capabilities will have different relevance and applicability for the different usage scenarios addressed by IMT-2020. There are a total of 13 capabilities defined in [9], where eight were selected as *key capabilities*, which are outlined in Table 1.1 and compared with those of 4G LTE technology in Fig. 1.2. Next to these eight key capabilities it is also set the requirement for *Reliability* for the purpose of evaluation in the URLLC scenario. The minimum requirement is $1 - 10^{-5}$ success probability “of transmitting a layer 2 protocol data unit of 32 bytes within 1 ms in channel quality of coverage edge for the Urban Macro-URLLC test environment”, as defined by ITU-T in [9]. Fig. 1.3 shows the importance of each key capability for the usage scenarios.

1.3 5G radio protocol stack overview

The 5G System (5GS) is composed by three macro elements as sketched in Fig. 1.4:

- 5G NR Core Network (CN), responsible for authentication, charging functionality, setup of end-to-end connections and provide services to UEs (*network slicing*)
- 5G NR Radio Access Network (RAN), responsible for all radio-related functionalities of the overall network including scheduling, radio-resource

Table 1.1: Key performance indicator of IMT-2020

KPI		**Use case**	**Values**
Peak data rate		eMMB	DL: 20 Gbps, UL: 10 Gbps
User experience data rate		eMMB	DL: 100 Mbps, UL: 50 Mbps
Latency	User plane	eMMB/URLLC	4 ms/1 ms
	Control plane	eMMB/URLLC	20 ms
Mobility		eMMB	Up to 500 km/h
Connection density		mMTC	$1,000,000$ devices/km^2
Energy efficiency		eMMB	3x IMT-Advanced [10]
Spectrum efficiency		eMMB	3x IMT-Advanced [10]
Area traffic capacity		eMMB	DL: 10 Mbps/m^2

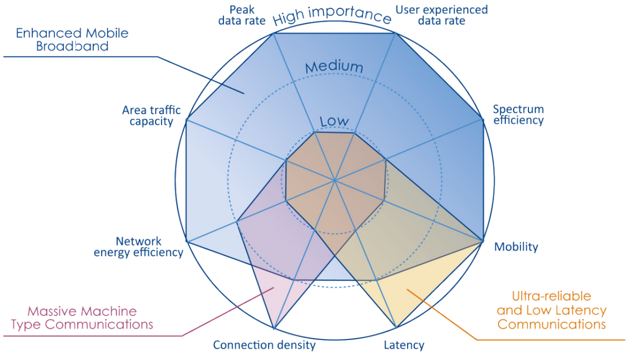

Figure 1.3: Key performance indicator in different usage scenario [7]

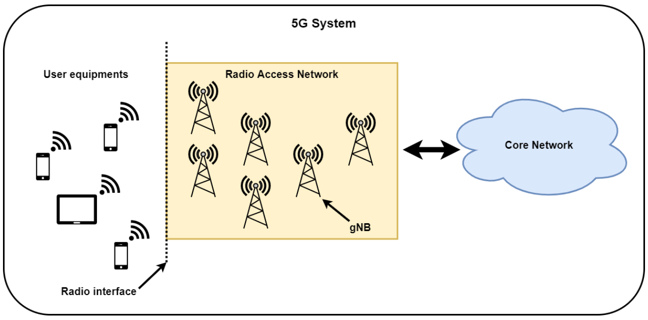

Figure 1.4: 5G system components

handling, retransmission protocols, coding, radio resource management, admission control, connection establishment, and various multi-antenna schemes;

- User Equipments (UEs)

UEs are connected to the RAN through the radio channel, which is the subject of this work. 5G NR RAN is composed by a network of base stations named next generation Node B (gNB). A base station is not a physical unit, rather a logical entity implementing a logical radio access network node and it can be realized in different ways based on a standardized gNB protocol. The NR radio protocol architecture (which rules the transmissions through the radio channel) is split into *control-plane* architecture and *user-plane* architecture. The user-plane is responsible for transferring application data between the UE and the service provider. Fig. 1.5 illustrates the 5G user-plane protocol stack for the radio interface (called NR-Uu). The protocol is split into the following layers: Physical (PHY) layer, Medium Access Control (MAC) layer, Radio Link Control (RLC) layer, Packet Data Convergence Protocol (PDCP) layer, and Service Data Adaptation Protocol (SDAP) layer. The control-plane is mainly responsible for control signaling for connection setup, mobility, and security. Control signaling originates either from the CN or from a Radio Resource Control (RRC) layer in gNB. The RRC messages are transmitted using the same PDCP, RLC, MAC, and PHY layers as for the user-plane. Therefore, from a physical layer perspective, there is not at all a fundamental technological difference in providing services to higher layers in control-plane and user-plane protocol stacks.

1.3.1 5G physical layer elements

The physical layer forms the backbone of a mobile communication technology, responsible for coding, decoding, modulation, demodulation, multi-antenna processing, and mapping of signals to the appropriate physical time-frequency

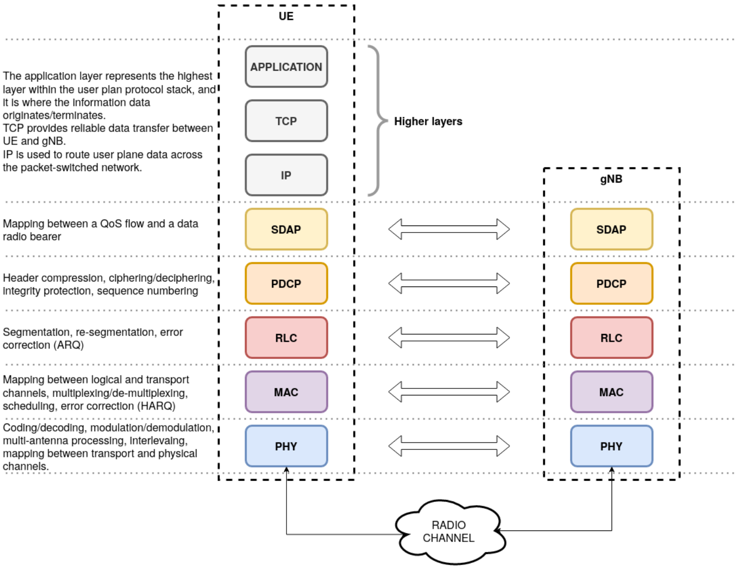

Figure 1.5: User-plane protocol stack for NR-Uu interface (assuming TCP/IP application)

resources. As mentioned in the previous sections, the NR physical layer has to support various use cases with extreme requirements on throughtput, latency and reliability. NR is also envisioned to support a very diverse spectrum, various deployment options (from pico cells to macro cells) and various link types, including downlink, uplink, sidelink and backhaul. Moreover, potential future scenarios will lead to an increased variety of such necessities. Such features have direct implications on the physical layer design, posing complex technical trade-offs. For this reason, the physical layer design leitmotiv is *flexibility* [11]. As a matter of facts, to successfully address all these challenges, 3GPP is developing a flexible and scalable physical layer for NR aiming an unified, more capable air interface. In the first release of 5G (3GPP Release 15) there are defined two frequency ranges [12]:

- **FR-1**: 450 MHz – 6 GHz (sub-6 GHz spectrum)

- **FR-2**: 24.25 GHz – 52.6 GHz (millimeter wave spectrum)

In the Technical Specifications 38.101-1 [12] and 38.101-2 [13] are also defined all the operating bands along with the relative duplex mode and channel bandwidths for FR-1 and FR-2 respectively. In the following, the key technology components of the 5G NR physical layer [14] are outlined, with considerations on flexibility and scalability.

Waveform

NR employs Cyclic Prefix OFDM (CP-OFDM, [15]) in both uplink and downlink up to at least 52.6 GHz [14]. Having the same waveform in both directions simplifies the overall design. Additionally, there is an option for DFT-spread OFDM (DFTS-OFDM) in uplink for coverage-limited scenarios, with single stream transmissions [16]. The CP-OFDM has been assessed against other relevant waveforms, resulting as an excellent choice for 5G NR [17].

Modulation

NR supports Quadrature Phase Shift Keying (QPSK), 16 Quadrature Amplitude Modulation (QAM), 64 QAM and 256 QAM modulation formats for both uplink and downlink. Moreover, $\pi/2$-BPSK is supported in uplink to enable a further reduced peak-to-average power ratio and enhanced power amplifier efficiency at lower data rates, which is important for mMTC services. Since NR will cover a wide range of use cases, it is likely that the set of supported modulation schemes may be expanded. For example, 1024 QAM may become part of the NR specification, since fixed point-to-point backhaul already uses modulation orders higher than 256 QAM.

Numerology

The numerology defines the OFDM frequency domain subcarrier spacing. NR has a scalable numerology to enable diverse services on a wide range of frequencies and deployments. The subcarrier spacing is scalable and specified as $15 \cdot 2^n$ kHz, where n is an integer and 15 kHz is the subcarrier spacing used in LTE. Different numerologies are specified for different frequency bands. The choice of the numerology depends on various factors such as the type of deployment, carrier frequency, service requirements, mobility and hardware impairments [18] [17]. For example, large subcarrier spacing is preferable for URLLC applications due to the smaller symbol time. It is also better for highly mobile users because of the robustness against Doppler spread. On the other hand, small subcarrier spacing is more convenient for supporting massive connectivity which is required for mMTC scenarios and for reducing the effect of delay spread [5].

Frame structure

The NR frame structure supports TDD and FDD transmissions and operation in both the licensed and the unlicensed spectrum [12]. Physical time-frequency resources correspond to OFDM symbols and subcarriers within the OFDM symbols. The smallest physical time-frequency resource consists of one

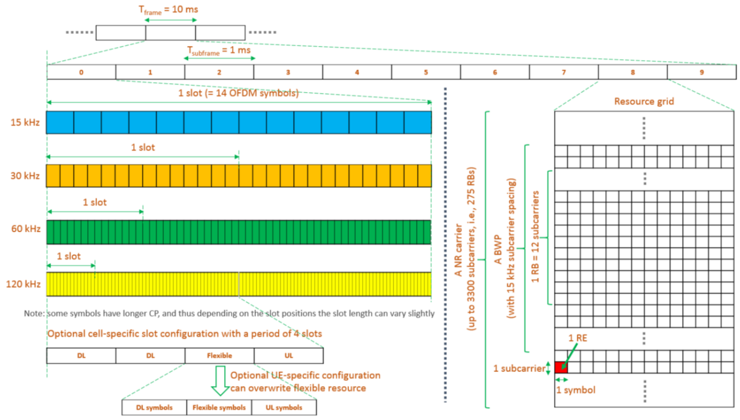

Figure 1.6: Time-frequency physical resources [19]

subcarrier in one OFDM symbol, known as a resource element. The transmissions are scheduled in group(s) of 12 subcarriers, known as Physical Resource Blocks (PRBs), as shown in Fig. 1.6 In the time domain, the radio transmissions are organized into radio *frames*, *subframes* and *slots*. As depicted in Fig. 1.6, each radio frame has a duration of 10 ms and consists of 10 subframes with a duration of 1 ms. A subframe is formed by one or multiple adjacent slots, according to the numerology, each slot having 14 adjacent OFDM symbols. The time duration of a slot scales with the chosen numerology since the duration of an OFDM symbol is inversely proportional to its subcarrier spacing. Physical layer uses time-frequency resources for transmission, representing either *physical channels* or *physical signals*. In the 3GPP terminology, a physical channel corresponds to a set of resource elements carrying information originating from higher layers, whereas a physical signals corresponds to a set of resource elements that do not contain information from higher layers. In order to support the diverse use cases also *mini-slot* structure and *slot aggregation* are considered. Mini-slots allow to support transmissions with a flexible start position and a duration shorter than a regular slot duration. They can be useful in various scenarios, including URLLC in which transmission needs to begin immediately without waiting for the start of a slot boundary, transmissions in unlicensed spectrum where it is beneficial to start transmission immediately after the listen-before-talk (LBT) mechanism and transmission in the FR-2 where the large amount of bandwidth available implies that the payload supported by a few OFDM symbols is large enough for many of the packets. In slot aggregation multiple slots can be combined for longer transmissions helping in transmission of data-heavy payloads, reducing the overhead due to switching of TDD and the transmission of reference signal and control information. This is particularly suitable for eMBB applications.

1.3.2 Multiantenna techniques

Multiantenna techniques were important already in LTE, but in NR they are expected to have a more fundamental role in the system design. Multiantenna techniques can be defined by the use of multiple antennas at the transmitter and/or receiver, usually referred to as Multiple-Input Multiple-Output (MIMO) systems, in combination with signal processing. These techniques can be used to improve the system performance in terms of throughput, coverage and reliability. Research on MIMO took place in the '90s with the works, among the others, of Foschini [20] [21], Tarokh [22] and Marzetta [23]. Today MIMO is one of the most claimed technology for wireless applications, due to its revolutionary benefits [24]. In practice, the central theme of MIMO is the smart exploitation of the radio channel characteristics to provide system benefits in terms of:

- **Channel capacity** that is the maximum achievable throughput (bps);
- **Reliability** that is the minimum probability of transmission errors (bit error rate).

The advantage of MIMO systems is that they can positively affect these two parameters without increasing neither the bandwidth nor the transmit signal power. MIMO techniques may be summarized into three main categories:

- Beamforming;
- Diversity;
- Spatial multiplexing;

Beamforming

Beamforming is a signal processing technique used to create a particular array radiation pattern, with specific shape and directionality, driving the single antenna radiating elements. Through *beamforming gain* it is possible to increase the Signal-to-Noise Ratio (SNR) and to provide additional radio link margin that mitigates propagation path loss. Moreover, beamforming provides reduced co-channel interference from the spatial selectivity of the directional beams. This is a potential for dense spatial frequency reuse, by pointing a very narrow beam (pencil-beamforming) towards the intended user. In this way, the interference to other user is kept to minimum, making multiple concurrent wireless data transfer feasible in a confined area. Beamforming provides major benefits in power-limited scenarios, increasing the SNR and allowing the use of higher order modulation to increase channel capacity. Basically, beamforming is most effective when the radio links operate in a *low SNR regime* and are power-limited [25].

Diversity

The main idea of diversity is to make available at the receiver more copies of either the transmitted or received signal, through *diversity gain* to increase the reliability of the channel. Diversity techniques are based on the observation that - at least in the case of flat fading - errors in reception occur at times when channel attenuation is high (i.e. when the channel is in a situation of deep fading), due to the consequent low SNR that it determines at the receiver input. Providing the receiver with multiple copies of the same transmitted signal, each affected by independent fading, the probability that all replicas of the signal fade simultaneously is considerably reduced. There are several ways in which diversity can be exploited, the main ones being:

- Frequency diversity: the same signal is transmitted by modulating L different carriers, where each pair of contiguous carriers must be separated in frequency by an amount greater than the coherence band Bc of the channel

- Time diversity: the same signal is replicated in L different time slots, temporally separated by a time greater than the channel coherence time Tc;

- Space diversity: the same signal is received by L different antennas which are spatially separated by a distance greater that the coherence distance Dc.

Spatial multiplexing

Spatial multiplexing provides *multiplexing gain* that increases communication system throughput by subdividing an outgoing signal streams into multiple sub-streams (also called spatial streams), where each of them is transmitted simultaneously and in parallel on the same channel, through different antennas. Spatial multiplexing allows the possibility to increase the data rate proportionally to the number of antennas and avoiding to spend extra radio resource as bandwidth or power. The key aspect is that radio channel multipath is not considered as an impairment but rather an advantage exploited to send and receive more samples at once, without time or frequency division multiple access techniques. Spatial multiplexing is most effective when the radio links operate in a *high SNR regime* and are bandwidth-limited. Moreover, it is only effective when the channel provides high rank (that is the number of streams that can be supported by the MIMO channel matrix) [25] meaning that the environment has a rich multipath. At low SNR operating points (that is power-limited channels with little interference), spatial multiplexing provides little benefits since the transmitter must split its power across the different spatial streams, thus weakening each stream and inducing bit errors that limit overall capacity gains.

Channel State Information

It is clear that, the key point in MIMO is the knowledge about the condition of the radio channel. Any combining scheme can take advantage from the information about the multipath that affects signals, named Channel State Information (CSI). CSI depends only on the capabilities of terminals to sound the channel and estimate its nature. This is not a trivial task, because CSI can change in time and space. The impact of the quality of CSI estimation may lead to sub-optimal results with respect to initial MIMO theoretical results. So, this represents one of the technical limitation of MIMO technology, demonstrated by the trade-off between speed and overhead introduced by sharing the CSI among transmitter and receiver. Using the observations from multiple antennas at an individual receiver (single-user MIMO, SU-MIMO) or when multiple end user receivers are simultaneously receiving signals from a MIMO transmitter (multi-user MIMO, MU-MIMO), the receiver can reconstruct the original transmitted sequence by using an estimate CSI. If the receiver's CSI is also available at the transmitter, precoding can be employed at the transmitter to send the data streams along the best dimensions of the channel, resulting in higher throughput with low-complexity receivers. Using channel knowledge at the transmitter is called *closed-loop* MIMO, where feedback is usually used to convey CSI from the receiver back to the transmitter [26]. In time-division duplex (TDD) single-frequency systems, the transmitter can directly measure the CSI when the receiver decides to transmit without the need for feedback, allowing *open-loop* MIMO.

1.4 Physical layer challenges

As mentioned in Section 1.2.1, 5G systems are expected to support diverse use cases and applications that will expand beyond the current systems. The wide range of capabilities will be tightly coupled with the different scenarios. The key challenge in the design and deployment of 5G systems is not only about the development of a new radio interface but also about the coordinated operation in a highly heterogeneous environment characterized by the existence of multi Radio Access Techniques (multi-RAT) systems, multi-layer networks, multi-mode devices, and diverse user interactions. Such scenarios create extreme - and sometimes conflicting - requirements on data rate, latencies, traffic handling capability, and availability of ubiquitous connectivity. Moreover, the flexible components can be properly optimized with an accurate understanding of radio channel propagation. This is a challenge, because these characteris-

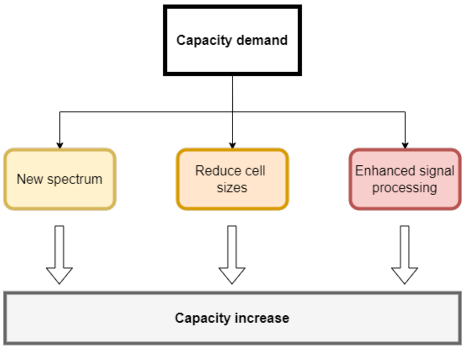

Figure 1.7: The three main techniques to boost system capacity

tics are less understood. As descripted in more detail in the next chapter, NR is the first ever mobile radio access technology going into millimeter-wave frequency range (with frequencies up to 100 GHz), targeting channel bandwidths in the GHz range and enabling massive multiantenna systems and largely benefing from all available spectrum options from 500 MHz to 100 GHz, including licensed, unlicensed and license-shared access to radio channel.

The 5G requirements can be met using techniques that are tried and tested in past generations of mobile networks, summarized in Fig. 1.7. These are to gain access to new spectrum, improve spectral efficiency, and densify the networks using small cells. Recent advances in air-interface design provide spectral efficiency performance very close to the Shannon limit. There is, however, room for increase in spectral efficiency through techniques such as coordinated multipoint, massive multiple-input multiple-output (mMIMO). In the case of 5G, these techniques are given new life using two means: the use of millimeter Wave (mmWave) spectrum for the availability of large blocks of contiguous spectrum, presented in the next chapter, and the subsequent adoption of beamforming as an enabler for high spectrum efficiency.

Chapter 2

Millimeter wave channel

In this chapter it is presented the mmWave spectrum, along with its characteristics and benefits. Since such characteristics differ a lot from those of the sub-6 GHz spectrum, it is important to develop new radio channel models which include the new challenges and requirements. For this reason it is also presented a brief insight on radio channels, their evolution across mobile generations and the current work in view of 5G systems with a focus on map-based models, particularly attractive for mmWave frequencies.

2.1 mmWave spectrum

Current 4G LTE systems are designed only for frequencies below 6 GHz. With the explosive growth of data rate demand, the sub-6 GHz spectrum shortage has led to consider the millimeter wave (mmWave) frequencies for future wireless systems. The mmWave frequencies strictly refers to the 30-300 GHz band (extending the spectrum also to the 10-30 GHz band, as industry generally considers a more relaxed definition), with a wavelength range of 1-10 mm [27]. In 5G framework, 3GPP has decided to support the range from below 1 GHz up to 52.6 GHz already from the first releases of NR (the FR-1 frequency range). In compliance with ITU World Radiocommunication Conference (WRC) in 2019, in order to satisfy the IMT-2020 specifications, new bands above 24 GHz are meant to be allocated to mobile communications, as shown in Fig. 2.1 The primary motivation for using mmWave spectrum is its ability to provide extremely high data rates due to the large bandwidth available [29] [30]. Recently, this attractive potential has led to considerable interest in mmWaves for mobile systems both in industry [31] [32] and academia [33][34][35], with a growing belief that mmWaves bands will play a significant role in beyond 4G and 5G cellular systems [36]. Actually, wireless communications in mmWaves bands are not new. Such bands are widely used for satellite communications [37] and cellular

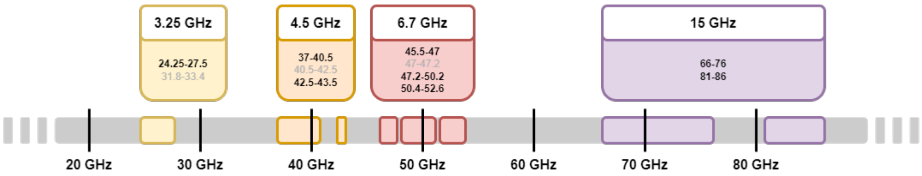

Figure 2.1: New IMT-2020 bands above 24 GHz [28]. Bands in gray are under investigation for IMT-2020.

backhaul [38][39]. More recently, mmWaves transmissions have been used for very high throughput wireless local area network and personal area network systems [40][41][42] in the newly unlicensed 60 GHz bands. While these systems offer rates in excess of 1 Gb/s, the links are typically for short-range or point-to-point LOS settings.

Despite these activities, this interest in mmWaves is still very recent and their application for longer range, NLOS cellular scenarios is a new, unexplored frontier, and the feasibility of such systems has been the subject of considerable debate.

2.1.1 mmWave propagation characteristics

While mmWave spectrum allocation carry lots of potential benefits for 5G mobile systems (as shown in the next section), it presents its own set of unique challenges that must be overcome in order for it to be used for mobile use cases. In particular, mmWaves propagation characteristics are inherently different from those of the sub-6 GHz spectrum where most of today's wireless systems operate.

One of the key aspects of mmWaves propagation is the higher isotropic path loss which sets more stringent limits on coverage. In fact, isotropic free-space attenuation is inversely proportional to the square of the wavelength [43], as shown in Eq. 2.1.

$$PL = 20\log_{10}\left(\frac{4\pi d}{\lambda}\right) \tag{2.1}$$

However, the smaller wavelength of mmWave signals also enables proportionally greater antenna gains for the same physical antenna size which may be used to compensate for path losses.

While signals at lower frequencies can penetrate more easily through buildings, a significant concern for mmWaves is the high exposure to shadowing and blockage. Due to lower diffraction and higher penetration loss [44] experienced through obstacles, such as buildings [45][46], vegetation [47] and human activity [48], mmWaves signals undergo strong attenuation and are particularly vulnerable to blockage. In outdoor cases, mmWaves transmissions can experience significant attenuations in the presence of heavy rain [47]. Moreover, in

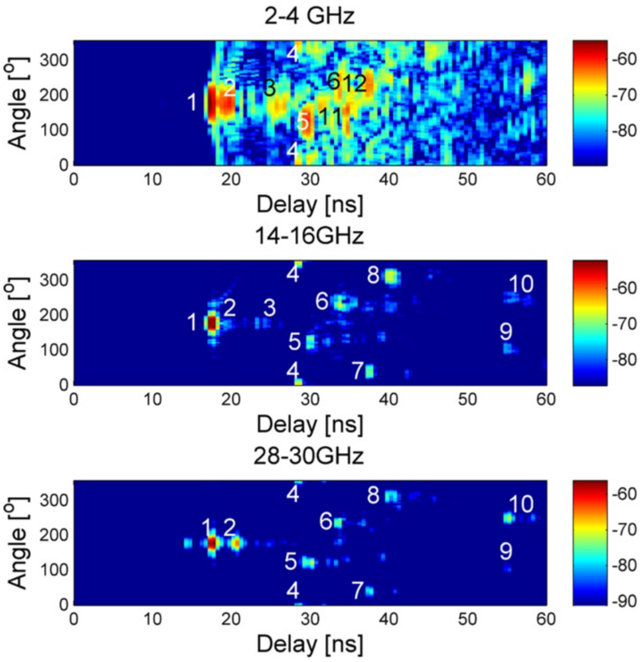

Figure 2.2: Power-angle-delay profile measured with directive antennas at different frequency bands [50].

the frequency range up to 100 GHz, two absorption peaks occur in standard atmosphere. The larger one is due to oxygen at 60 GHz and corresponds to 15 dB/km.

Moreover, at these frequencies the channel is highly time-variant due to the higher Doppler spread effect. Such frequency dispersion is caused by the mobility of the terminals and its extent is proportional to both the frequency and speed of mobility as shown in Eq. 2.2

$$f_D = \frac{v}{c} \cdot f_c \qquad (2.2)$$

The resulting higher Doppler spread leads to a channel coherence time which is particularly lower than that of sub-6 GHz frequencies [49] meaning that it changes much faster in time. This higher variability in the time domain, along with the higher exposure to shadowing and blockage leads to a channel which is often intermittent and discontinuous.

At mmWave frequencies the channel is often spatially sparser and more specular [50][51][52] with respect to lower frequencies. As shown in Fig. 2.2, richer multipath environments can be observed for sub-6 GHz frequencies, with many more paths present in both delay and angle domains, while only few specular paths are identified at higher frequencies, both in outdoor [53] and indoor [54]. This might be due to a stronger diffuse scattering from objects at low frequency bands, as the wavelength is more comparable to object dimensions. At the higher frequencies, the wavelength is much smaller, thus specular reflections are dominant. The diffuse component of the channel is typically rich and spread out in direction, whereas the specular component is composed of a few spikes in direction and delay, as shown in the bottom plot of Fig. 2.2. Moreover, due to the higher path loss, beamforming techniques (even at both ends) need to be considered, which further reduces the multipath richness, as only few propagation paths are selected. Whether diffuse scattering becomes stronger or weaker at mmWaves with respect to lower frequencies is still under debate, and even conflicting analyses can be found in literature. In particular, some authors hypothesized a stronger Dense Multipath Component (DMC) at mmWave frequencies compared to lower frequencies [55]. However, recent studies have shown that the actual ratio of the DMC to the Specular Multipath Component (SMC) is similar [56], or even lower [57]. Another outcome from [50], confirmed by our results in chapter 4, is that at mmWaves frequencies specular reflections are dominant and also higher-order reflection may be significant [58][59], while diffraction effect is weak.

At mmWave the polarimetric properties of propagation become important. Results indicate that most multipath contributions are polarization dependent, as they appear and disappear from channel's power profiles depending on the polarization of both the transmitter and the receiver [60].

2.1.2 mmWave benefits

The mmWaves frequency band is nowadays seen as the most suitable wireless frequency band for transmitting several gigabits via radio. These higher frequencies carry many potential benefits, gaining considerable attraction within the wireless industry [61].

First of all, in this part of the spectrum more bandwidth is available. This would allow service providers to significantly expand the channel bandwidths far beyond the current LTE 20 MHz channels. The availability of large contiguous spectrum blocks of 1 GHz or more, allows higher data rates and reduced latencies. Large blocks of spectrum also make it possible, in early deployments, to tradeoff spectral efficiency for bandwidth (i.e. high data rates can be achieved even with low-order modulation schemes, requiring lower power, complexity and costs).

Moreover, most of these bands appear to be unused and free, suggesting the absence of interference from other technologies.

As mentioned above, at these higher frequencies, transmission and penetration losses are much more critical than lower frequencies. The consequently higher attenuation allows to reuse the same frequency in a shorter distance, which increase the channel capacity directly. The possibility of dense frequency reuse over spatial domain due to the use of mmWaves, is another reason among the others of moving towards very smaller cells (cell densification), for efficient interference management, leading to an improved per-area efficiency.

A considerable attraction point is that at these higher frequencies, due to the very small wavelengths, large-scale antenna arrays can be deployed - especially at the base stations - leading to the design of massive MIMO (mMIMO) systems [62]. A mMIMO system can not only enjoy the benefits of conventional MIMO systems (see chapter 1), but also significantly enhance both spectral efficiency and energy efficiency [63]. In particular, analog beamforming can be implemented to compensate for the high propagation losses, to reduce interferences with other users by steering zeros toward interfering paths and to cope with time variations of the channel by steering the beam toward major paths to optimize signal strength. Pencil-beamforming (that is the use of very narrow beams) can help also to achieve dense spatial frequency reuse. Furthermore, because many antenna elements can be implemented on the small aperture, it is possible to increase the channel capacity significantly by spatial multiplexing if the receiver SNR is sufficiently high [64][65]. These main advantages enable mMIMO to be a promising candidate technology for the 5G wireless communication networks [66][67]. In both spatial multiplexing and beamforming, interaction between the antennas and the propagation conditions determines the attainable performance of a radio link. As mentioned in the previous chapter, whether to use spatial multiplexing or beamforming depends on the operating SNR and channel characteristics. In Section 2.1.1 it has been mentioned the debate between DMC and SMC. The DMC affects the Spatial-Degrees-of-Freedom (SDoF) of the propagation channel and determines the extent of the possible channel capacity improvement through spatial multiplexing. The SDoF is determined by inherent multipath richness of the propagation channel and the antenna aperture size [68]. The higher the SDoF the higher improvement through spatial multiplexing. On the other side, the higher SMC the lower multipath richness, meaning that there are only few dominant paths, which can be better exploited through analog beamforming.

2.2 Radio channel models

To meet the minimum requirements and to support the different use cases outlined in the previous chapter, mobile operators are forced to use mmWave spectrum. One of the basic highly important challenges in the development of mmWave technologies is the lack of appropriate radio channel models based on the peculiar characteristics of mmWave propagation, which are not fully addressed by the existing models developed for bands below 6 GHz.

Radio channel models are not only used in analysis and simulations when per-

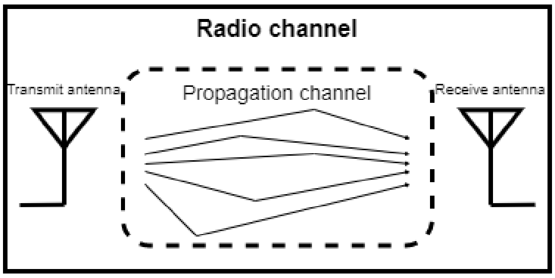

Figure 2.3: The radio channel consists of the transmit antenna, multipath propagation channel, and the receive antenna.

forming research, development and standardization of new telecommunication systems. Such models are of great importance in network deployment, optimization and conformance/performance testing. For example, once a certain system has been standardized and industry has developed devices to operate in the system there could be the need to evaluate the performance of any mobile terminal models by executing a comprehensive set of measurements. Such measurements are based on radio channel models and specific setups and procedures, in order to provide accurate, repeatable, and comparable results.

A typical communication system is sketched in Fig. 2.3, and consists of a transmitter, a receiver, and the channel. The channel plays a very important role in communication system design because the transmitter and receiver designs must be optimized with respect to the target channel. A *radio channel* is composed of a transmitting antenna, the (multipath) propagation channel and a receiving antenna. The *propagation channel* is the environment where the radio waves propagate from the transmitting antenna to the receiving antenna. Radio channel is determined once the transmitting and receiving antenna illuminate the propagation channel. In Line-Of-Sight (LOS) radio links it is possible only one electromagnetic direct path between transmitting and receiving antenna and this is not influenced by obstacles present in proximity of the radio link. The free space propagation is described by the Friis transmission law. All the other radio links are in a Non-LOS (NLOS) condition. In this case signals propagate from the transmitter to the receiver through different propagation mechanisms such as reflection, diffraction, trasmission and scattering. Due to these mechanisms, between the two antennas there are many possible electromagnetic paths (multipaths), so that the total electromagnetic field present on the receiving antenna is the superposition of those related to several waves. Consequently, on the receiving antenna it takes place an interference phenomenon between the various electromagnetic waves, whose effects are collectively indicated with the term *fading*. Fading is a characteristic of most practical radio channels and represents the fluctuation of the channel gain over time, frequency, and space.

To account for the multipath, the channel was traditionally modeled as a set of discrete plane waves which combine at the receive antenna. Each discrete wave is determined by its path defined by three factors: delay, attenuation and phase shift. In general, for the plane wave expansion, the channel between transmit antenna and the receive antenna is mathematically characterized by its discrete time-variant Channel Impulse Response (CIR), $h(\tau, t)$, that can be written has

$$h(\tau, t) = \sum_{n=1}^{N} a_n(t) e^{-j2\pi f_c \tau_n(t)} \delta[\tau - \tau_n] \tag{2.3}$$

where, $a_n(t)$ is the attenuation factor for the signal received on the n-th path at time instant t, τ_n is the propagation delay at the n-th path and time t, $e^{-j2\pi f_c \tau_n(t)}$, is the phase rotation of the signal component at delay t at carrier frequency f_c and $\delta[\cdot]$ is the Dirac Delta function. In typical mobile communications scenarios the number of paths needed to characterize the channel (N in Eq. 2.3) may be very large. In multiantenna systems (e.g. MIMO), the time-varying CIR is replaced by the $N_R \times N_T$ channel matrix $\mathbf{H}(\tau, t)$, given by:

$$\mathbf{H}(\tau, t) = \begin{bmatrix} h_{1,1} & h_{1,2} & \dots & h_{1,N_T} \\ h_{2,1} & h_{2,2} & \dots & h_{2,N_T} \\ \vdots & \vdots & \ddots & \vdots \\ h_{N_R,1} & h_{N_R,2} & \dots & h_{N_R,N_T} \end{bmatrix} \tag{2.4}$$

where $h(i, j)$ is the channel coefficient corresponding to the j-th transmit antenna and the i-th receive antenna.

Traditionally, the propagation channel was typically the only component of the system that could not be engineered and the other components had to be designed with the conditions and constraints set by it. However, recent trends on *meta-materials* and *meta-surfaces* [69] [70] (which are out of the scope of this work) have shown the possibility of planning the environment as well. Metamaterials are artificial engineered materials whose properties go beyond what nature offers; meta-surfaces are the 2D counterparts of metamaterials, that is thin engineered structured surfaces. Nevertheless, propagation and radio channel modelling are crucial in telecommunication research and system design.

2.2.1 Evolution of radio channel models

Channel models evolved across mobile generations. The evolution of channel modelling is illustrated in Fig. 2.4 along with the new emerged challenges. In the earliest systems (1G) the communication link was established between stationary and highly elevated radios. The key design aspect was the received power level obtained by specifying antenna gains and by determining the path loss, describing the overall attenuation of signals in the propagation channel. Hence,

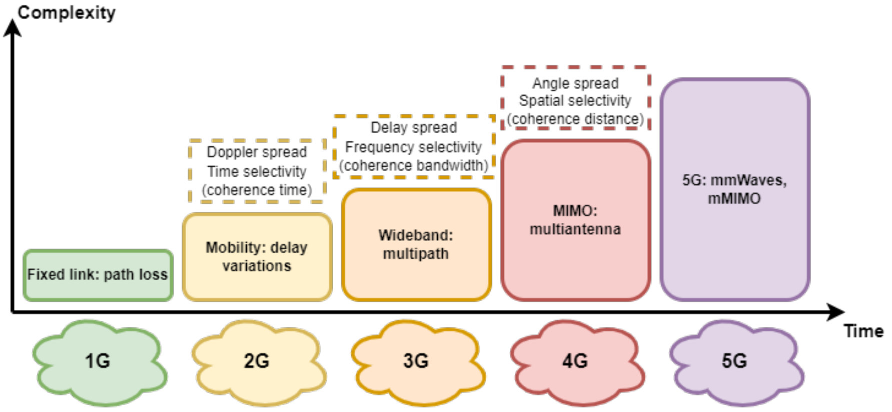

Figure 2.4: Evolution of mobile communication systems and channel model features

channel models were essentially path loss models, usually empirically determined (that is developed by finding a suitable function that fits to a large measurement data set) [71]. A random shadow fading term is commonly considered and modelled with a log-Normal distribution in order to represent additional fluctuation in the path loss.

In the next 2G systems, it was introduced the support for mobile users. Mobility created the need to model the time selectivity of the radio channel, caused by the motion of transmitter or the receiver (or both) and the scattering objects in the environment, which turns into a Doppler spread effect. Hence, 2G channel models had to take into account the *Doppler-time* domain. In the early models the probability distribution of channel amplitudes (gains) was modelled with Rayleigh in NLOS or Ricean distributions in LOS conditions [72]. In addition to the amplitude distribution, also the Doppler power spectrum (DPS) and the temporal auto-correlation function were modelled [73].

Studies on wideband communication systems (3G) led to channel modelling for both delay and frequency domain characteristics. In fact, wideband systems introduced the notion of frequency selectivity, which is caused by the superposition of many multipath components arriving with many different delays, generating a delay spread. Hence, new channel models needed to consider also *delay-frequency* domain. The resulting radio channel is a fading channel, both in time and frequency according to the specified statistics. A common approach was the so called *tapped delay line* (TDL) modelling. In this method a radio channel is specified by a number of delay taps, each with characteristics such as the average power, excess delay of the propagation path, amplitude distribution function, and DPS [74].

The introduction of antenna arrays and MIMO systems in 4G expanded the modelling complexity substantially, since the spatial and polarimetric structure of the radio channel had to be considered as well. In particular, the multipath components arriving from different directions in space create a spatial selectivity. Hence, next to the Doppler-time and delay-frequency domains, 4G channel models requires the description in the *space-direction* domain. There were different approaches for this. The so-called *correlation matrix based* method utilizes the Kronecker product of both link end antenna correlation matrices. The principle is to extend the TDL description by specifying transmitter and receiver correlation matrices, either for each tap, or jointly for all taps [75]. This approach gained high popularity, as it is simple to implement, and, maybe more importantly, because it provides analytical tractability. Another method for characterizing the wideband space-time MIMO channel is the *geometry-based stochastic channel model* (GSCM) [76][77]. In GSCM antenna radiation patterns and array geometries are specified independently as well as bi-directional propagation parameters. Then, a generic mathematical framework is used to compose time-variant MIMO channel transfer functions based on the previously computed parameters. The propagation channel is specified by a limited number of discrete propagation paths, commonly called sub-paths or rays, each having specific angular and gain parameters, without any particular definition of the environment. They are stochastic as they model spatial radio channel with randomly drawn directional and other propagation parameters. The method is flexible, versatile, but still with reasonable implementation complexity. It gained wide acceptance, now being the de-facto modelling approach for cellular communication system evaluations in numerous studies and standards such as [78][79][80]. Furthermore, the recent 3GPP channel model for 5G evaluations is a member of the same GSCM family.

2.2.2 Current work on 5G radio channel models

The main goal of channel modelling is to generate the radio propagation coefficients of Eq. 2.4 in time, space and frequency domains as accurately as possible under acceptable computational complexity for the purpose of link level or system level simulation. The model used should be consistent across wide range of environments, network topologies and frequencies. Moreover, channel models should be able to illustrate the key characteristics of the propagation under different circumstances and requirements. The last block of Fig. 2.4 refers to the upcoming 5G systems. The novel features of 5G systems, such as mmWave spectrum and mMIMO, set new channel modelling challenges and requirements that are not addressed by the models of previous generations. Due to frequency allocation for 4G and earlier cellular systems, the models were mainly targeted at sub-6 GHz frequencies. Thus, they are not directly applicable for 5G needs. 5G systems features are extensively investigated and the corresponding new requirements for the channel model are identified in [81][82][58][83][84] and should be taken into account during channel modelling for 5G use cases.

The primary requirement is the support for mmWave frequencies, motivated by the considered spectrum allocations for 5G systems. In particular, new channel models must accommodate a wide frequency range up to 100 GHz. The joint propagation characteristics over different frequency bands will need to be evaluated for multi-band operation. They also must support large channel bandwidths, up to 2 GHz, where the individual channel bandwidths may be in the range of 100 MHz to 2 GHz and may support carrier aggregation.

Moreover, the new channel models must support large antenna arrays, having very high directivity for compensating severe transmission losses and with a channel angular resolution down to around 1 degree. Current channel modelling needs corresponding improvement in angular resolution. Such antenna arrays could be of different types as linear, planar, cylindrical and spherical arrays, with arbitrary polarization. Overall, the antenna arrays will get larger, in the number of elements and either or both in their electrical and physical size. Both with electrically and physically large arrays, the far field distance increases and the suitability of planar wave modelling may become questionable [81]. Hence, these large arrays require spherical wave modelling replacing the commonly used plane wave approximation. Also, with large arrays it may be not appropriate to assume that all the antennas of a single radio link experience the same propagation paths [85].

The new channel models must ensure consistency, especially in the spatial domain, which may be characterized, for example, via spatial coherence, intersite correlation, and correlation among frequency bands. Taking into account mobility as well, all channel characteristics must vary reasonably and continuously because either or both ends of the radio link are moving. In particular, the commonly used channel models [82] are drop based, meaning that the scattering environment is randomly created for each link. The corresponding performance of spatial techniques is exaggerated, because even close-by mobiles see independent scatterers, which is not the case in reality. A spatially consistent model can also inherently support mobility of users.

Finally, the descriptive and computational complexity of the channel model must be resonable. The model must be described in such a compact and clear way that it can be implemented unambiguously and it must be implementable so that the required computing resources (processing units and memory) and computing time are feasible. Without a functional implementation, the model is not useful for any practical evaluations.

Conventional MIMO channel models such as the WINNER II [86] and COST 2100 [87] models fail to capture these features and therefore they cannot be directly used for 5G scenarios. There are many existing and ongoing campaign efforts worldwide targeting 5G channel measurements and modeling. Recent activities and results towards 5G channel models include: 3GPP [88], METIS-2020 [82], COST IC1004 [89], 5G mmWave Channel Model Alliance [90], MiWEBA [91], mmMagic [92], ITU-R [8]. In these projects, many scenarios are considered using mmWave frequencies, such as street-canyon and open square in urban outdoor cellular environments and shopping malls, open/closed indoor office environments, and stadium scenario. A compact overview of channel models from early geometric MIMO models up to the most recent mm-wave models is given in [93] and in [94].

3GPP channel model

Standardization and regulation activities have been carried out mainly by 3GPP and the ITU-R. In 3GPP a study item targeted for specifying a channel model for above 6 GHz frequencies, was initiated early 2016. The purpose was mainly to cover the new frequency area, but also to consider requirements from the coming 5G NR technology. Later, with the final model specification [88], the applicable frequency range was broadened to also include sub-6 GHz. This model is currently the de-facto channel model in the industry for 5G evaluations. It is an extension of the GSCM [80] for higher frequencies with revised parameters. It contains optional features for oxygen absorption, large bandwidth and large antenna arrays, ground reflection, blockage and spatial consistency. The latter in particular, is based on a new procedure, described in [88], given the user locations based on the parameter-specific *correlation distance* values. The modelled scenarios include urban micro street canyon and open area (UMi), urban macro (UMa), rural macro (RMa), and indoor office (InH).

Fig. 2.5 shows the main steps of the 3GPP channel modelling. First, the large scale parameters are generated. After having determined the scenario, the network deployment and the antenna parameters, it is evaluated the LOS probability and the consequent path loss evaluation. Then, the fast fading is calculated, modelling the time-varying fluctuations of wireless channels that are caused by the combination of multipath and user mobility. Finally, channel coefficients of a link between a transmitter and a receiver are determined by the composite channel impulse responses of the multiple path components, characterized by a path delay, a path power and random phases introduced during the propagation as well as the incident path angles.

2.2.3 Ray-based models

The main stream in spatial channel modelling has been on GSCMs. As describes above, they model spatial radio channel with randomly drawn di-

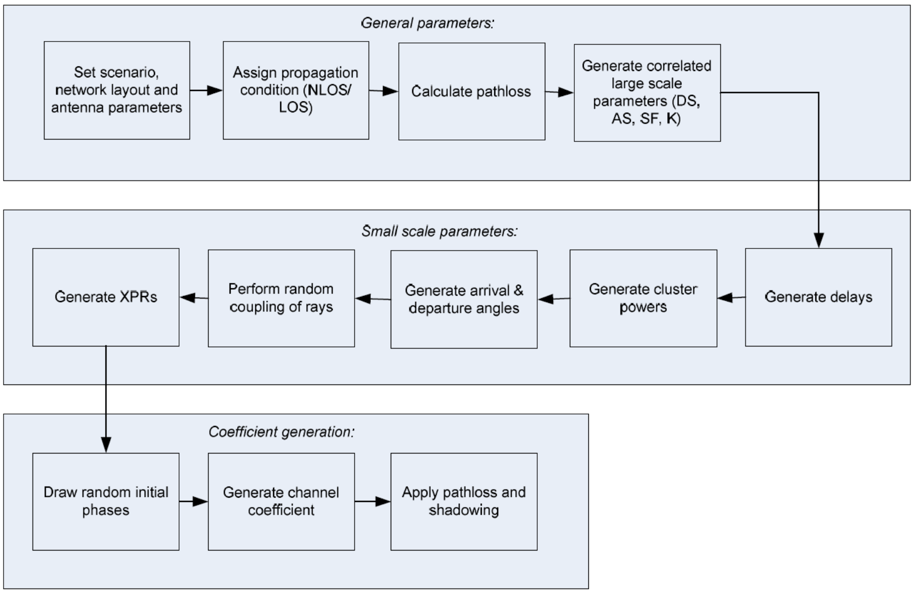

Figure 2.5: Channel generation steps in the 3GPP 3D channel model. Picture taken from [88]

rectional and propagation parameters, without any particular definition of the environment. Besides GSCM, the METIS group proposed a map-based channel model supporting various modeling requirements of 5G. Such model was established based on Ray-Tracing techniques. It aimed at tracking each ray from the transmitter to the receiver, considering interactions between rays and shadowing or scattering objects such as diffraction, specular reflection, diffuse scattering, and blocking are considered. In addition, 3GPP model adopted a hybrid of a GSCM and a map-based model, which was accepted and presented in the ITU-R M.2412-0 report [8]. Propagation prediction through ray-tracing simulations is getting more and more attention because of its ability to investigate most of the propagation mechanisms, such as reflection, scattering and diffraction, and inherently provides directionally resolved spatial characteristics. Although ray-tracing simulations often suffer some geometry data base errors and do not always include all of the relevant propagation mechanisms, such as non-specular scattering effects, ray-tracing results have been successfully used to model wireless radio propagation [95][96][97], and will become more important at mmWave frequencies.

Ray-based methods rely on ray approximation and on the Geometrical Theory of Propagation (GTP) to represent the propagating field as a set of rays, implementing all the propagation mechanisms mentioned before in order to model the radio channel in a digitized scenario. There are several reasons why a deterministic model is considered to be more suitable for 5G wireless communications.

RT, through GTP and the Uniform Theory of Diffraction (UTD), along with the addition of non-specular scattering effects, can provide an accurate correspondence of real world propagation, with an acceptable computation complexity [98]. Such models, being map-based, inherently guarantee site-specific simulations as the properties of each ray (path loss, propagation delay, angle of arrival and angle of departure) are directly calculated by applying RT to a well-defined environment layout map. This also means that spatial and temporal consistency can be achieved naturally. Similar with the ability to fulfill spatial consistency, map–based model can simulate the correlation between any two communication links whose transmitters or receivers are either the same or nearby, where the correlation exists in both large scale fading and small scale fading. In view of mmWave frequency, another important feature is that there is no need to have additional bandwidth handling in RT tool as long as the bandwidth is up to 10% of carrier frequency. The calculation based on centre frequency can be representative for the whole bandwidth. If extremely large channel bandwidth ($>$ 10%) is needed, the bandwidth can be partitioned into several bins and ray–tracing is applied separately to each bandwidth bin. Finally, for the large antenna arrays beyond consistency interval, spherical wave calculation should be taken into consideration, where the ray–tracing can support it by calculating the propagation parameters.

Chapter 3

Fabry-Pérot material characterization

Several frequency bands above 6 GHz are being proposed for next generation wireless systems, and the electromagnetic characteristics of many common construction materials at these frequencies still need to be determined. The knowledge of the electromagnetic properties of construction materials is crucial for the design of future wireless systems, especially in relation to the increasing use of deterministic, ray-based, propagation models and tools for radio channel characterization in 5G and beyond systems. In this chapter, the new recently developed method for electromagnetic material characterization based on Fabry-Pérot procedure is presented and extensively discussed in the original pubblications [99][100] and [101].

3.1 Materials e.m. characterization

The next generation of wireless communication systems is envisioned to satisfy the current demand for higher data rates, lower network latencies and more reliable and ubiquitous connectivity [102][103]. As explained in the previous chapter, the congestion of the sub-6 GHz spectrum led to consider the use of several new frequency bands in the millimeter wave (mmWave) and sub-THz (100-300 GHz) ranges, where larger and unused bandwidths are available and advanced multiantenna techniques, such as massive MIMO (mMIMO) can be implemented with relatively compact antenna arrays to further enhance channel capacity and reliability. With respect to sub-6 GHz bands, such frequencies generally show peculiar propagation characteristics and in particular higher diffraction and penetration losses from walls and objects that strongly depend on the different material parameters [104][105]. Moreover, the effectiveness of multiantenna techniques depends on the wideband spatial and temporal properties of the channel. Therefore, there is the need of a deep and detailed radio channel characterization at these frequencies, for example using measurements and deterministic simulation tools. In the context of map-based tools, it is required the knowledge of the environment geometry and electromagnetic characteristics of all materials, (namely the relative permittivity and conductivity). Consequently, simple and fast electromagnetic characterization of construction and furniture materials at multiple frequency bands will soon become an urgent need for the design of future wireless networks and of smart buildings where such networks will have to operate [105]. Material characterization is also necessary to properly use the increasingly popular deterministic simulation tools such as Ray-Tracing.

Several methods for measuring the complex permittivity of materials have been developed over the years, each suitable for specific frequency range and material type. Well known methods include *transmission line methods* [106], *coaxial probe methods* [107], *resonant methods* [108][109], *impedance analyzer methods* and *free space methods* [110]. Each method has its own advantages and drawbacks and which technique should be used depends strickly on the boundary conditions: the required measurement accuracy and precision, band of interest, material properties, form of materials, destructive or non destructive, contact or contact-less and so on.

A measurement using the transmission line method involves placing a sample in a section of waveguide or coaxial line (called sample holder) and measuring the two ports complex scattering parameters with a vector network analyzer. The method involves the measurement of the reflected (S11) and transmitted signal (S21). The relevant scattering parameters relate closely to the complex permittivity and permeability of the material by equations. The conversion of S21 and S11 to complex dielectric parameter is computed by solving the equations using a conversion techniques such as Nicholson-Ross-Weir (NRW) method, NIST Iterative method or Short circuit line (SCL) method among the others. In many cases, the method requires sample preparation such as machining so that the sample fit tightly into the waveguide or coaxial line. Calibration must be carried out before making the measurement, usually involving the de-embedding function of the VNA. The measurement method allows the estimation of permittivity and permeability of the dielectric material. Such approach is commonly used to measure samples with medium to high loss and it allows to determine both the permittivity and permeability of the material under test.

In coaxial probe method the probe is pressed against a sample of material or immersed into the liquids and the reflection coefficient is measured and used to determine the permittivity. This method is a non-destructive testing method as the sample can be place in close contact with the probe without causing any changes in the material characteristics. The reflection coefficient is measured using a vector network analyzer. The VNA with a probe system is first calibrated so that the reflection coefficient measurements are referenced to the probe aperture plane. This method requires no machining of the sample and has an simple preparation.

Resonant measurements are the most accurate methods of obtaining permittivity and permeability. However, there are limitations on the frequencies and loss characteristics of the materials that can be measured with the method. There are many types of resonant methods available such as reentrant cavities, split cylinder resonators, cavity resonators etc. With resonance characteristics depending on the MUT in a cavity its quality factor and resonance frequency can be monitored to determine the dielectric parameters. The dielectric properties can be determined by first measuring the resonant frequency and quality factor of an empty cavity. The second step is to repeat the measurement after filling the cavity with the MUT. The permittivity or permeability of the material can then be computed using the frequency, volume and q-factor. There is no need to calibrate the network analyzer for this type of measurement.

Free space methods are the most commonly used for measuring the characteristics of construction materials at radio frequencies as they do not require to cut or machine the sample in order to measure it and therefore are suitable for non-destructive, contact-less tests on large construction and furnishing material samples. However, conventional free-space methods usually need multiple, accurate reflection or transmission measurements for different incidence/reception angles that require rotating positioners, anechoic environments and complex maximum-likelihood parameter determination methods or the numerical solution of scattering equations [111][112]. They could be affected by the presence of unwanted multipath propagation requiring for complex calibration procedures as the measurement of the absolute value of the reflection and transmission complex coefficients is usually required.

3.2 Fabry-Pérot approach

With respect to free space methods, the Fabry-Pérot approach is a simple and fast technique for the characterization of low-loss materials based on the Fabry-Pérot resonance (depicted in Fig. 3.2) that takes place inside a material slab [113]. Instead of performing multiple measurements, a wide measurement bandwidth is used to extract the same information from the difference between adjacent resonance frequencies using a simple setup (portable spectrum analyzer or a Vector Network Analyzer (VNA) as for instance). Because of the simplicity of the setup, measurements can even be executed on site, without the need of carrying around heavy or large material samples such as a marble slab or a door leaf. However, the method has its limitations: it can only be applied to thick enough slabs and/or over a wide enough bandwidth in order to show up at least two or three successive resonance dips on the frequency span. At mmWave frequencies, a thickness of 1 cm and a bandwidth of 1-2 GHz is usually enough to successfully apply the method: over such a bandwidth the complex permittivity of most materials at frequencies above 6 GHz is generally constant. Moreover, it can only be applied to materials that can be considered relatively homogeneous: this means that for grainy materials such as sandstone or chipboard, grains must be significantly smaller than the wavelength in order to prevent severe diffuse scattering from hampering Fabry-Pérot resonance.

3.2.1 Description of the method

Electromagnetic characterization of materials consists in the determination of their complex relative permittivity given by Eq. 3.1

$$.\epsilon_r = \epsilon' - j\epsilon'' \tag{3.1}$$

We assume here that the imaginary part of ϵ_r is due to equivalent ohmic conduction, and therefore:

$$\epsilon'' = \frac{\sigma}{2\pi f \epsilon_0}, \tag{3.2}$$

where σ [S/m] is the conductivity of the material, and ϵ_0 is the vacuum's permittivity. Applying the proposed method to low-loss materials, i.e. with $\epsilon'' << \epsilon'$, real and imaginary parts can be determined separately, and therefore the measurement procedure is simpler and less critical compared to traditional methods [113][99].

Fig. 3.1 shows a diagram with the main steps of the Fabry-Pérot parameter estimation procedure, including the determination of both ϵ' through the reflection measurement (branch on the left) and ϵ'' through the transmission measurement (branch on the right).

First step

The first step in the measurement procedure is to determine the real part ϵ' of Eq. 3.1 through the Fabry-Pérot method itself. When a plane wave impinges on an infinite low-loss dielectric slab it takes place a resonant phenomenon due to a series of multiple reflections - and transmissions - within the slab. This phenomenon results in a frequency response pattern with a number of deep notches - the Fabry-Pérot resonances shown in Fig. 3.2. By measuring the reflectivity of the slab for a given incidence angle over a wide-enough bandwidth B, in order to highlight at least two or three resonance notches and estimating the frequency distance Δf between two adjacent notches, it is possible to compute

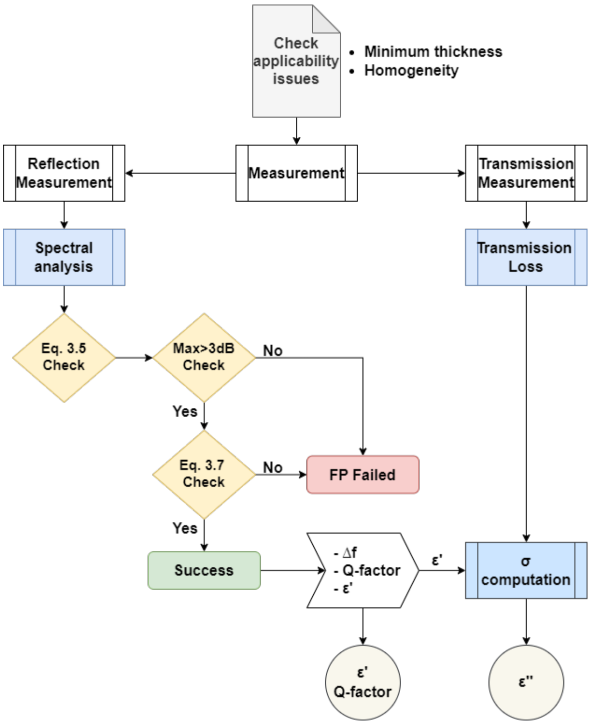

Figure 3.1: Fabry-Pérot procedure

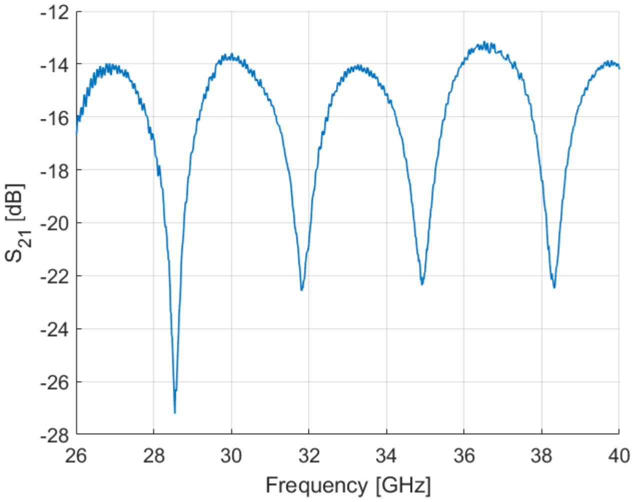

Figure 3.2: Periodic pattern of a measured frequency response for a sample of Paraffin in [26-40] GHz band

ϵ', according to the following equation [113]:

$$\epsilon' = \left(\frac{c}{\Delta f \cdot 2w}\right)^2 + (\sin\theta_i)^2 , \tag{3.3}$$

where w [m] is slab thickness, θ_i [rad] is the incidence angle with respect to the surface normal and c [m/s] is the speed of light. As the other quantities in Eq. 3.3 are given from the setup, once Δf is known, it is possible to estimate the value of ϵ', in the chosen bandwidth. It is worth noting that, the higher the number of notches, the better the Δf estimation. If material characteristics – and therefore Δf – change over B, the estimated ϵ' it is to be understood as a mean value over B. In a very first version of the approach [113] such Δf was estimated by eye. However such a procedure is subjective, and not very precise: in this new, improved version of the method [101] Δf estimation is performed through a spectral analysis.

Second step

The second step is the evaluation of the imaginary part (ϵ'') of Eq. 3.1 separately, through a transmission method by matching the measured transmission coefficient with a reference model [100].

Although building materials are low-loss at most frequencies, ϵ'' is very important to determine the overall penetration loss, a critical parameter for the design and deployment of mmWave systems. A procedure has been developed to fit the theoretical model to a least squares approximation of the measured curve. The procedure leads to an estimate of the transmission loss of the slab over the considered bandwidth, using the ϵ' value previously estimated through Eq. 3.3. Again, as the procedure provides only one value of σ, it has to be considered as a mean value over B. Time-gate filtering techniques (see Section 3.2.5) can be applied before the estimation of both ϵ' and ϵ'' in order to filter out environment multipath and noise. In ϵ' estimation however, time gating must be limited in order to allow the Fabry-Pérot resonance interference pattern to show up.

3.2.2 Description of the setup

For both reflection and transmission measurements (namely the first and second steps respectively) the setup is exemplified in Fig. 3.3: for reflection measurements (Fig. 3.3a), antennas are set symmetrically at a fixed incident angle with respect to the normal of the material under test surface. An absorber can be used to block the direct path between the antennas, though the procedure is resilient to crosstalk issues. For transmission measurements (Fig. 3.3b), antennas are set to be in front of each other. The transmission coefficient is computed by de-embedding antenna gains and free space loss: to this aim, it is required

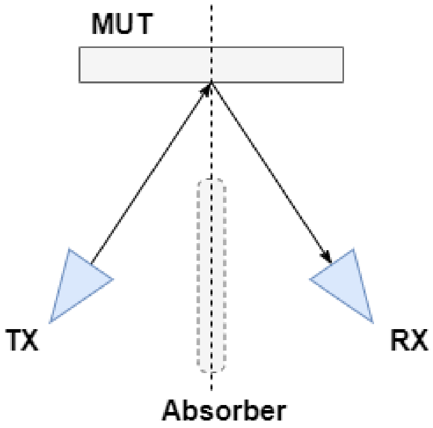

(a) Reflection setup

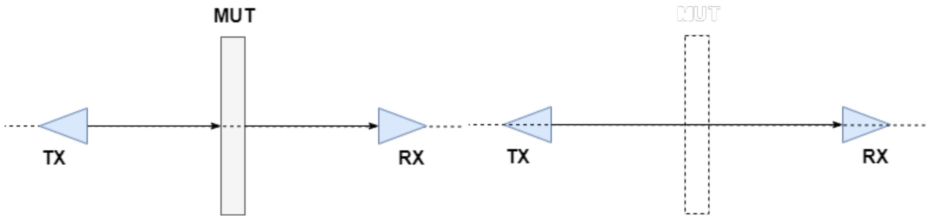

(b) Transmission setup (c) Transmission ref. setup

Figure 3.3: Reflection measurement setup (3.3a) and transmission measurement setup (3.3b, 3.3c)

to normalize the measurement with a reference measurement, which is recorded by keeping the two antennas in line-of-sight without the material under test in between (Fig. 3.3c). It is worth noting that this normalization is not needed for reflection measurements.

In order to properly apply the Fabry-Pérot method, some precautions must be taken during the setup. First of all, the slab's size should be large enough to ensure that the antenna's -3dB lobe footprint is concentrated around the slab center to reduce edge diffraction effect, which might generate similar frequency oscillations as the Fabry-Pérot resonance. Secondly, the distance between the slab and the aperture of the antennas should be at least 10-15 wavelengths to ensure far field conditions. Moreover, the slab should be uniform and flat with constant thickness in order to avoid lens effects. Finally, the frequency resolution should be high enough to identify unambiguously the position of the notches.

3.2.3 Estimation of ϵ'

As mentioned above, the value of Δf to be used in Eq. 3.3 might be estimated by eye from the frequency response graph as that shown in Fig. 3.2, but such a procedure is subjective, not very precise and problematic when noise and scattering blur the pattern and Fabry-Pérot notches are not univocally identifiable (e.g. Fig. 3.4b). Therefore, an automated procedure based on a spectral analysis is defined in the following to solve the mentioned problems. The procedure is based on the frequency response, i.e. the module of the measured $S_{21}(f)$ ($|S_{21}(f)|$ [dB]). The FFT of $|S_{21}(f)|$ is performed to find the first harmonic in the FFT-transformed domain which corresponds to the inverse of the resonance period, that is, $1/\Delta f$. However, if the frequency response still embeds a Fabry-Pérot resonance periodicity but noise and/or scattering and multipath make its pattern irregular, the evaluation of Δf can be challenging, or in extreme cases not possible. Note that such impairments are usually due to material's irregularities: in this case most characterization methods fail. The Fabry-Pérot method, however, can still give an estimate of effective material parameters thanks to the procedure described below. In Fig. 3.4 for example, paraffin (Fig. 3.4a) shows a very clear periodic pattern, which translates into a prominent harmonic in the relative FFT transform, while chipboard (Fig. 3.4b) does not show a well-defined periodicity and the FFT transform presents two main harmonics (red and blue lines). The black line in Fig. 3.4 sets the lower bound for the acceptable Fabry-Pérot harmonics as defined by Eq. 3.5 (so, the first harmonic identified by the red line in Fig. 3.4b must be discarded). Hence, the main purposes of the FFT-based procedure are: i) understand if the Fabry-Pérot resonance is established; ii) if so, estimate the correct resonance harmonic; iii) estimate the quality of such a resonance. The procedure must be automatic,

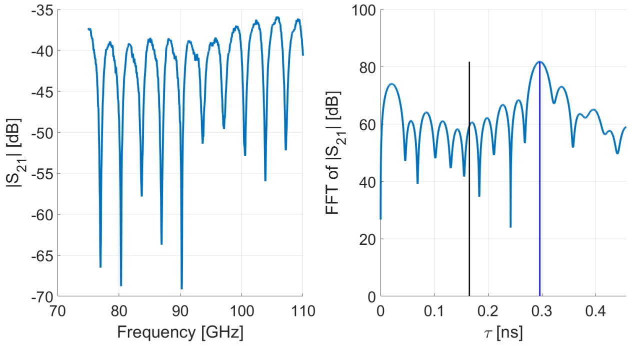

(a) Paraffin

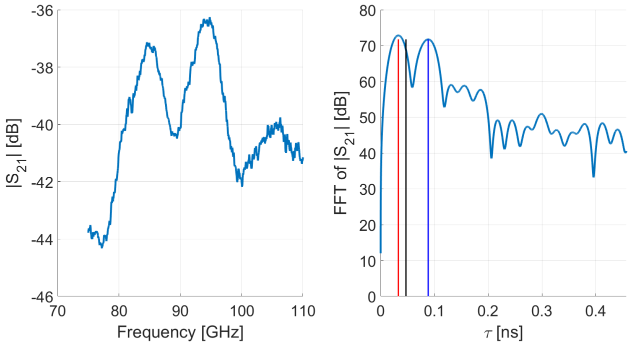

(b) Chipboard

Figure 3.4: Frequency response patterns and their relative FFT in two different cases: a clear case of resonance for Paraffin (Fig. 3.4a) and an ambiguous one for Chipboard (Fig. 3.4b).

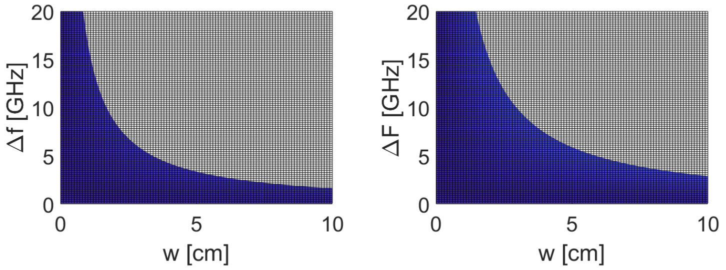

(a) $\theta_i = 40°$ (b) $\theta_i = 60°$

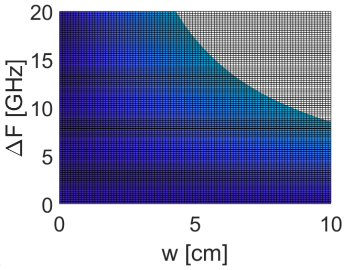

(c) $\theta_i = 80°$

Figure 3.5: Regions for allowed $\Delta f, w$ pair as a function of a

.

reliable, and fast. In order to identify the correct spectral component, it is worthwhile to find an approximate range for acceptable Δf values. Considering Eq. 3.3, the value of ϵ', cannot be smaller than the value of the vacuum $\epsilon' = 1$ leading to $\epsilon' \geq 1$. Calling $(\sin\theta_i)^2 = a$ with $\theta_i \in (0° - 90°)$, we have:

$$\left(\frac{c}{\Delta f \cdot 2w}\right)^2 \geq 1 - a. \tag{3.4}$$

Hence:

$$\Delta f \cdot w \leq \frac{c}{2\sqrt{1-a}}. \tag{3.5}$$

In Fig. 3.5 the allowed range for $(\Delta f, w)$ pair is shown, for increasing value of a. Given w, it is possible to check if the computed Δf value is meaningful. In addition, if a range of reasonable "initial guess" values can be assumed for ϵ' (for example from literature, manufacturers, etc.), it is possible to define the corresponding Δf range. If $\epsilon'_{min} < \epsilon' < \epsilon'_{max}$, it must be that:

$$\frac{c}{2\sqrt{\epsilon'_{max} - a}} \leq \Delta f \cdot w \leq \frac{c}{2\sqrt{\epsilon'_{min} - a}}. \tag{3.6}$$

In order to assess if the Fabry-Pérot resonance takes place, a comparison of the amplitudes of the frequency response's harmonics in the valid Δf range is performed: if the strongest harmonic is at least 3 dB above the second strongest

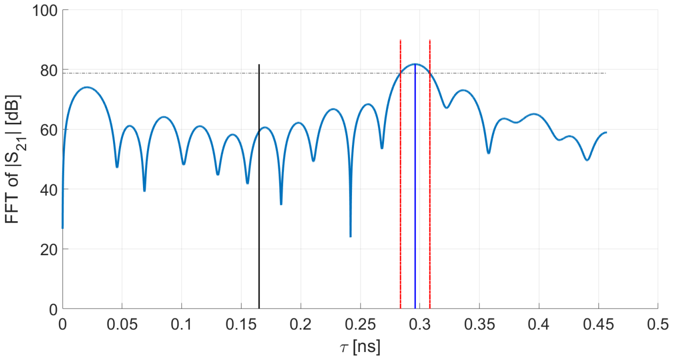

Figure 3.6: Paraffin resonance width $\Delta\tau$. The dashed black line is the -3dB level under the maximum (blu line). The interval between these two points (red lines) is $\Delta\tau$.

harmonic the resonance is confirmed; otherwise, if there are two (or more) harmonics with comparable amplitudes (that is, within 3 dB), we are not able to solve the ambiguity and to determine which is the true resonance's harmonic. Moreover, it is clear that a minimum of two notches within the considered measurement bandwidth B is required in order to identify at least one Δf. Hence, it must be true that $\Delta f \leq B$. However, a stricter condition is necessary in order to ensure that Fabry-Pérot resonance is good enough to yield reliable results. A number N of notches of the frequency response (see Fig. 3.2) is required. Therefore, if a valid harmonic is found, as a final validity check, it must be that:

$$\Delta f \leq \frac{B}{N-1}. \tag{3.7}$$

A reasonable value for N is 4. Finally, to estimate the quality of the occurred resonance (if any) we consider the quality factor Q, defined as the ratio between the resonance peak τ_0 and the resonance width $\Delta\tau$:

$$Q = \frac{\tau_0}{\Delta\tau}. \tag{3.8}$$

As shown in Fig. 3.6, τ_0 is the blue line x-axis position and $\Delta\tau$ is defined as the span between the half-power (black, dashed line) points of the resonance peak (red solid lines). The smaller the $\Delta\tau$ (hence, the higher Q) the better the resonance, as the harmonic is clearer. As an example, $\Delta\tau$ for the two cases of Fig. 3.4 are 0.0247 ns for the Paraffin ($\tau_0 = 0.2960$ ns) and 0.0288 for the Chipboard ($\tau_0 = 0.0885$ ns), leading to $Q = 12.00$ and $Q = 3.07$, respectively.

3.2.4 Estimation of ϵ''

Once ϵ' has been determined, ϵ'' must be estimated from the measurement of the transmission coefficient $T_{meas}(f)$ over the considered bandwidth. A proper procedure is applied to determine the σ value, and therefore the ϵ''. If hard time-gating is applied, i.e. Fabry-Pérot resonance is cut off, leading to transmission coefficients constant in frequency (see Section 3.2.5), or if the noise level is high, $T_{sim}(\sigma)$ should be computed using the single-path transmission formula in the appendix of [101] as stated in Section 3.2.5. Otherwise, the coefficients must be considered frequency-dependent, yielding $T_{sim}(\sigma, f)$. In this case, to compute the transmission losses, that heavily depend on the conductivity σ, we refer to the model described in [114] which has been modified to consider losses in the material under test and non-orthogonal incidence. The procedure is based on a least-square optimization method to determine the best-fit σ that minimizes the Root Mean Square Error (RMSE) between the simulated transmission coefficient $T_{sim}(\sigma, f)$ and the measured transmission coefficient $T_{meas}(f)$. The problem can be stated as follows: find σ^{opt} such that

$$\sigma^{opt} = \arg\min_{\sigma} \left(RMSE(\sigma) \right), \tag{3.9}$$

with

$$RMSE(\sigma) = \sqrt{\underset{f}{mean}\left(e^2(\sigma, f)\right)} \tag{3.10}$$

$$e(\sigma, f) = abs\left(|T_{meas}(f)| - |T_{sim}(\sigma, f)|\right) \tag{3.11}$$

where, $e(\sigma, f)$ is the error between the simulated and measured transmission coefficients. Error minimization is carried out using a standard iterative procedure until the desired precision is achieved. Fig. 3.7 shows the fitting of a measured paraffin transmission coefficient, $|T_{meas}(f)|$ (black line), in the considered [8-14] GHz band with the reference model, $|T_{sim}(\sigma, f)|$, computed for five values of σ (colored lines) in a range of $[0 - 4 \cdot 10^{-3}]$ S/m, at the third iteration of the procedure. The optimum value (in a minimum RMSE sense) is within such range. The measured transmission coefficient has been previously filtered through a time gating technique in order to remove multipath components' noise, as shown in Fig. 3.8.

3.2.5 Time-gating

Time-gating techniques can be applied to reflection and transmission measurements in order to select and keep only contributions arriving within a given maximum delay after the first one and filter out later arrivals, including the environment multipath [100]. However, internal reflections must not be filtered out as long as we want to carry out ϵ' measurements using the Fabry-Pérot interference pattern. In [99] it has been described the time-gating procedure applied in some works as [100][101].

It is worth mentioning that there is no relation between the number of internal reflections and the frequency-distance between two adjacent Fabry-Pérot

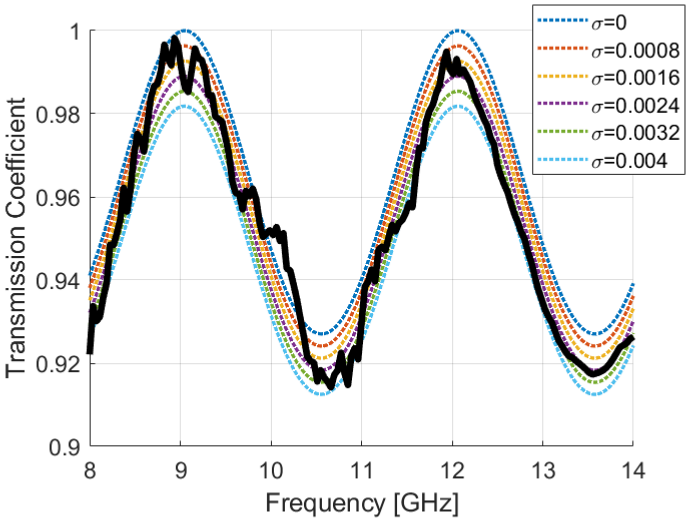

Figure 3.7: Measured (black) and simulated (coloured) transmission coefficient for $\sigma \in [0 - 4 \cdot 10^{-3}]$ S/m

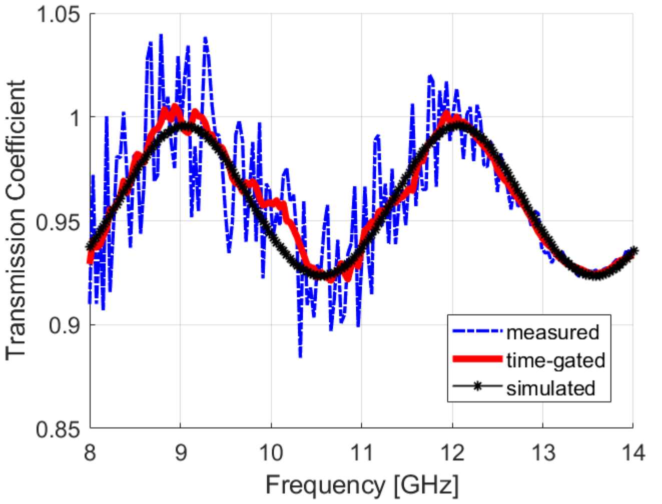

Figure 3.8: Measured (blue) and filtered (red) transmission coefficient for the Paraffin slab as a function of frequency. Simulated transmission coefficient (black) computed with the best value of sigma

notches (Δf). As a matter of fact, to satisfy Eq. 3.3, the following equation should hold [113]:

$$\delta = \left(\frac{2\pi}{\lambda_0}\right) \cdot 2\sqrt{\epsilon'} \cdot 2 \cdot \cos\theta_T = 2k\pi \tag{3.12}$$

where, δ is the phase rotation of the i-th reflected component with respect to the $(i-1)$-th one. As shown in Eq. 3.12, δ does not depend on i, hence the notches' position does not depend on the number of reflections retained within the time-gate window. Thus, it is enough to consider just two components (the direct path and the first double reflected path) in order for the interference pattern to show notches in the correct positions, thus allowing correct ϵ' measurements. Based on these evaluations, an aggressive time gating (*hard time-gating*) can be applied to single-out only the direct path in transmission measurements where - unlike reflection measurements - the Fabry-Pérot resonance is not functional to the estimation procedure. By doing so, all the multipath interference, and even the Fabry-Pérot resonance ripple, can be eliminated, the transmission coefficient becomes constant in frequency and its average value over the considered bandwidth can be considered, thus averaging out noise and using the resulting equation in the appendix of [101] to evaluate σ. However, if c is vacuum light speed and n is the refraction index, the delay of the first internal double-reflection with respect to the direct path in case of normal incidence is:

$$\Delta t = \frac{2w \cdot n}{c} \tag{3.13}$$

Using the typical values $w = 4$ cm, and $n = 3$, we get $\Delta t = 0.8$ ns, which is below the time resolution of most setups.

3.2.6 Advantages and limits of Fabry-Pérot method

As common materials are often heterogeneous compounds, they exhibit large variability between different samples and an accurate characterization is hardly possible. Rather than accuracy, simplicity, speed of execution and the possibility of performing contact-less and non-destructive measurement of large material samples are important features here. Under this perspective, an advantage of the Fabry-Pérot method is that all measurements can be easily performed in one single shot without the need of multiple measurements for different incidence angles, that would require rotating positioners and anechoic or quasi-anechoic conditions. The method only requires a simple measurement setup and the use of a general-purpose VNA or portable spectrum analyzers (as that used in this work, see Section 3.3.1) without the need of extensive calibration. Moreover, as stated in Section 3.2.2, references are not required for reflection measurements as the relative distance between frequency-domain notches, rather than absolute values of the reflection coefficient, is used for the estimate. The main limit of

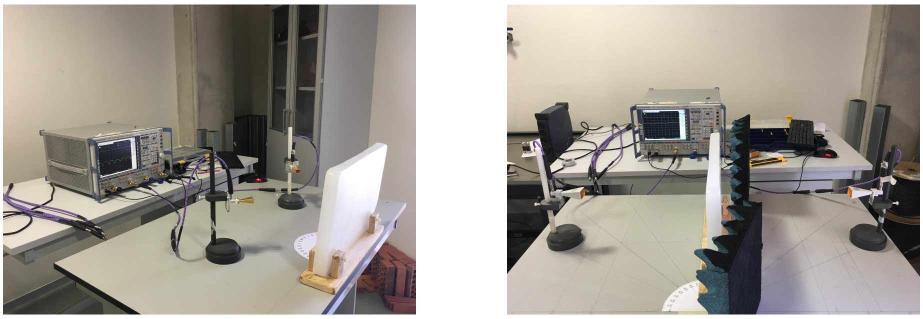

(a) Paraffin reflection measurement (b) Paraffin transmission measurement

Figure 3.9: Reflection measurement setup (3.9a) and transmission measurement setup (3.9b) for a paraffin slab

the Fabry-Pérot method resides in its applicability, which is limited to low-loss and flat materials. However, this requirement is common to several other characterization methods. In 3.3 it is given an estimation of the impact of the non-perfect flatness of the slab in terms of relative error.

3.3 Fabry-Pérot results

Different measurement campaigns have been performed in order to assess the reliability and accuracy of the method in practical cases and to show its usability and flexibility.

3.3.1 Measurement campaigns

An extensive measurement campaign has been conducted at the Universidad Politécnica de Cartagena (Spain), where many samples of different materials have been taken into account in diverse frequency bands. As shown in Fig. 3.9, the measurements have been performed with a Rodhe& Schwarz VNA, working in the frequency range from 10 MHz to 75 GHz, extended up to 300 GHz through an upconverter. The considered bands are: 26-40 GHz, 50-70 GHz, 75-110 GHz and 220-330 GHz. During this campaign many different samples of materials have been tested such as brick, granite, plywood, various types of chipboard, paraffin, teflon, nylon and tile. Some of these are shown in Fig. 3.10

Other campaigns have been carried out at the University of Bologna. Here, two setups have been used for measurements: a traditional VNA and a portable spectrum compact analyzer (SCA) [115] for on-site measurements. Each equipment shows advantages and disadvantages with respect to the performed measurement. Desktop VNA provides greater measurement capabilities and accuracies, but mobility is limited due to cables and instrument's size, which could

(a) A type of chipboard (b) A type of chipboard

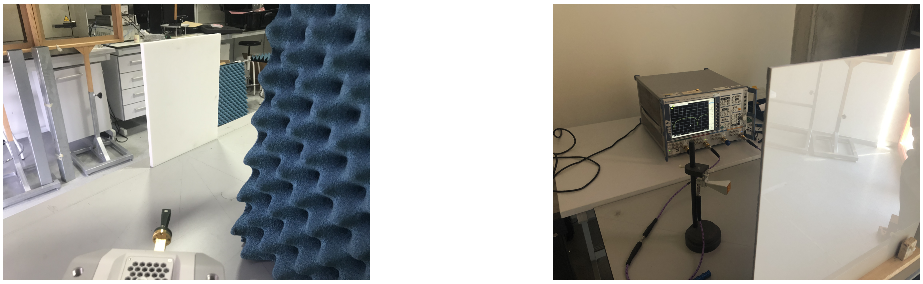

(c) Nylon (d) Tile

Figure 3.10: Samples of tested materials at the Universidad Politécnica de Cartagena in Spain

be a relevant issue for some applications. On the other hand, SCA is a light, portable and easy-to-use measurement kit, useful for on-site measurements even of walls or furniture, but at the cost of a lower sensitivity and resolution. The considered bands are the 8-13 GHz and 26-40 GHz. In this campaign the tested materials were chipboard, marble, sandstone, paraffin and pine wood.

The overall results are shown in Table 3.4 and in Table 3.5.

3.3.2 Validation

In order to understand the effectiveness of the method, accuracy and precision are two important factors to consider when dealing with data measurements. Accuracy refers to the closeness of the measurements to the true value. Precision is the degree to which repeated and reproduced measurements yield the same results, which turns into the spreading of measurements. Moreover, it has been evaluated the applicability of the method to different materials and cases.

Accuracy

Measurements setup is subject to different errors which may come from:

- the variation of the nominal (unknown) value of Δf, due to noise, VNA's

Table 3.1: Impact on the ϵ' estimate of Δf, θ_i and w errors

	Error on Δf	Error on θ_i	Error on w	Total Error
	±10 MHz	±1°	±1mm	
Error on ϵ'	0.56%	0.53%	5.65%	5.70%

resolution, FFT procedure resolution, etc.;

- the non-perfect alignment of the antennas to the nominal reflection and transmission angles of incidence, along with the non-perfect perpendicularity of the slab to the leaning surface, which affect θ_i;
- the non-perfect flatness of the slab, which would result in a slight variation of the thickness along the surface that must be considered as an error on w dimension.

In order to assess the Fabry-Pérot accuracy, the impact of such errors on the real part of the complex permittivity is evaluated. To this aim, error propagation on Δf, θ_i and w, and ϵ' is analyzed. Given a function of n uncorrelated variables x_i, $g(x_1, x_2, ..., x_n)$, each affected by its uncertainty Δx_i ($x_i \pm \Delta x_i$), the uncertainty on $g(x_1, x_2, ..., x_n)$, can be calculated as:

$$\Delta g = \sqrt{\sum_{i=1}^{n} \left(\frac{\delta g}{\delta x_i} \Delta x_i \right)^2} \tag{3.14}$$

In our case the target function g corresponds to the ϵ' in Eq. 3.3, while the error-affected variables (x_i) are Δf, θ_i and w which are considered independent. Table 3.1 shows the relative error on ϵ' as a function of the three sources of error, separately computed using Eq. 3.14, and the total error. Results are computed for $\Delta f = 3$ GHz, $\theta_i = 45°$ and $w = 3$ cm. It is clear that the highest error comes from w.

Precision

Precision is a measure of the variability of the values around the mean and it is defined by repeatability and reproducibility. In [100], the Fabry-Pérot approach has been tested both with a VNA and a portable spectrum analyzer equipment, called Spectrum Compact Analyzer (SCA) kit. The purpose of this study is to show the reproducibility and the usability of the approach using a quite different measurement equipment with respect to the VNA, which is one of the most common one. This second measurement equipment is a very light, portable, battery-powered kit which is an attractive solution because of its portability and easy use, allowing on the field measurement. In [100] the comparison between the two different setups is reported, showing a good agreement.

Different measurements performed on the same materials at the same frequency are shown to get a grasp of the precision of the method. As shown in [101], the precision is good although they have been conducted in different moments, by different operators and with different VNAs, and even in two different labs (in Italy and in Spain). For example, the same paraffin slab has been tested under different conditions at 10 GHz, and results are in very good agreement (see Section 3.4). Also granite has been tested in different conditions at 60 GHz, showing good agreement as well. In [99] the Fabry-Pérot approach is also compared with the open-ended coaxial method, which is a well-known tecnique to estimate the e.m. characteristics of materials. Results of the proposed technique in this work are in good agreement with the open-ended coaxial probe assessment and with literature.

Applicability

There are some aspects that should be considered for the Fabry-Pérot applicability. First of all, it is worthwhile to know a priori an approximate minimum thickness of the slab for observing at least 3-4 adjacent notches, which is related to the measurement bandwidth B. In order to highlight N notches it must be $\Delta f \leq B \cdot (N-1)$. From Eq. 3.6 we can extract a lower bound for the thickness:

$$w_{min} = \frac{c \cdot (N-1)}{2B \cdot \sqrt{\epsilon'_{max} - a}} \tag{3.15}$$

From Eq. 3.15 it is clear as the lower B the higher w_{min}. Fig. 3.5 shows the valid region for Δf for a given value of thickness w. Such value must be greater than w_{min} according to the measurement bandwidth B. For example, the minimum thickness for a brick at $B = 5$ GHz is $w_{min} = 2.92$ cm (considering $\epsilon'_{max} = 10$, $N = 4$ and $\theta_i = 45°$).

Moreover, although "grainy", inhomogeneous materials can be measured with the Fabry-Pérot method as long as the wavelength is much larger than the average grain size, at high frequencies inhomogeneity could generate diffuse scattering and prevent the resonance from taking place. It is interesting to roughly estimate the cut-off frequency at which the Fabry-Pérot resonance ceases to exist as frequency increases: Table 3.2 shows that the cut-off frequency for some inhomogeneous materials. Fig. 3.11 shows examples of reflection frequency responses for a working band (around 60 GHz) and a failing band (around 100 GHz) for chipboard. From Table 3.2 there seems to be a fixed ratio of about 0.3 between the size of grains and the wavelength at the cut off frequency.

Another applicability issue, actually common to many other methods, is that for very-low-conductivity materials the measured transmission coefficient may approach 1, making the estimation of ϵ'' or σ challenging.

Table 3.2: Relation between wavelength and grain size at FB cut-off frequency

	Cut-off frequency est.	Wavelength	Mean grain size est.
Wood	20 GHz	1.500 cm	0.33λ
Chipboard	80 GHz	0.375 cm	0.26λ
Granite	70 GHz	0.430 cm	0.28λ

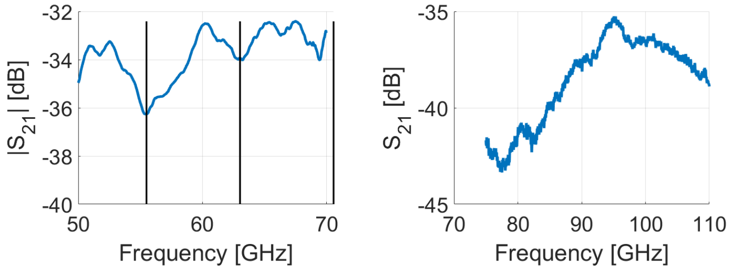

(a) Chipboard in [50-70] GHz (b) Chipboard in [75-110] GHz

Figure 3.11: Working (Fig. 3.11a) and failing (Fig. 3.11b) bands for a Chipboard slab. Black solid lines in Fig. 3.11a highlight the notches' position ($\Delta f = 7.53$ GHz)

.

It is worth noting that ϵ' results are virtually independent of the chosen incidence angle θ_i, as shown in Table 3.3. However, as diffraction on the slab's vertical edges might arise with very large angles, while the antennas could get too close to each other for very small angles and crosstalk effect may corrupt measurements, we decided to use the intermediate angle value $\theta_i = 45°$.

3.4 Validation against literature

In [101] the overall results of the extensive measurement campaign on Fabry-Pérot material characterization is reported. Results are shown also in Table 3.4 and in Table 3.5, in terms of ϵ', σ [S/m] and insertion loss (L_T) [dB]. As can be noted, some materials could not be measured at lower frequencies because the thickness of samples was too small given the considered frequency band (see

Table 3.3: Marble's results at 30 GHz for three different incidence angles

	Δf	ϵ'
$\theta_i = 15°$	1.824	7.561
$\theta_i = 45°$	1.883	7.563
$\theta_i = 60°$	1.893	7.564

Eq. 3.15). As mentioned Section 3.3, the same paraffin slab has been tested with two different measurement setups (see Paraffin* and Paraffin** in 3.4 and 3.5), in two different labs and results are in very good agreement with each other. Values reported in the table are in good agreement with those reported in the literature for similar materials and frequencies [104][116][117]. The conductivity appears to increase with frequency for almost all materials, in agreement with the frequency-dependent formula suggested by ITU [118]. Interestingly, marble represents an exception to the rule, confirming what already found in [113].

Validating measurement methods for material parameters is a quite difficult task. While there is a vast literature on such methods, only in very few cases the error or the confidence level of the measured parameter values are provided [108][116][117][119][120][121][122][123][124][125][126][127]. Moreover, common materials are inhomogeneous and vary quite a lot with the manufacturing method, even between different samples for the same manufacturer. For this reason, we decided to validate the Fabry-Pérot method using reference low-loss materials often used in constructions and in the industry, namely brick-clay, teflon (PTFE), paraffin, sandstone and pine wood, for which some reliable data are available in the literature. Values in Table 4 of [101] (ϵ') are in good agreement with Fabry-Pérot measurements, the error being always below 10% for teflon and paraffin. The error is larger for brick clay. However, brick material is known to be highly variable: we used a relatively thin and dense clay tile used for floor coating, while brick clay for wall construction is usually considered in the literature. It is worth noting that even teflon is quite variable: besides polytetrafluoroethylene (PTFE) considered in the present work, it can also be perfluoroalkoxy alkane (PFA) or fluorinated ethylene propylene (FEP), that have a slightly different composition: unfortunately the exact composition is rarely indicated in the literature. For σ values (Table 5 in [101]) the order of magnitude is always matched by the Fabry-Pérot method, while the exact estimate figure varies quite a lot, not only between Fabry-Pérot and literature references, but even between such different literature results. As stated before, this is partly due to the great variability of building materials [116]. But for very low loss polymers, where the grade of discrepancy can be even of one order of magnitude, the cause is probably the insufficient sensitivity of measurement methods used by researchers compared to the very low value of the loss tangent [127].

Table 3.4: Fabry-Pérot results for 8-13, 26-40 and 50-70 GHz. Gray cell means that no data is available for that case, as no measurements were performed. In green cells the procedure worked properly. Finally, in light red cells, the method failed, due to either one of the two checks not being satisfied or to applicability issues, as highlighted in Fig. 3.1. However, even in this case, the average insertion loss L_T could be estimated: this is a useful side-result of the FP measurement procedure.

Frequency band [GHz]		8-13			26-40			50-70		
Bandwidth [GHz]		5			14			20		
Material	w [cm]	10 GHz			30 GHz			60 GHz		
		ϵ	σ [Sm^{-1}]	L_T [dB]	ϵ	σ [Sm^{-1}]	L_T [dB]	ϵ	σ [Sm^{-1}]	L_T [dB]
Brick	1.5	w too small			5.64	0.13	2.92	5.32	0.27	5.71
Chipboard-1	1.6	w too small			2.19	0.11	2.28	2.04	0.48	9.07
Chipboard-2	1.6	w too small			2.15	0.12	2.46	1.85	0.41	8.09
Chipboard-3	1.0	w too small			5.66	0.12	2.41	4.93	0.92	8.12
Chipboard-4	2.0	2.60	0.15	3.54	2.60	0.26	5.76			
Granite	2.1							5.51	0.42	7.13
								5.53	0.40	7.10
Plaster	2.0	w too small					8.02			10.88
Marble	3.0	6.90	0.15	4.75	7.56	0.06	3.21			
Nylon	0.6	w too small			w too small			w too small		
Paraffin*	3.5	2.00	$0.23 \cdot 10^{-3}$	0.27	2.25	$8.17 \cdot 10^{-3}$	0.67	2.36	0.03	1.51
Paraffin**	3.5	2.03	$0.26 \cdot 10^{-3}$	0.30						
Pine wood	4.5	2.10	0.07	3.85			14.33			
Plywood	1.8			2.25	1.77	0.21	4.82	1.81	0.44	9.82
Sandstone	3.0	7.70	0.09	3.76	6.53	0.25	6.64			
Teflon	1.0	w too small			w too small			w too small		
Tile	0.7	w too small			6.27			5.88	0.59	4.44

Table 3.5: Fabry-Pérot results for 75-110 and 220-330 GHz. Gray cell means that no data is available for that case, as no measurements were performed. In green cells the procedure worked properly. Finally, in red cells, the method failed, due to either one of the two checks not being satisfied or to applicability issues, as highlighted in Fig. 3.1. However, even in this case, the average insertion loss L_T could be estimated: this is a useful side-result of the FP measurement procedure.

Frequency band [GHz]		75-110			220-330		
Bandwidth [GHz]		35			110		
Material	w [cm]	100 GHz			300 GHz		
		ϵ	σ $[Sm^{-1}]$	L_T $[dB]$	ϵ	σ $[Sm^{-1}]$	L_T $[dB]$
Brick	1.5	5.57	0.36	9.28	▨		
Chipboard-1	1.6	🟥		16.51	🟥		46.91
Chipboard-2	1.6	🟥		11.94	🟥		45.29
Chipboard-3	1.0	🟥		10.73	🟥		18.82
Chipboard-4	2.0	▨			▨		
Granite	2.1	🟥		18.51	▨		
		🟥		18.04	▨		
Plaster	2.0	1.71	🟥	🟥	🟥		10.97
Marble	3.0	▨			▨		
Nylon	0.6	3.95	0.13	1.65	3.86	0.66	4.27
Paraffin*	3.5	2.11	0.04	1.87	2.19	0.04	1.88
Paraffin**	3.5	▨			▨		
Pine wood	4.5	▨			▨		
Plywood	1.8	🟥		17.11	🟥		38.06
Sandstone	3.0	▨			▨		
Teflon	1.0	2.22	$4.48{\cdot}10^{-3}$	0.39	2.25	$5.85{\cdot}10^{-3}$	0.42
Tile	0.7	🟥		4.72	🟥		12.88

Chapter 4

mmWave propagation characterization

[In this chapter it is reported the measurement campaign performed at the University of Bologna, extensively discussed in a recently submitted the paper, with the objective of investigating the large-scale spatial characteristics of both indoor and outdoor channels. Measured data is then analyzed through a Ray-Tracing simulation tool. After the validation of the predicted results by simulation, Ray-Tracing is used to get insights into the principal propagation mechanisms at mmWave frequencies. The outcomes of the present work are of particular interest for the calibration of Ray-Tracing tools when used as prediction channel models. This work gives an in-depth analysis of the directional propagation characteristics at two considered mmWave frequencies.

4.1 Measurement campaigns

Channel measurements are essential to get a first insight in understanding the radio propagation. Directional characteristics of the propagation channel are particularly interesting when going up in frequency into the mmWave range. As explained in chapter 2, at these frequencies the use of omnidirectional antennas limits the possible range due to the increase in transmission loss. Beamforming techniques are required to focus the transmission and reception in propagation directions which minimize the losses. All these reasons lead to an overall simplification of the channel at mmWave frequencies, as the channel can mainly address the large-scale directional properties. In this perspective, the full characterization of the channel, which requires a great effort, appears to be worthless. Directional channel characteristics turn out to be much more attractive.

In this work, both indoor and around buildings channel measurements have

Table 4.1: Measurement setup

Frequency	**Gain**	**HPBW**	**TX output power**
27 GHz	20.5 dBi	E-plane: 14° H-plane: 17.5°	+5 dBm
38 GHz	21.5 dBi	E-plane: 11.5° H-plane: 13°	+5 dBm

been carried out at two different frequency bands, 27 GHz and 38 GHz at the University of Bologna. The objective is to investigate the large-scale directional characteristics of indoor and outdoor channels.

4.1.1 Measurement setup

The equipment used to sound the radio channel is a compact, portable kit - Spectrum Compact Analyzer (SCA) by SAF Tehnika [115] - composed of a spectrum analyzer, a continuous wave signal generator and two horn antennas, along with cables, connectors and two tripods. The SCA is a very light, battery-powered analyzer, which is an attractive solution because of its portability and easy use. The signal analyzer is connected through an USB cable to the laptop to store the information of the received signal using a dedicated proprietary software GUI. The signal generator is instead connected to the transmitting antenna. The directive horn antennas operate in the frequency band ranging from 26.5 GHz to 40.5 GHz and the considered frequencies are the 27 GHz and the 38 GHz, as they are two frequencies of interest for 5G. Technical data are reported in Table 4.1. Through a rotating antenna positioner, the receiver is steered to scan the channel from each angular direction, in the azimuth plane (0°-360°), with a step of 15°, for a total of 24 directions.

4.1.2 Measurement description

Indoor channel measurements are conducted in the entrance hall of the University of Bologna, reported in Fig. 4.1. The environment is an open space, almost empty, with sparse corners and a central column, made of travertine. The floor is entirely made of a particular type of marble, while the walls are composed by travertine as well. In the top side of Fig. 4.1, there is a large, windowed glass wall. Ceiling is at a height of 5-6 meters. The arrangement is sketched in Fig. 4.1: the TX unit is located at the bottom-right corner of the figure (blue dot), whereas the RX unit is placed in 11 different central location in the room (red dots), both in LOS (RX1, RX3, RX10, RX11) and in NLOS, in order to test the indoor radio channel in different positions in space. The height of TX and RX antennas is the same for all positions (2.1 m). The environment

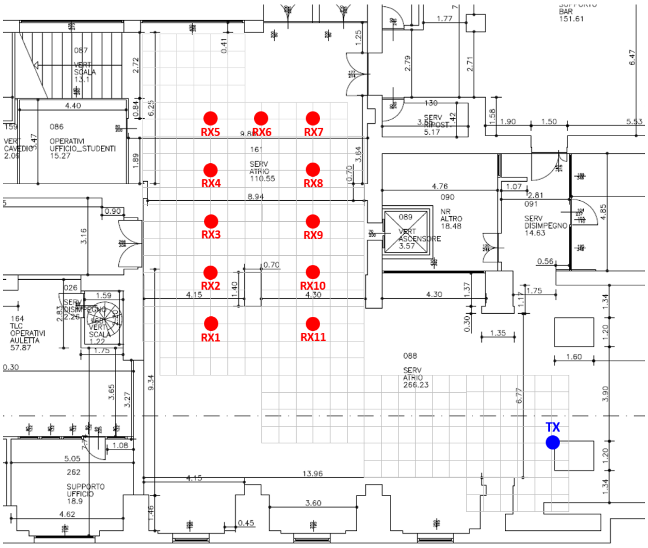

Figure 4.1: Map of the Entrance hall of University of Bologna

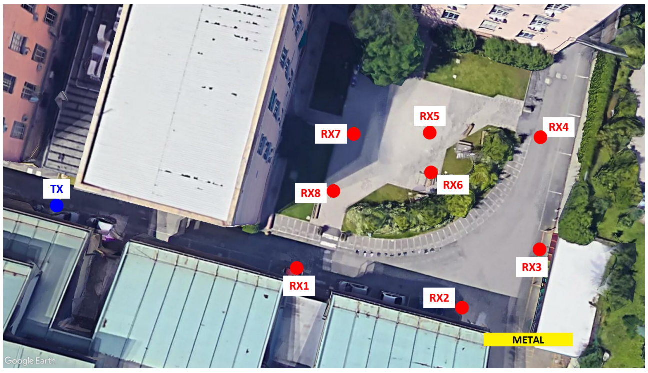

Figure 4.2: Internal yard of the University of Bologna.

is kept almost static during the measurement.

Outdoor channel measurements are conducted in the internal yard, around buildings of the University of Bologna, reported in Fig. 4.2. The environment has an open garden surrounded by high buildings and a short canyon-street, where the transmitter is placed. The construction at the bottom-right corner is made of metal; nearby the garden few cars and scooters were parked. The RX unit is placed in 8 different positions both in LOS (RX1 and RX2) and in NLOS. Also in this case, the height of TX and RX antennas is the same for all positions (2.1 m).

4.2 Ray-Tracing simulation

Ray-Tracing (RT) tools are advanced software belonging to the category of ray-based deterministic models. Based on the Geometric Theory of Propagation (GTP), RT represents the propagation field as a set of rays which undergo various propagation mechanisms such as multiple specular reflections, transmission, diffraction and scattering. With a digitized description of the environment, RT computes all the interactions and the multipath effects between a transmitter and one (or more) receiver(s) and evaluates the evolution of electromagnetic fields along the rays. The digital description of the environment refers to both its geometrical (shape, dimension and position of each object of the environment) and electromagnetic (complex electric permittivity) properties. Along with these inputs, RT requires the description of the radiative characteristics of the antennas and the precise positions of transmitter and receivers. For these reasons, RT predictions are very sensitive to the description of the scenario and antennas.

As outlined in the second chapter, RT represents a very good solution, especially at higher frequencies, to provide accurate, site-specific field prediction and multidimensional characterization of the radio propagation channel [98]. The frequency-agility and the scenario-independent characteristics make RT more flexible and applicable everywhere. Moreover, it is naturally suitable to evaluate the spatial characteristics of the radio channel, providing directly spatial consistency of results. Considering future wireless systems above 6 GHz, with short-medium links, and the wide availability of high-speed computers with GPU, RT has become an efficient, accurate and fast tool for radio channel characterization [97]. The software used for RT simulations in the same environments where measurements have been carried out (see Section 4.1.2) is an advanced 3D RT tool which is a deterministic field prediction software based on the GTP, capable of simulating multipath propagation in indoor and outdoor environments with multiple interactions, including specular reflection, transmission, diffraction, diffuse scattering (through the implementation of Effective Roughness model [128]) and any combination of these. Such tool has been extensively used also in [129], where the dual-directional characteristic of an indoor channel were deeply analyzed.

The objective of RT simulations is two-fold. First, to calibrate and validate the tool against the mmWave channel measurement. In this step, it is essential an item-level investigation on the electromagnetic properties of construction materials (i.e. their complex relative permittivity) using our Fabry-Pérot (FP) method, presented in [101] and discussed in chapter 3, in order to get consistent results. When it is not possible to apply FP, or if it does not provide reliable results, it is possible to perform simple reflectivity measurements to tune both the real and the imaginary part of the complex permittivity. Secondly, RT is

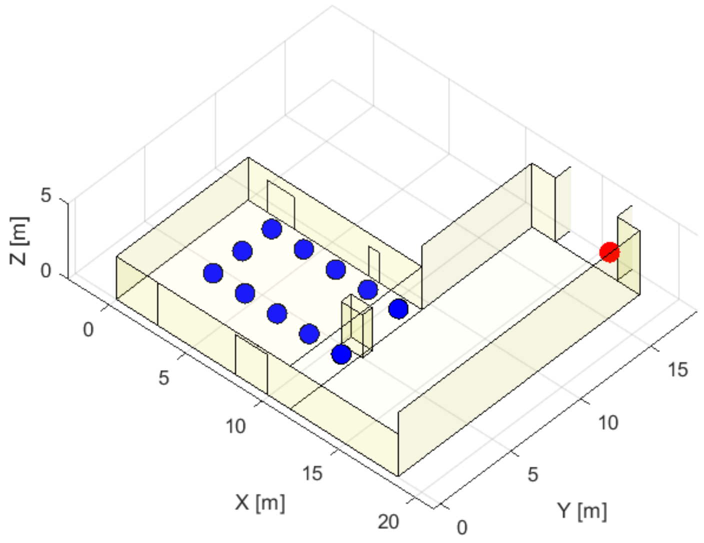

Figure 4.3: Digital representation of the entrance hall environment.

used to further investigate and understand the measured data, by analyzing the main contribution of the principal propagation mechanisms and their relevance.

The final direction is to evaluate RT as a real-time prediction channel tool to assist future beamforming techniques (RT-assisted beamforming [130]). In fact, in future applications, the progresses of environment digitalization, powerful distributed computing and localization techniques will allow the development of advanced beamforming techniques which rely on deterministic propagation models such as RT to perform real-time prediction of the channel's directional characteristics, thus reducing the need of time-consuming exhaustive search techniques to a minimum. If accurate localization is available, directional beamforming can be implemented at any time without any necessity for channel sounding.

4.2.1 Ray-Tracing simulations

The digital map representing the indoor environment of Section 4.1.2 used as geometrical input of the RT tool is depicted in Fig. 4.3. As shown in the figure, only the main structures of the room are considered, such as main walls, floor and ceiling, metal rods and windows. The electromagnetic properties of walls and environment objects have been derived from literature surveys when available. Since little or no information on material parameters were available in literature at 27 GHz and 38 GHz, we first estimated the required material characteristics through our method presented in [99][100][101] to support reliable channel predictions. The settings of the main RT parameters are summarized

Table 4.2: RT main simulation settings

Maximum number of interactions for each ray	20
Maximum number of reflections for each ray	5
Maximum number of diffractions for each ray	2
Maximum number of transmissions for each ray	2
Combined reflections and diffractions	Yes (max. 3)
Combined scattering and reflections	Yes (max. 1)
Angular resolution for ray launching of scattering rays	3.75°

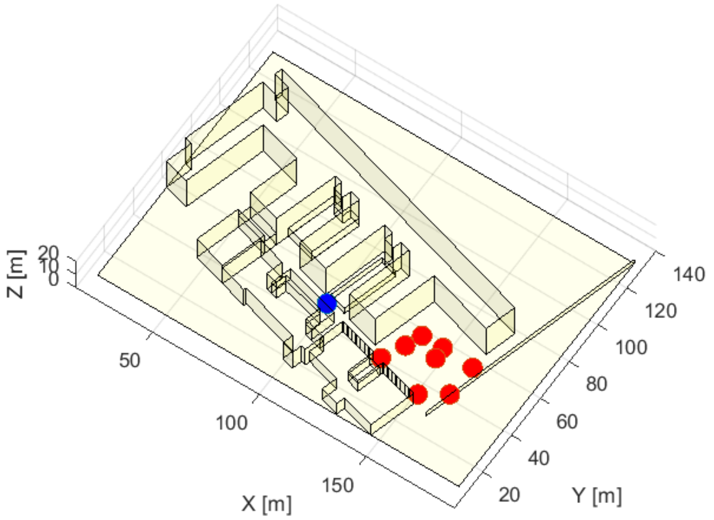

Figure 4.4: Digital representation of the internal yard environment.

in Table 4.2. These parameters were chosen mainly considering the trade-off between computational effort and prediction accuracy. In fact, increasing the number of reflections or transmissions (combined with diffraction and/or scattering in particular) results in a severe increase of simulation time. However, in large indoor and outdoor environments increasing these parameters beyond a certain limit has little or no visible effect. Based on previous experiences with RT tools, the chosen parameters for the considered environments are reasonably tuned to achieve good accuracy (as shown in Section 4.3.3).

For outdoor simulation the digital map representing the environment of Section 4.1.2 is depicted in Fig. 4.4. As for the indoor simulation, the electromagnetic parameters of the environment, have been estimated through the FP method and partially gathered from literature. The main RT parameters are

Table 4.3: RT main simulation settings

Maximum number of interactions for each ray	20
Maximum number of reflections for each ray	4
Maximum number of diffractions for each ray	2
Maximum number of transmissions for each ray	2
Combined reflections and diffractions	Yes (max. 2)
Combined scattering and reflections	Yes (max. 1)
Angular resolution for ray launching of scattering rays	3.75°

sketched in Table 4.3, for which the same consideration for the indoor apply.

4.3 Results

In this section, both indoor and outdoor measurements at the two considered frequencies are analyzed and compared with RT simulations to investigate the channel propagation characteristics and RT performance. By means of RT we extrapolate the principal propagation mechanisms. We also describe how the measured and simulated results are positioned with respect to well-known models, such as 3GPP's.

4.3.1 Narrowband analysis

For both RT simulations and measurements, the received power for each RX position has been computed by adding up power contributions received from all RX antenna orientations. This is a common approach in RT, since usually the incoherent addition of rays is considered, allowing the filtering of fast fading. Moreover, the used measurement kit gives directly the received power by each receiver. The comparison between measured and RT-predicted power is shown in Fig. 4.5 and Fig. 4.6 for both indoor and outdoor scenario respectively. Indoor results confirm a good agreement for all RX positions, with a root mean squared error (RMSE) equal to 1.3710 dBm and 1.5485 dBm for 27 GHz and 38 GHz respectively. Good results also for the outdoor LOS RXs (RX1 and RX2) while the NLOS RXs probably undergo a high fading, as shown in Fig. 4.7, which reports the RMSE for the outdoor case in each RX position.

In order to have an idea about how our results are positioned with respect to reference models, we compare them with the models defined by 3GPP, which have also been adopted by ITU-T for IMT-2020 [8]. For indoor we compared our measured data with the Indoor Hotspot model (InH) in Fig. 4.8. InH scenario is intended to capture various typical indoor deployment cases including offices, open areas, corridors and shopping malls. Transmitters are at a height of 2-3

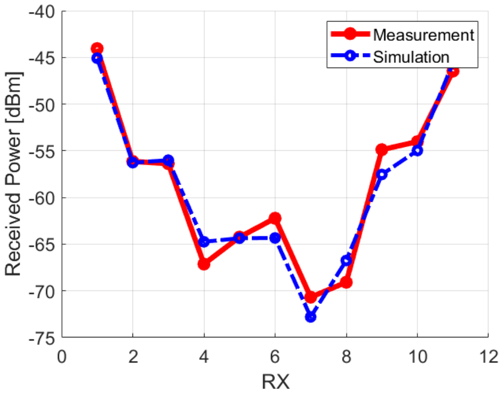

(a) Total received power in indoor environment at 27 GHz.

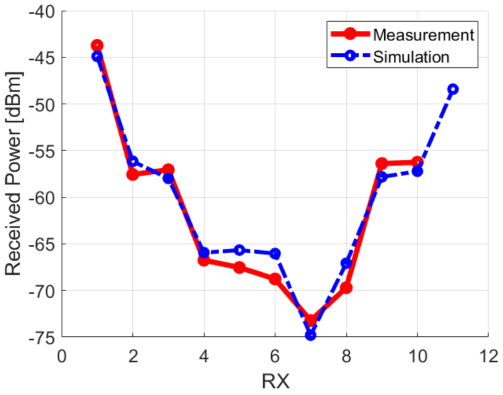

(b) Total received power in indoor environment at 38 GHz.

Figure 4.5: Comparison between measurements and simulation for indoor environment at 27 GHz (Fig. 4.5a) and 38 GHz (Fig. 4.5b).

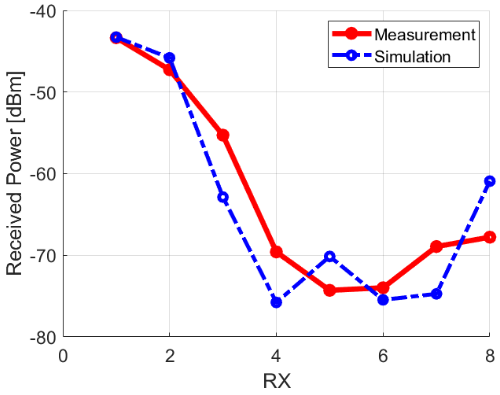

(a) Measurements and simulation for outdoor environment at 27 GHz.

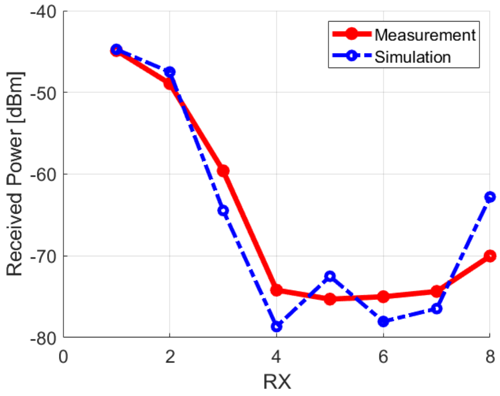

(b) Measurements and simulation for outdoor environment at 38 GHz.

Figure 4.6: Comparison between measurements and simulation around buildings at 27 GHz (Fig. 4.6a) and 38 GHz (Fig. 4.6b).

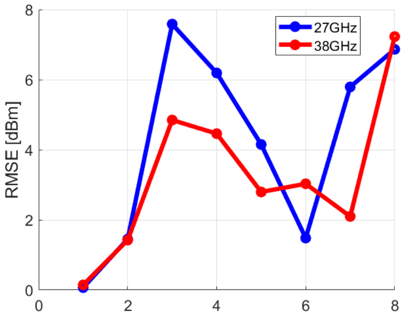

Figure 4.7: RMSE between simulated and measured received powers for outdoor scenario

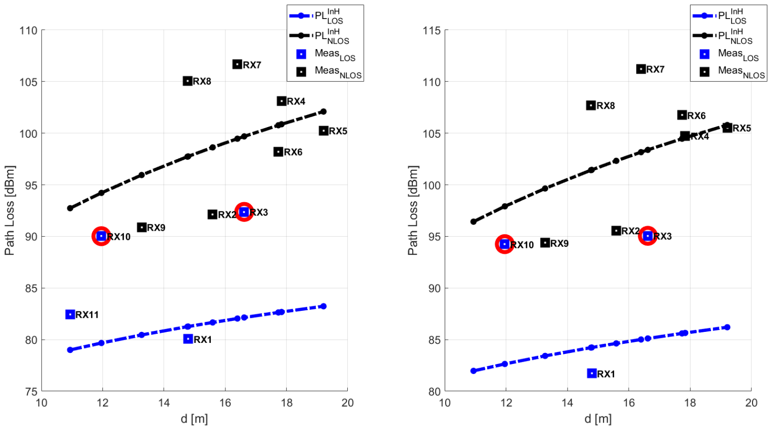

Figure 4.8: Indoor measured path loss compared with 3GPP InH model at 27 GHz (on the left) and at 38 GHz (on the right) frequencies

m while receivers are at a height of 1.5 m. Outdoor data are compared with the Urban Micro (UMi) model, shown in Fig. 4.9. UMi scenario is intended to represent street canyon and open areas, where the transmitter is mounted below the rooftop levels of surrounding buildings (less that 10 m), and the receivers are at a height of 1.5-2.5 m. In both scenarios, there are some RXs which are in a Obstructed LOS (O-LOS) condition, meaning that they are very close to the visibility border. These RXs are the RX3 and RX10 for indoor case, and RX3 for outdoor case. In both Fig. 4.8 and Fig. 4.9, such receivers (highlighted by the red circle marker) have an measured path loss very different from that predicted by 3GPP models. The indoor case it is an evidence of the fact that at mmWaves, close to the shadow boundary, the attenuation is almost the same as in the shadow because of the low contribution of diffraction (as illustrated in Section 4.3.3).

4.3.2 Angular dispersion analysis

In order to investigate the multipath spatial properties, directional results are given in terms of Power Angle Profile (PAP) related to the (azimuth) angle-of-arrival characteristic of the channel and in terms of Angle Spread (AS), which is an important second-order characteristic, characterizing the directivity of the multipath components (MPCs).

PAPs have been derived at the RXs side, exploiting the wide angle-of-arrival range in azimuth (0°-360°). Since the PAPs are related with the measurement environment and antenna locations, to verify the azimuth angle-of-arrival results, they are charted in the environment layout in each RX position, as shown in Fig. 4.10 and Fig. 4.11 for indoor and outdoor respectively. In each sce-

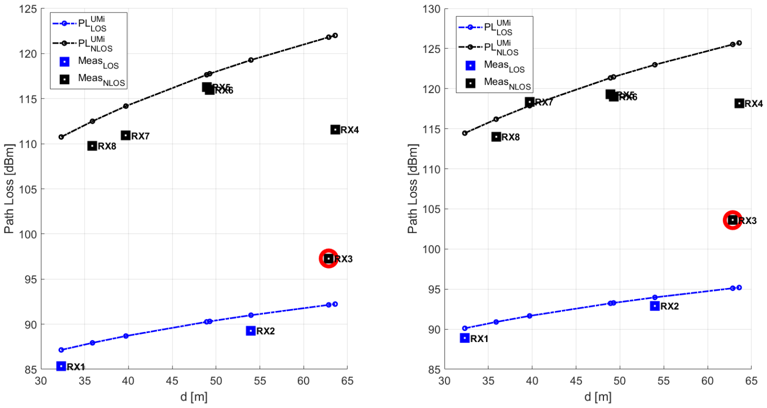

Figure 4.9: Outdoor, measured path loss compared with 3GPP UMi model at 27 GHz (on the left) and at 38 GHz (on the right) frequencies.

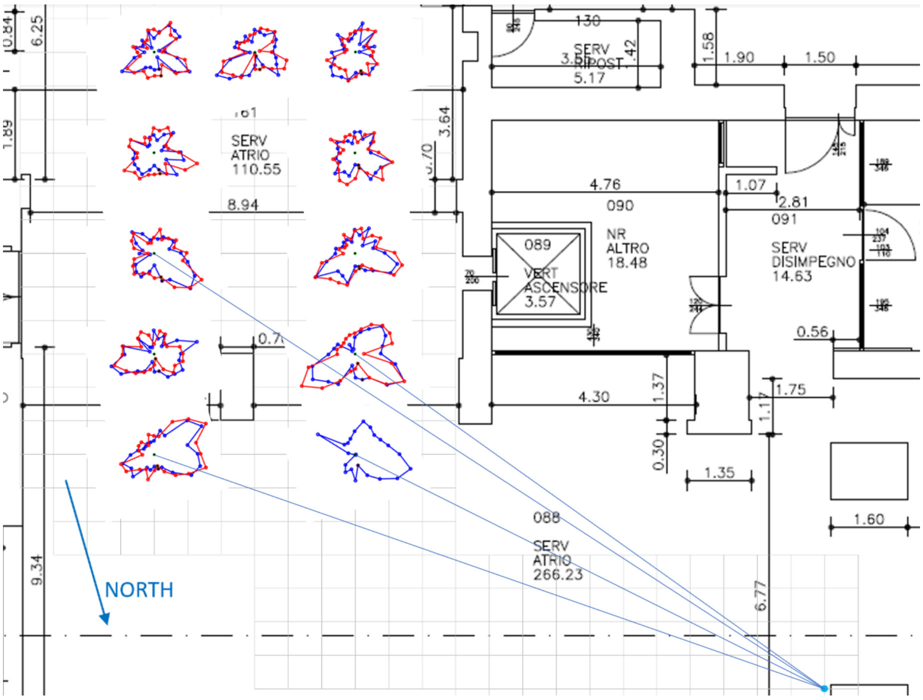

Figure 4.10: Validation of measured PAPs for indoor scenario: 27 GHz in blue; 38 GHz in red.

Figure 4.11: Validation of measured PAPs for outdoor scenario: 27 GHz in blue; 38 GHz in red.

nario, the LOS direction is pointed to the receiver antenna location, while other reflection MPCs can correspond with scatterers in the environment according to the angle information of MPCs. In order to assess the performance of RT we also compared the PAPs for two RX positions, for both indoor and outdoor scenario at 27 GHz frequency, reported in Fig. 4.12 and Fig. 4.13. For the indoor scenario the RMSE, for RX2 and RX11 are 5.1057 dBm and 4.5826 dBm respectively. For the outdoor scenario the RMSE, for RX1 and RX6 are 6.9253 dBm and 9.5844 dBm respectively. Similar results in terms of RMSE are achieved for the 38 GHz frequency. The RMSEs for NLOS RXs are higher with respect to LOS cases.

The AS is related to the angular dispersion of the channel. Fig. 4.14 and Fig. 4.15 show a good agreement between measured and simulated AS at 27 GHz, especially for indoor scenario. Also in this case, similar results are achieved for the 38 GHz frequency. In indoor scenario, RX1, RX3 and RX11 (LOS receivers) have a very low AS with respect to the others, meaning that the space dispersion is lower. The LOS RX10 has an AS comparable to the NLOS RXs. Same remark for RX1 and RX2 in outdoor case. Note that here, RX4 is an outlier, showing a small AS. An interesting outcome from Fig. 4.14 and Fig. 4.15 is that the AS is not correlated to the distance between TX and RXs, neither to the LOS/NLOS condition. In fact, as we can see from both figures, AS of LOS RXs is often lower than that of NLOS RXs. However, the indoor RX10, which is in LOS, has a high AS. This is due to the fact that in

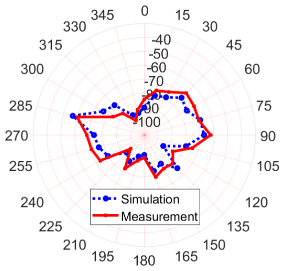

(a) Measured and simulated PAP for RX2 in indoor scenario at 27 GHz

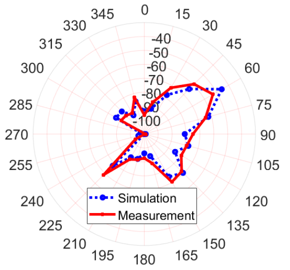

(b) Measured and simulated PAP for RX11 in indoor scenario at 27 GHz

Figure 4.12: Comparison between measured and simulated PAP for indoor scenario at 27 GHz; RX11 (LOS) in Fig. 4.12a; RX2 (NLOS) in Fig. 4.12b

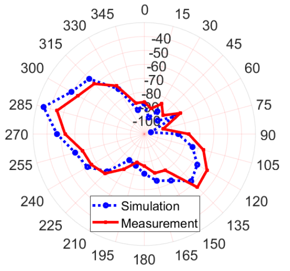

(a) Measured and simulated PAP for RX1 in outdoor scenario at 27 GHz

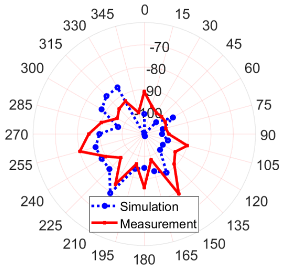

(b) Measured and simulated PAP for RX6 in outdoor scenario at 27 GHz

Figure 4.13: Comparison between measured and simulated PAP for outdoor scenario at 27 GHz; RX1 (LOS) in Fig. 4.13a; RX6 (NLOS) in Fig. 4.13b

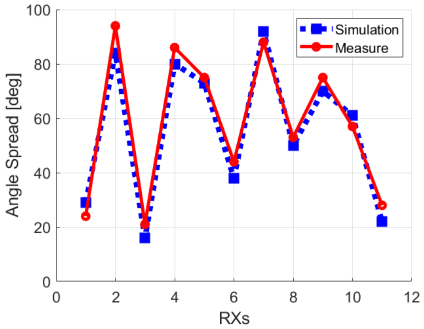

Figure 4.14: Comparison between measured and simulated AS for indoor scenario at 27 GHz

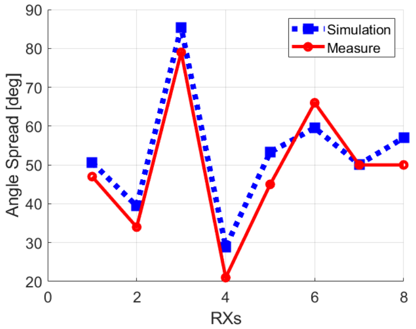

Figure 4.15: Comparison between measured and simulated AS for outdoor scenario at 27 GHz

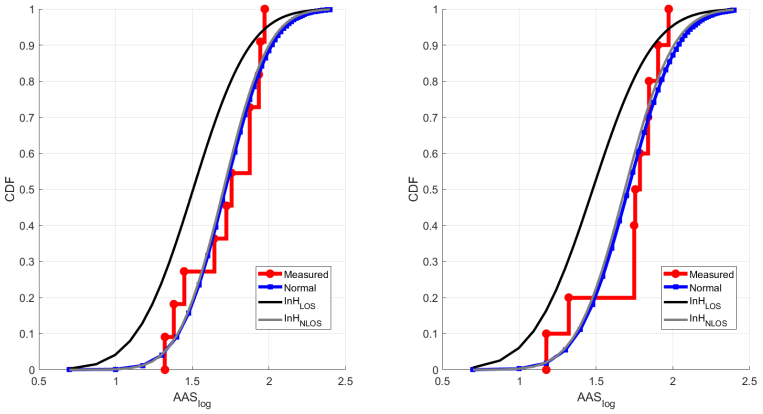

Figure 4.16: Cumulative probability distribution function of Angle Spread in indoor scenario for 27 GHz (on the left) and 38 GHz (on the right)

addition to the strong lobe in the LOS direction, towards the TX, there are also two other strong lobes coming from an intense reflection from the central column and from the wall as it is reported in Fig. 4.10. This leads to a higher power spread in the azimuth dimension even if the receiver is in LOS. On the other hand, taking the NLOS RX4 in the outdoor scenario, positioned at a distance of 64 m from the TX, the AS is quite low. This is due to the fact that the main contribution to the total received power is given by the strong reflection coming from the metal wall as shown in Fig. 4.11. This means that the highest fraction of the total received power comes from one main azimuthal direction, leading to a low AS. The Fig. 4.16 and Fig. 4.17 show the cumulative distribution functions (CDFs) plotted as a function of logarithmic AS, defined as $AS_{log} = log_{10}(AS/1°)$ in [8], for the two considered frequencies in indoor and outdoor scenario respectively. It is worth mentioning that these plots include both LOS and NLOS measurements and should have been split to compare with the LOS and NLOS 3GPP models. In this case the number of LOS scenarios in both environments would not have been statistically large enough. However, in both scenarios even the RXs set in LOS condition are in a quasi-LOS condition, or Obstructed-LOS (OLOS), with the exception of RX1 and R11 in indoor, being close to the shadow boundary. In order to give an idea of how these results relates to 3GPP models, both the LOS and NLOS reference models are reported. The AS for indoor scenario are in the range of 21°-94° for 27 GHz and 15°-93° for 38 GHz, while around buildings the AS are in the range of 21°-79° for 27 GHz and 32°-73° for 38 GHz as indicated in Table 4.4 and Table 4.5. In Fig. 4.16 and Fig. 4.17, all the measured data (in red) are fitted by a Gaussian Normal distribution $N\ (\mu, \sigma)$ (the blue line), where μ and σ are the mean and standard deviation values. The distribution parameters are shown in Table 4.6

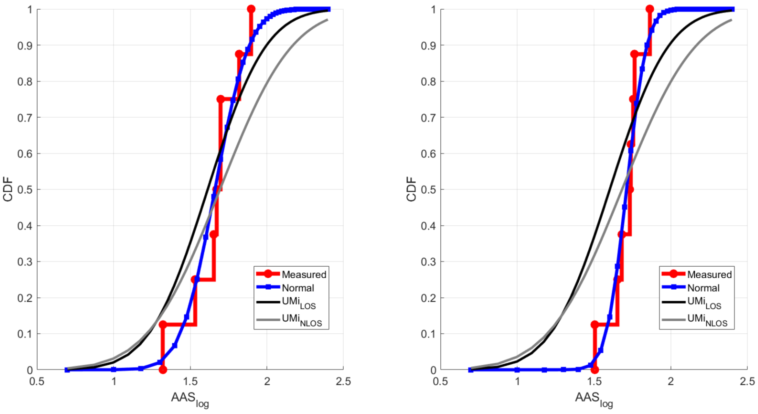

Figure 4.17: Cumulative probability distribution function of Angle Spread in outdoor scenario for 27 GHz (on the left) and 38 GHz (on the right)

Table 4.4: Measured AS for indoor scenario in degree

RX1	RX2	RX3	RX4	RX5	RX6	RX7	RX8	RX9	RX10	RX11
24	94	21	86	75	44	88	53	75	57	28
21	61	15	56	69	80	94	56	70	57	NA

Table 4.5: Measured AS for outdoor scenario in degree

RX1	RX2	RX3	RX4	RX5	RX6	RX7	RX8
47	34	79	21	45	66	50	50
32	45	73	48	57	55	54	58

Table 4.6: Normal distribution and 3GPP AS model parameters for indoor scenario

		Model		**Measurement**	
		μ	σ	μ	σ
27 GHz	LOS	1.5060	0.2927	1.7159	0.2374
	NLOS	1.7038	0.2327		
38 GHz	LOS	1.4787	0.3099	1.7096	0.2555
	NLOS	1.6880	0.2499		

Table 4.7: Normal distribution and 3GPP AS model parameters for outdoor scenario

		Model		**Measurement**	
		μ	σ	μ	σ
27 GHz	LOS	1.6142	0.3003	1.6618	0.1756
	NLOS	1.6942	1.6827		
38 GHz	LOS	1.6027	0.3023	1.7119	0.1041
	NLOS	1.6827	0.3796		

and Table 4.7 for indoor and outdoor scenario respectively. We can see that 38 GHz tends to have smaller AS spread with respect to 28 GHz. In Fig. 4.16 and Fig. 4.17 the measured AS are also compared with the 3GPP models defined in [8]. The indoor measurement are compared with the InH scenario in both LOS and NLOS cases. As we can see the NLOS case fits the measured data very well as shown in Table 4.6. The outdoor scenario is compared with the UMi model defined in [8]. In this case the LOS case fits better the measured data, even though we have a combination of LOS and NLOS RXs, as shown in Table 4.7.

4.3.3 Propagation mechanisms analysis

In order to further investigate the multipath propagation aspects at mmWave frequencies in the considered scenarios, we used RT to calculate the incidence in percentage of the chosen propagation mechanisms (summarized in Table 4.2 and Table 4.3) on the total received power.

Fig. 4.18 and Fig. 4.19 report the simulation results for the indoor scenario at 27 GHz and 38 GHz respectively. As we can see, for LOS RXs, except for RX10, almost the 100% of the total received power comes from the direct ray (L), for both frequencies. The RX10 has a strong contribution from reflection (43%), coming from the central column, as shown in Fig. 4.10. Moreover, diffraction (D) has a low impact, being always the 3% in both cases. Note that, starting from the second-order diffraction we have no contribution, being always under

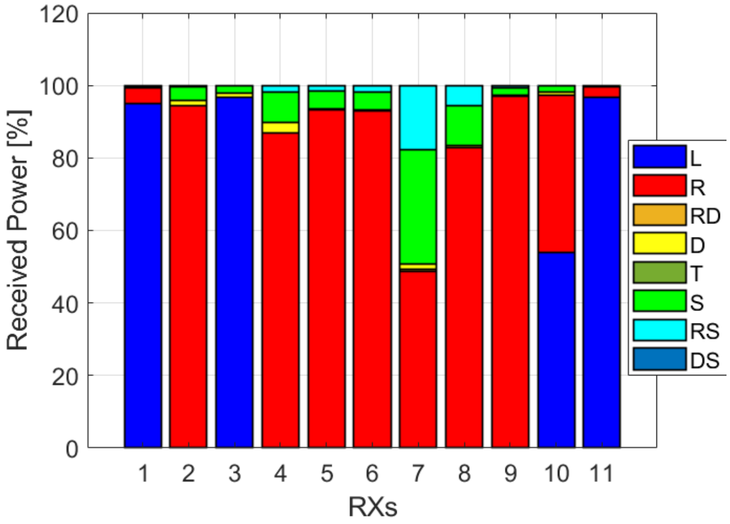

Figure 4.18: Contribution of the different propagation mechanisms on the total received power at 27 GHz: LOS (L); Reflection (R); Reflections with Diffraction (RD); Diffraction (D); Transmission (T); Scattering (S); Reflection with Scattering (RS); Diffraction with Scattering (DS).

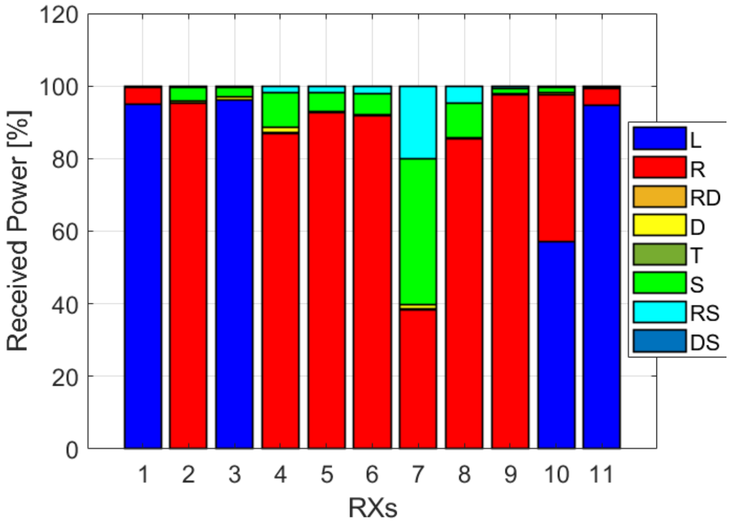

Figure 4.19: Contribution of the different propagation mechanisms on the total received power at 38 GHz: LOS (L); Reflection (R); Reflections with Diffraction (RD); Diffraction (D); Transmission (T); Scattering (S); Reflection with Scattering (RS); Diffraction with Scattering (DS).

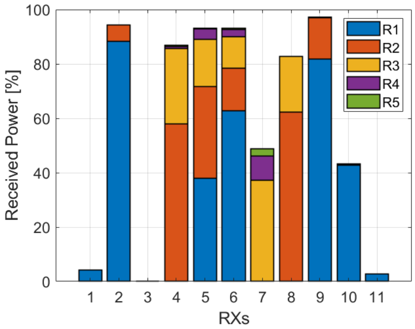

(a) Reflection mechanism for indoor scenario at 27 GHz

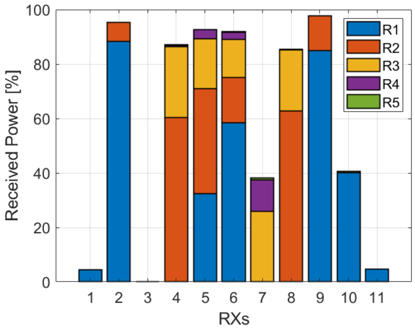

(b) Reflection mechanism for indoor scenario at 38 GHz

Figure 4.20: Insight of Reflection mechanism for 27 GHz (Fig. 4.20a) and 38 GHz (Fig. 4.20b) in Indoor scenario

the 0.0005%. Same conclusion for combined reflections and diffractions (RD), which are always below the 0.5% at both frequencies. Reflection is the main propagation mechanism for NLOS RXs. As shown in Fig. 4.20, also third (and higher)-order reflections are important for deep NLOS RXs, such as RX7. For these RXs, scattering (S) represents one of the main power sources as well. In this case scattering represents the 30% and 40% of the total received power for 27 GHz and 38 GHz frequencies respectively. As indicated in Table 4.2, we also considered combined mechanisms, such as reflections combined with scattering. Adding together reflections, scattering and combined reflections with scattering, we can see that these mechanisms represent almost the total received power for NLOS receivers, at both frequencies as shown in Fig. 4.21. For indoor scenario, no transmissions (T) through walls have been observed at RXs.

For what concerns outdoor analysis, Fig. 4.22 and Fig. 4.23 show simulation results at 27 GHz and 38 GHz respectively. In this case the LOS contribution to the total received power is lower with respect to the indoor scenario. In fact, the direct ray component for RX1 and RX2 is 67% and 48% respectively. However, the TX-RXs distances are higher in outdoor scenario: here the two

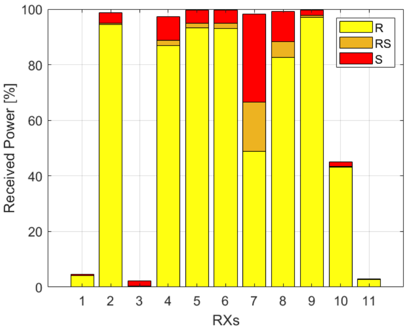

(a) Reflection (R), Scattering (S) and combined Reflection with scattering (RS) for indoor scenario at 27 GHz

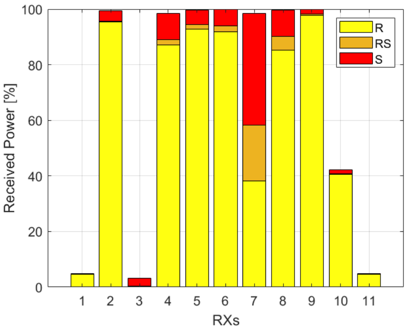

(b) Reflection (R), Scattering (S) and combined Reflection with scattering (RS) for indoor scenario at 38 GHz

Figure 4.21: Reflection, Scattering and combined Reflection with scattering for 27 GHz (Fig. 4.21a) and 38 GHz (Fig. 4.21b) in Indoor scenario

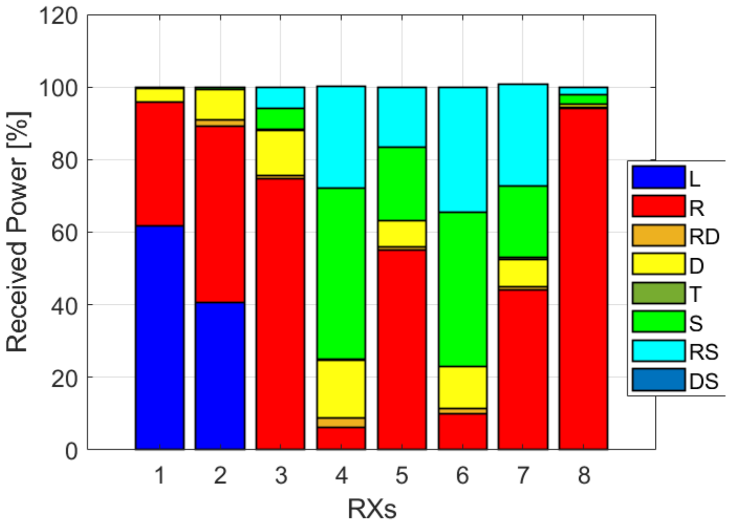

Figure 4.22: Contribution of the different propagation mechanisms on the total received power at 27 GHz: LOS (L); Reflection (R); Reflections with Diffraction (RD); Diffraction (D); Transmission (T); Scattering (S); Reflection with Scattering (RS); Diffraction with Scattering (DS).

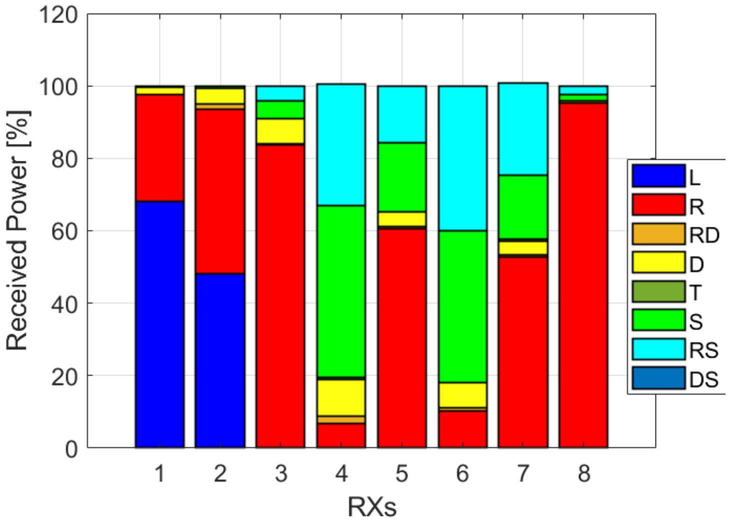

Figure 4.23: Contribution of the different propagation mechanisms on the total received power at 38 GHz: LOS (L); Reflection (R); Reflections with Diffraction (RD); Diffraction (D); Transmission (T); Scattering (S); Reflection with Scattering (RS); Diffraction with Scattering (DS).

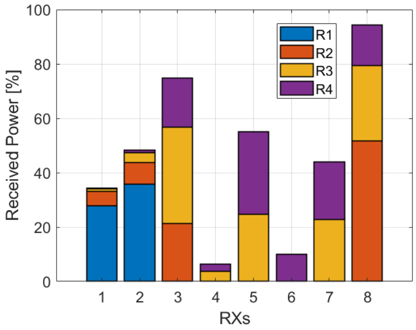

(a) Reflection mechanism for outdoor scenario at 27 GHz

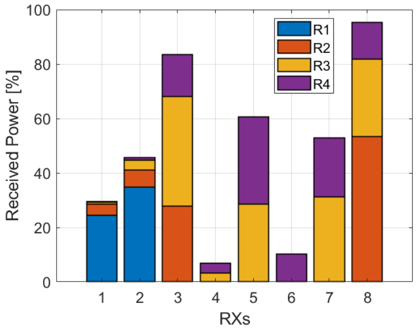

(b) Reflection mechanism for outdoor scenario at 38 GHz

Figure 4.24: Insight of Reflection mechanism for 27 GHz (Fig. 4.24a) and 38 GHz (Fig. 4.24b) in outdoor scenario

LOS RXs are 32 m and 54 m distant, while in the indoor case the farest RX is at 16 m. Around buildings, reflection is significant also for LOS RXs as shown in Fig. 4.24, being greater than 35% for RX1 and almost 50% for RX2 at both frequencies. It appears that, for NLOS RXs that are closer to the buildings, such as RX3, RX5 and RX8 (see Fig. 4.2), reflection is the main propagation mechanism. For NLOS RXs placed in the middle of the yard (RX4 and RX6), scattering and reflections with scattering are essential (see Fig. 4.25). In particular, scattering has a major impact in the outdoor case than the indoor case. Moreover, unlike indoor, around buildings diffraction is higher. In fact, while in the indoor scenario diffraction is always lower the 3%, for outdoor case diffraction reaches values of 10-15%. Even the second-order diffraction has a detectable contribution. As an example, Fig. 4.26 reports the contribution of diffraction in indoor and outdoor scenarios at 27 GHz. Reflections combined with diffraction are higher around buildings, yet with low values (lower than 3%) also in this case. Transmissions through walls have very low values, being always under 1%.

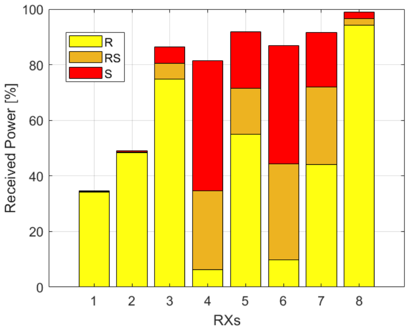

(a) Reflection (R), Scattering (S) and combined Reflection with scattering (RS) for outdoor scenario at 27 GHz

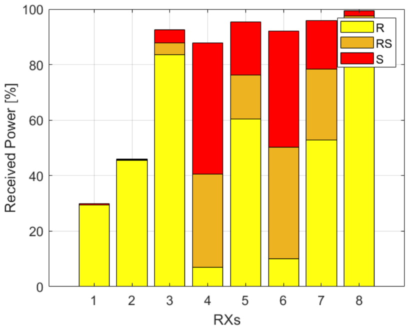

(b) Reflection (R), Scattering (S) and combined Reflection with scattering (RS) for outdoor scenario at 27 GHz

Figure 4.25: Reflection, Scattering and combined Reflection with scattering for 27 GHz (Fig. 4.25a) and 38 GHz (Fig. 4.25b) in outdoor scenario

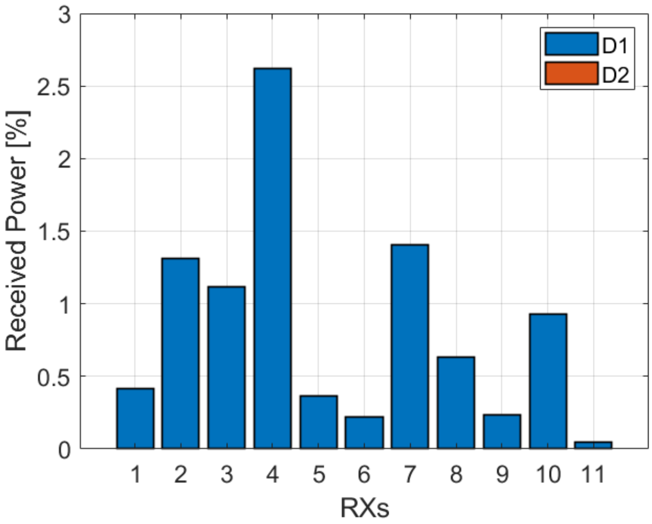

(a) Diffraction mechanism a 27 GHz for indoor

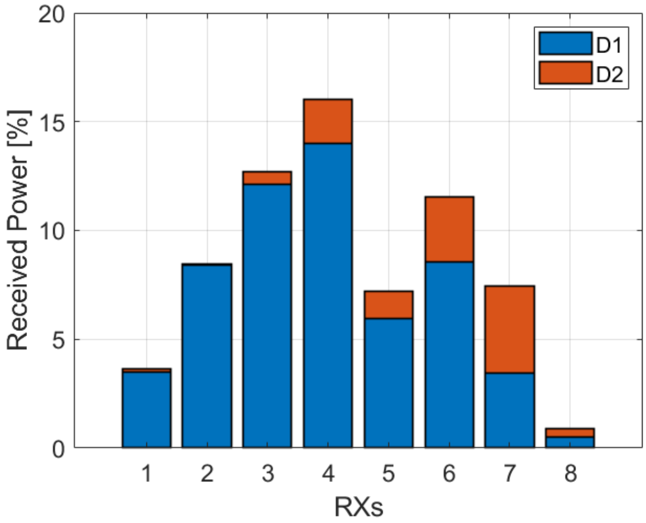

(b) Diffraction mechanism a 27 GHz for outdoor

Figure 4.26: Insight of Diffraction mechanism a 27 GHz for indoor (left) and outdoor (right) scenarios

Part II

Open RAN: the next evolution of Cloud RAN

Chapter 5

RAN's Evolution

This chapter presents an overview of the evolution of radio access networks, highlighting the reasons that led to the current schemes. Although actual Radio Access Network (RAN) architectures have reached a very cutting-edge condition, there are still some questions to deal with, especially considering the requirements set by the forthcoming 5G systems. This leads to the new concept of functional split, which is described in this chapter. Functional splits and the emerging need for interoperability set the basis for the work of the next chapter.

5.1 Mobile wireless networks

The road towards the next generation of mobile communication has led research and industry in the direction of a centralized processing, known as Cloud Radio Access Network (C-RAN) [131]. C-RAN is a novel mobile network architecture which can address a number of challenges the operators are facing in order to meet the continuously growing customers' needs. Since the first generation of mobile networks, the popularity of mobile phones has dramatically increased. This has led to an industry where operators constantly need to renew their networks in order to fulfill the customers' demands yet keeping the costs down in order to offer competitive prices. In particular, the demand on RAN's efficiency, flexibility and scalability forced a radical review of traditional network architecture. In such a context, novel architectures that optimize cost and energy consumption become a necessity in view of the next generation of wireless systems.

Wireless communication networks provide users with network coverage that can be used for transmission of voice and data. Such networks make use of radio waves (hence the name of *radio networks*) to transfer the information between users. Among wireless networks, mobile wireless networks allow mobile users to communicate with other fixed or mobile users. A mobile wireless network,

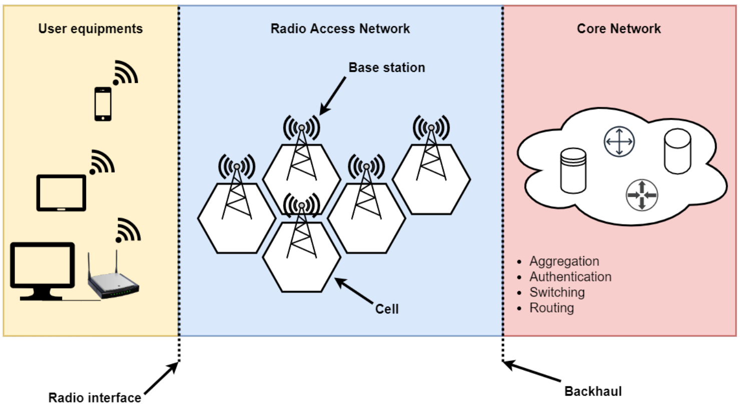

Figure 5.1: High-level architecture of a mobile wireless network

depicted in Fig. 5.1 divides its functionalities into geometrically smaller areas called *cells*, with each cell covered by a radio *base station*, typically mounted on towers or high buildings, owned by tower companies, service providers etc. These collection of base stations form the *Radio Access Network* (RAN). Mobile devices (smartphones, tablets, laptops, etc.), also called *user equipments* within each cell communicate with the base station (usually the nearest) via radio through the air interface (the radio interface) for voice and data communication. The signal is then transmitted to the *core network* either via cables or high-frequency radio links through the **backhaul network**. The core network is the central part of the overall mobile network. It allows users to get access to the services that they are entitled to use and it is responsible for critical functions such as subscriber profile information, subscriber location, authentication of services and the necessary aggregation and switching functions for voice and data sessions.

5.2 RAN's evolution

Since the first deployments, over the last several years RAN architectures evolved. In the traditional 1G and 2G architectures, radio and baseband processing functionalities were integrated inside the base station as shown in Fig. 5.2. The antenna module was generally located in the proximity of the radio module as coaxial cables employed to connect them exhibit high losses.

In 3G mobile networks it was introduced the idea of separating the functionalities of the base station into two different physical units:

- **Baseband Unit - BBU** which acts as a digital unit implementing the base station's functionalities from baseband processing to packet processing;

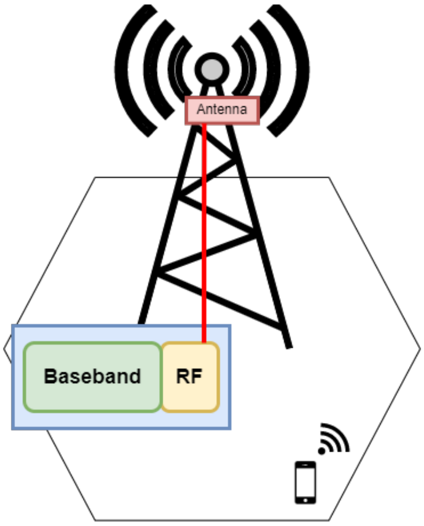

Figure 5.2: Traditional base station

- **Remote Radio Unit - RRU** (also called Remote Radio Head (RRH), according to its complexity), which performs radio functions, including frequency conversion, power amplification, filtering, digital to analog conversion, analog to digital conversion, creating the analog transmit radio signal from the baseband signal and sourcing it to the antennas.

5.2.1 Distributed RAN

In traditional 3G RANs, base stations were deployed in a distributed fashion (D-RAN), in which each base station at the site tower consists of a collocated BBU at the base and an RRU at the top. The RRU embodied only the radio functions and was located close to the antenna in the cell site tower, where the BBU contained all baseband processing functions. Each RRU and BBU pair was connected by a high speed, low latency and highly reliable transport link called **fronthaul network**. The fronthaul was most often a point to point connection, and the radio signals were transmitted using mainly the Common Public Radio Interface (CPRI) [132] (other used protocol are the Open Base Station Architecture Initiative (OBSAI) [133] or Open Radio Interface (ORI) [134] protocols). The BBU is then connected to the core network via the backhaul network.

The increasing traffic requirements, the introduction of various air-interface standards and the emerging of new services induced a tough challenge on D-RAN architectures. In particular, the main challenge the D-RANs had to face was two-fold: find a way to increase bandwidth capacity that is both economical and scalable, allowing for future growth, and do so in a way that reduces the total costs of ownership. To meet such requirements in an energy-efficient

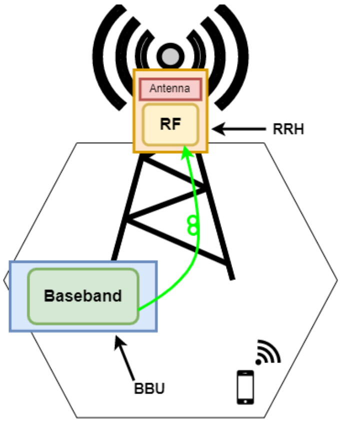

Figure 5.3: Distributed RAN

way there are several alternatives: the first option is to improve the spectrum efficiency by employing more advanced transmission techniques such as Multi Input Multi Output (MIMO) and beamforming. There has been significant progress on this aspect in recent decades, but now we are approaching the theoretical limit. The second option is to exploit spectrum holes through dynamic spectrum access technologies such as cognitive radio, but it cannot ensure consistent and reliable services, and the growth of data capacity is also limited. The third option is to deploy more cells with smaller size (densification and heterogeneous networks) and take full advantage of frequency reuse, which will introduce more interference and increase the cost of infrastructure operation and management. Cell densification is considered a key solution in order to realize the required enhancements [135]. However, increasing cell sites will cause major capital expenditure (capex) and operating expenditure (opex) concerns which would significantly limit the number of base stations that could be deployed by service providers.

5.2.2 Centralized RAN

With the emerging of 4G standards and the necessity to mitigate the operators' capex and opex, novel architectured that optimize costs and energy consumption become essential. In this context, mobile RAN has slightly evolved to a full centralized architecture known as Centralized RAN (C-RAN), introduced by IBM [136]. In this novel architecture the baseband processing moved to a centralized location and BBUs are no longer at the macro site but deployed and aggregated in remote locations, still hardware-based, known as *BBU Pools*, whereas the RRU radio functionalities remain in edge locations and the radio frequency signals are transmitted at the cell sites via the fronthaul network through an Optical Transmission Network (OTN). The basic idea is to collect

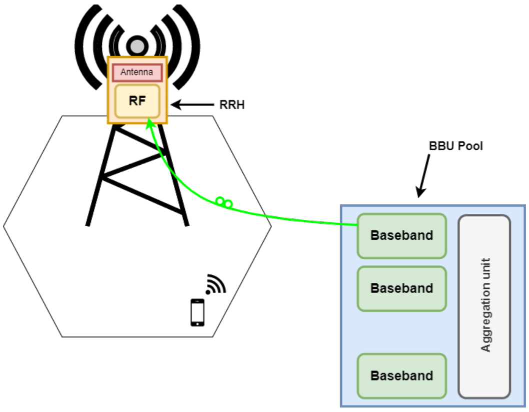

Figure 5.4: Centralized RAN

the BBUs from multiple base stations into centralized BBU clusters and deploy the access nodes as close as possible to the end users, in order to satisfy the required Quality of Service (QoS) and maximize the system throughput.

C-RAN addressed the issues of both maintenance and spectral efficiency, resulting in higher capacity support. The advantages of a centralized architecture are numerous. In C-RAN, a centralized control section provides performance benefits through inter-cell and inter-frequency coordination. In fact, since BBUs from many sites are co-located in one pool, they can interact with lower delays – therefore mechanisms introduced to increase spectral efficiency and throughput, such as enhanced ICIC (eICIC) and Coordinated Multi-Point (CoMP) are greatly facilitated. New BBUs can be added and upgraded easily, improving the RAN scalability. The centralized installation of equipment provides cost benefits through resource pooling and reduced number of cell sites, decreasing or eliminating resources previously required at each site (thus mitigating capex and opex), minimizing the Operation and Maintenance (OAM) efforts as multiple BBUs can be serviced by one technician in a single visit and reducing power and energy consumption compared to the traditional RAN architecture. Furthermore, the centralization evolution is also required in order to support Multi-Radio Access Technology (Multi-RAT) feature and seamlessly integrate new radio access technologies with existing ones.

5.2.3 Cloud RAN

With the introduction of new advanced technologies such as Network Functions Virtualization (NFV) and Software-Defined Networking (SDN), centralized RANs moved towards Cloud RANs, also called Virtual RANs (V-RAN) [137][138]. Based on the developments in softwarization, virtualization and resource coordination, SDN and NFV techniques introduced the concept of BBU-

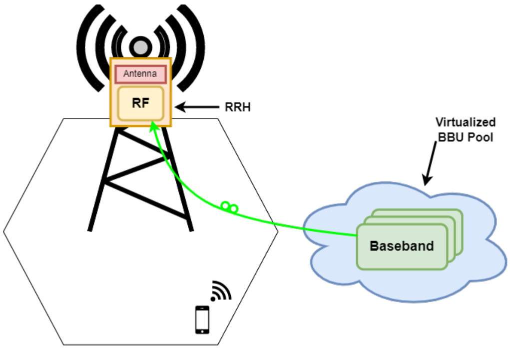

Figure 5.5: Cloud RAN

pool virtualization and shared processing, allowing to distribute the available processing resources among several sites. In particular, NFV performs the abstraction of features from the underlying hardware-based network functionalities. Network functions traditionally run on proprietary and dedicated hardware. By adopting NFV features, virtualized network functions can be deployed in general-purpose commercial-off-the-shelf (COTS) hardware allowing to realize the hardware-based baseband functionalities in a software fashion. In this way, in a further evolution of the centralized RAN, cloud RANs, depicted in Fig. 5.5, BBUs can be not only centralized but also virtualized and coordinated by a centralized entity, in order to optimize resource management [136]. Cloud RAN is a new paradigm of advanced 4G networks and it is envisioned to be one of the key enablers of 5G RANs [139][140][141].

5.3 Towards an Open RAN

However, despite the promising advantages of Cloud RAN such as improved spectral and energy efficiency and lower capex and opex compared to conventional architectures, the main drawback of this fully centralized RAN architecture is the high bandwidth and latency requirements imposed on the fronthaul links [140]. The capacity demand on the fronthaul network is extremely high and with the advent of 5G the traffic is growing to volumes where capacity demanding fronthaul bitrates are non-affordable [142].

5.3.1 CPRI fronthaul challenges

Cloud RAN architecture has been adopted by operators for their RANs in advanced 4G deployments. As described in Section 5.2, C-RAN connects a baseband processing section (BBU) in centralized base station equipments, called BBU Pool, to multiple units of radio equipment (the RRUs) via the fronthaul network. The fronthaul network forwards the digitized baseband IQ (in-phase and quadrature) samples to the BBU in uplink and to the RRU in downlink using CPRI. The CPRI specifications have come to be used in most of conventional C-RAN for fronthaul interfaces.

Such protocol was developed for local link between BBU and RRU in D-RAN. However, first implementations of C-RAN fronthaul are still CPRI based. With the increase of the distance between RRUs and the BBU Pool, the fronthaul link will be extended in the range of kms, therefore traditional CPRI will not be the proper solution. In fact, the strict 5G requirements in terms of high bandwidth and low delay, leads to a further evolution of fronthaul and interface redesigning.

In addition, one of the most significant issues of CPRI is that the required data rate is related to the number of antennas, rather than the actual mobile traffic load. This means that the bandwidth demand will be dramatically growing when the scale of antenna array becomes larger and larger, as effect of massive MIMO deployments [143][144].

Moreover, CPRI does not deliver a full interface standardization that would allow a true interoperability among different vendors and do not sufficiently prescribe specification for fronthaul interfaces [145].

5.3.2 Functional split

In order to reduce fronthaul requirements it was introduced the concept of *functional split*. A functional split determines the amount of signal processing functionalities left locally at the antenna site (RRU), and the amount of functions centralized at BBU level. Fronthaul bandwidth in C-RAN can be significantly reduced with an appropriate functional split by offloading more signal processing functionalities from the BBU to the RRU. However, this not only reduces the acclaimed centralization benefits but also increases the complexity of the RRU. Considering the practical aspects such as power consumption, cost, size and weight, it is often desiderable to make RRU as simple, yet efficient, as possible. Hence, functional split decisions involve trade-offs as shown in Fig. 5.6: offloading more processing functionalities to the RRUs lowers the fronthaul demands but makes them more complex; on the other hand the more functional centralization, the higher the performance and the more efficient the coordination across the network, yet with higher fronthaul capacity requirements. Moreover, also latency is challenging: the more processing performed at the BBU side, the greater the latency introduced before transmission.

Several functional splits have been proposed by different organizations, e.g., Small Cell Forum (SCF) [146], Next Generation Mobile Networks (NGMN) [147], Next Generation Fronthaul Interface (NGFI) [148] and 3GPP [149], which have been investigated to be used for 5G. A complete survey and analysis on functional splits can be found in [142].

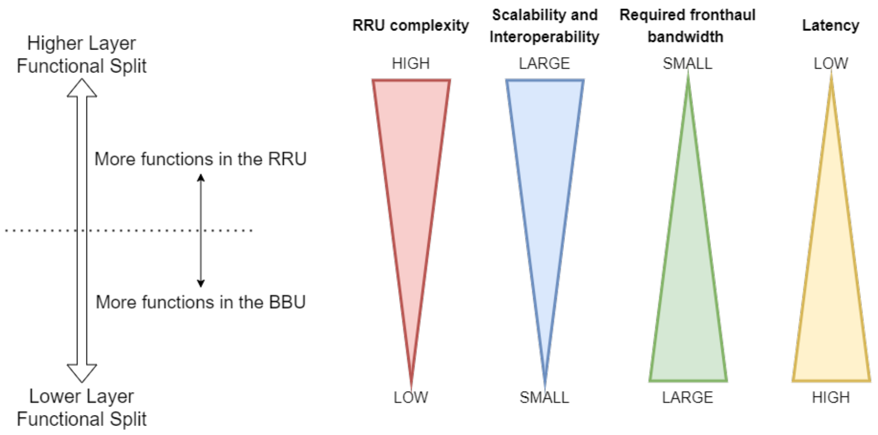

Figure 5.6: Trade-offs in functional splitting between BBU and RRU

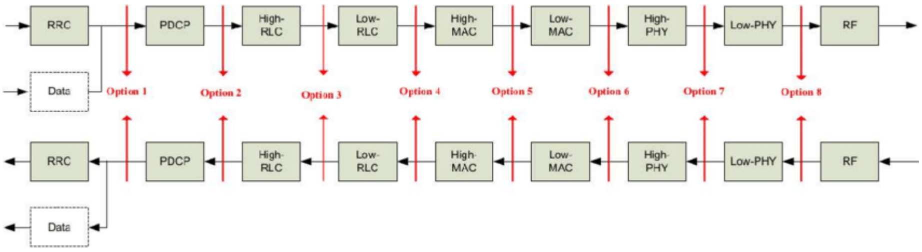

Figure 5.7: Functional splits proposed by 3GPP [150] marked by red lines

In particular, 3GPP has proposed eight functional splits in [150] (depicted in Fig. 5.7), including several sub-options. The red lines within Fig. 5.7 illustrate different options for functional splits: on the left of red line there are the functions implemented in the BBU, while the functions on the right are performed in the RRU. Option 1 has the largest amount of functions in the BBU and option 8 has the least amount of functions in the BBU, corresponding to the traditional split used in CPRI systems. The options 2, 3 and 7 consider also sub-options [142].

The Technical Report on ransport network support of IMT-2020 [151], by the ITU Telecommunication Standardization Sector (ITU-T), summarizes the 3GPP 5G architecture, referring to both *one tier* and *two tier* functional splits, allowing one or two functional splits within the 5G base station, namely to Remote Unit (RU), Distributed Unit (DU) and Centralized Unit (CU).

3GPP New Generation RAN Architecture

Fig. 5.8 shows the 3GPP RAN architecture for New Generation (NG) systems. The NG-RAN consists of a number of new-generation base stations (gNBs) connected to the 5G core network (5GC) via the NG logical inter-

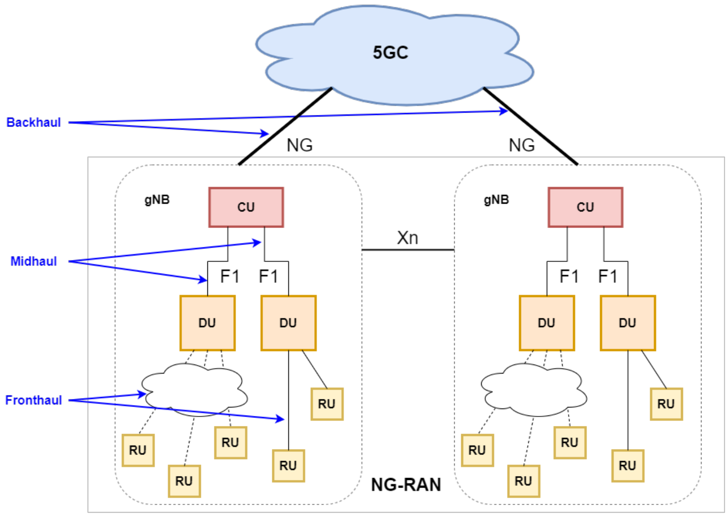

Figure 5.8: 3GPP NG-RAN architecture [151]

face. The gNBs can be interconnected through the Xn logical interface. A gNB consists of a gNB-Centralized Unit (gNB-CU) and gNB-Distributed Unit (gNB-DU). The CU processes non-real time protocols and services, and the DU processes PHY level protocol and real time services. A gNB-CU and the gNB-DU units are connected via F1 logical interface. In such architecture, three networs segments are defined: the fronthaul is the network between the Remote Unit (RU) and DU; midhaul is the network between DU and CU (F1 interface); backhaul is the network between gNBs and 5GC (NG interfaces). Note that the fronthaul network can be based on conventional OTN or on packet-swiched networks (such as Ethernet networks).

In this architecture, it is possible to have a single functional split (one tier functional split) or two functional splits (two tier functional split). The latter case leads to the definition of a low layer functional split (LLFS) and a high layer functional split (HLFS). The fronthaul would typically be based on LLFS and the midhaul would typically be based on HLFS. The motivations for the evolution to 5G transport architecture - where main change is that the original BBU-RRU system is split into three parts (CU, DU and RU) - are discussed in [152]. The 5G transport network may contain fronthaul, midhaul and backhaul networks and operators may use different deployment scenarios, as those shown in Fig. 5.9. In particular four RAN deployments have been identified, based on current wireless network applications.

- Independent CU, DU and RU locations: in this scenario there are fronthaul, midhaul and backhaul networs. The distance between an RU and DU is in the range of 0-20 km, while the distance between the DU and

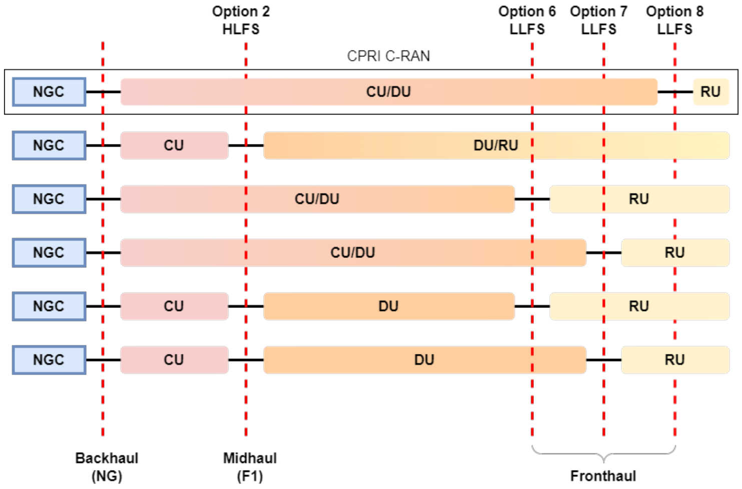

Figure 5.9: Examples of RAN deployment scenarios according to the split points

CU is up to tens of km;

- Colocated CU and DU: In this scenario, the CU and DU are located together, consequently there is no midhaul;
- DU and RU integration: In this scenario, an RU and DU are deployed close to each other. In this case, there are midhaul and backhaul networks.
- CU, DU and RU integration: This network structure may be used for small cell and hot-spot scenarios. In this case there is only backhaul.

However, the final application scenarios will be defined by wireless specifications, transport technology and operators' deployment requirements.

5.3.3 Need of interoperability

As shown in the above sections, along with CPRI limitations on C-RAN fronthaul networks, there is also the fact that CPRI does not deliver a full interface standardization for fronthaul links. As a result there are now many regions having original specifications prescribed by different vendors. This situation has led to a problem of interoperability between baseband processing equipment and radio equipment from different vendors. On the other hand, functional split creates an opportunity for the CU, DU and RU to be produced by different vendors, to enhance competitiveness among equipment and software vendors. A recent trend is that companies form consortia, where innovative solutions from different vendors can be integrated. In this context it is explicit the need for interoperability and open-standard technologies to overcome the limits of current C-RAN architectures.

To this aim the xRAN forum, founded by AT&T, Deutsche Telekom and SK Telecom in October 2016, points at developing, standardizing and promoting a software-based, eXtensible RAN (xRAN) architecture [153]. xRAN architecture decouples control- and data-plane, builds a modular base station operating on COTS hardware, as well as publishes open interfaces. Then, with the integration of the xRAN Forum into the O-RAN Alliance in March 2019, these specifications continued on as Open RAN (O-RAN) fronthaul specifications which are outlined in the next chapter.

Chapter 6

O-RAN Radio Synchronization

This final chapter presents the main activity carried out on the synchronization problems of an O-RAN-compliant RU. After a brief overview of the O-RAN specification, it is described the problem of synchronization in packet-switched networks. Finally, it is described the FPGA project of the O-RAN Synchronization Plane for a target RU, based on the new O-RAN functional split specifications and ITU-T G.8275.1 Telecom Profile.

6.1 O-RAN Protocol Overview

In the previous chapter, it has been presented the main challenge the current CPRI-based RANs are facing. The centralization and virtualization features brought many advantages in terms of costs, efficiency and throughput. On the other hand, fronthaul bandwidth requirements were extremely increasing. Functional splits were proposed in order to mitigate such requirements.

The Open RAN (O-RAN) specifications [154] were formulated against this background and are expected to help in making multi-vendor RANs (that is the possibility to connect any vendor DU to any vendor RU) a reality in the 5G era. Moreover, in the face of this bandwidth problem, O-RAN fronthaul specifications include a new provision for functional split called *Split Option 7-2x*, that places in the remote unit some PHY functions traditionally located in the baseband processing section.

6.1.1 Split Option 7-2x

As explained in chapter 5, when considering a LLFS defining a fronthaul interface there are two competing interests: on one hand there is a benefit in

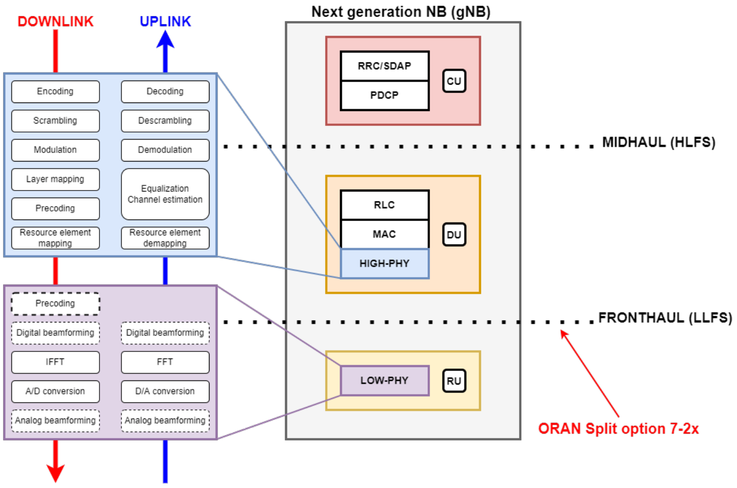

Figure 6.1: Split option 7-2x adopted in O-RAN fronthaul specifications.

keeping the RU as simple as possible because size, weight, and power draw are primary deciding considerations and the more complex the RU, the larger, heavier and more power-hungry the RU tends to be; on the other hand there is a benefit in having the interface at a higher level which tends to reduce the interface throughput relative to a lower-level interface – but the higher-level the interface, the more complex the RU tends to be.

In order to answer to this question, O-RAN has selected a single split point, known as Split Option 7-2x [155]. Split Option 7-2x is a specification for functional split between the O-RAN DU (O-DU) and O-RAN RU (O-RU) depicted in Fig. 6.1. Such split option allows a variation, with the *Precoding* function to be located either above the interface in the O-DU (therefore an O-RU of lower complexity, called O-RU Category A) or below the interface in the O-RU (O-RU Category B). Category A O-RU is expected to be the O-RU implementation of choice in 5G initial deployments.

In downlink processing flow, the user bit sequence received from the MAC layer undergoes various processing operations (indicated in Fig. 6.1), resulting in an I/Q sampling sequence of an Orthogonal Frequency Division Multiplexing (OFDM) signal in the frequency domain. Such IQ samples travel through the fronthaul network (either an OTN or a packet-switched network) and is then subjected to Inverse Fast Fourier Transform (IFFT), converting the sequence into an OFDM signal in the time domain. Finally, this signal is first sent to a digital to analog converter and then to the radio interface. In this flow, both digital and analog beamforming can be optionally performed.

In the uplink flow the coming time-domain signal from the radio interface undergoes the same, reversed operations backwards.

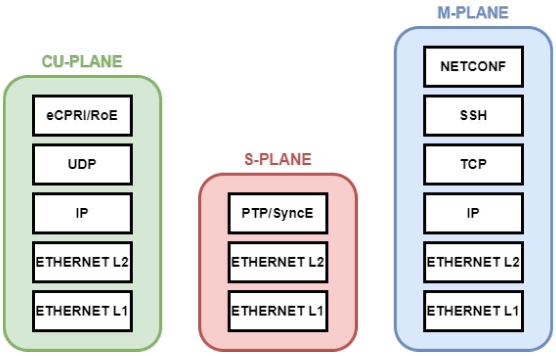

Figure 6.2: O-RAN protocol stack.

The detailed downlink and uplink processing flow are described in [155].

6.1.2 Protocol architecture

O-RAN specification defines four planes of operation:

- **Control Plane (C)**: C-plane messages define the scheduling, coordination required for data transfer, beamforming and mixed numerology handling;
- **User Plane (U)**: U-plane messages are used for efficient data transfer within the strict time limits of 5G numerologies, supporting data compression, DL data precoding, and I/Q data transfer;
- **Synchronization Plane (S)**: S-plane is responsible for the synchronization aspects between the O-DU and O-RU (see Section 6.2);
- **Management Plane (M)**: M-plane messages are used to manage the RU. It provides a variety of O-RU management functions to set parameters on the O-RU side as required by the CU planes and S plane, e.g. manage O-RU software, perform fault management, etc.

Fig. 6.2 shows the protocol stack defined for O-RAN specifications. In the CU planes, O-RAN supports a protocol stack that transmits signals used by eCPRI [156] or Radio over Ethernet (RoE) [157] directly over Ethernet or optionally over UDP/IP protocols.

In the S-plane either or both Precision Time Protocol (PTP) and Synchronous Ethernet (SyncE) work on top of Ethernet protocol.

Finally, in the M-plane, signals are transmitted through the NETwork CONFiguration (NETCONF) protocol [158], over TCP/IP networks.

6.2 Need for synchronization

Wireless telecommunication technologies have completely transformed over the past two decades. Voice traffic is no longer dominating bandwidth demand. Data now vastly dominates the traffic. Moreover, speed requirements are rapidly growing to support faster content download with video streaming at increasing resolutions. Globally, there is a growing trend in widely varying applications to move towards packet-switched networks which are ideal for carrying data at high speed. Ethernet has vastly proliferated over the last few years and it has become the preferred data transport mechanism, not only because of its universal adoption but also because of the lower costs associated with it.

One characteristic of packet-switched networks (such as Ethernet) is that they operate asynchronously, therefore they cannot interact with synchronous networks. However, many services require synchronization. For example LTE base stations which use Time Division Duplexing (TDD) require accurate time synchronization because the carrier radio frequency for the base station must be within the allocated spectrum and remote control services require low latency. With the emerging 5G standard, available bandwidth is increasing, latency is going down, and new services are being introduced that are driving tighter synchronization requirements. With the transition from TDD to packet-switched networks, the need to provide synchronization over a packet network become a necessity.

IEEE Std 1588-2008, also known as Precision Time Protocol [159] is becoming the main protocol to transport precise time, phase and frequency over packet networks and it has been adopted by O-RAN specification for the S-plane protocol stack.

6.2.1 Precision Time Protocol

The Precision Time Protocol (PTP) is a message-based transfer protocol for distributing precise time, phase and frequency synchronization across packet networks (Ethernet networks). It was introduced in the IEEE 1588-2002 standard and evolved in a new version, called PTPv2, which is addressed in the IEEE 1588-2008 [159]. PTP defines an exchange of timed messages over packet networks, ensuring the various points in the network to be precisely synchronized to the reference master clock so that the network meets specific performance limits according to the network's application.

The PTP standard describes a hierarchical master-slave architecture for timing distribution. Under this architecture, a time distribution system, depicted in Fig. 6.3, consists of a communication network and one or more clock devices. Here, the master is the provider of time, already synchronized to a Primary Reference Time Clock (PRTC) or being itself a PRTC (a GPS-capable device

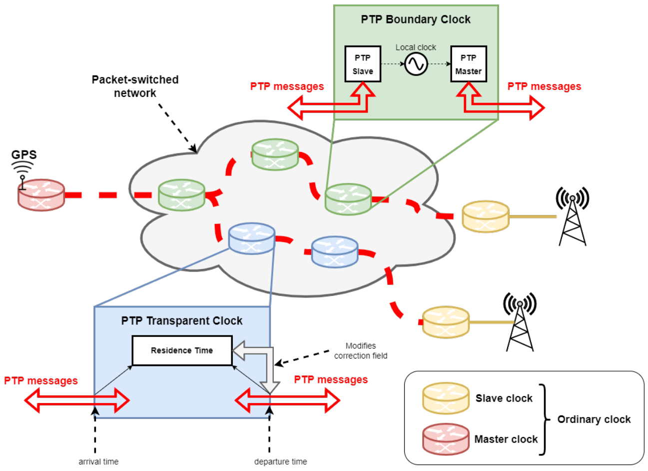

Figure 6.3: PTP framework.

as for instance), and the slaves synchronize to the master through the exchange of PTP messages. The precise time a packet passes an ingress or egress point of a PTP-aware device is recorded using *timestamps*. Master and slave network devices (referred to as *Ordinary Clocks* (OC) in PTP specification) are kept synchronized by the transmission of these timestamps sent within the PTP messages. Because packets take different lengths of time to travel through the network - caused by queuing in switches and routers on the path - this results in a Packet Delay Variation (PDV). To reduce the impact of PDV, PTP defines *Boundary Clock* (BC) and *Transparent Clock* (TC) that can be used to meet the target accuracy of the network. While OCs are PTP-aware single-port devices that can be a master or a slave clock, BCs are PTP-aware multi-port devices that can be a master or a slave clock. They calibrate themselves by recovering and regenerating the PTP timing from the previous clock in the chain and uses their (synchronized) local clock to drive a new PTP master function (see Fig. 6.3). TC is a PTP-aware multi-port device that is not master or slave clock, but a bridge between the two. They forward and correct all PTP messages by adding the residence time in the node into a correction field within the header of the message. At the end slave, the value of the correction field represents the total delay in each of the switches along the route. Both these devices make use of *hardware timestamps*. With hardware timestamps, when messages depart or arrive at a PTP-aware device port, special hardware generates a timestamp from the local clock (see Fig. 6.4), usually in the Media-Independent Interface (MII) between the MAC and the PHY. This removes the unpredictably slow response of the operating system and other software in generating timestamps.

PTP timing messages, containing the hardware timestamps, are carried within packet payload and can be transported over several protocols where

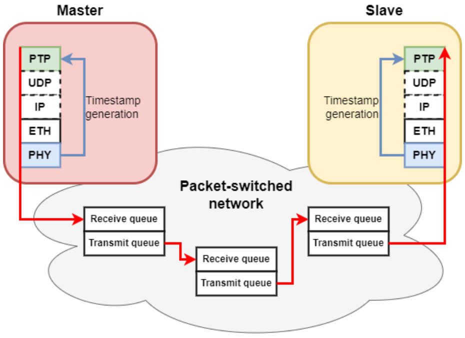

Figure 6.4: Hardware timestamps generation.

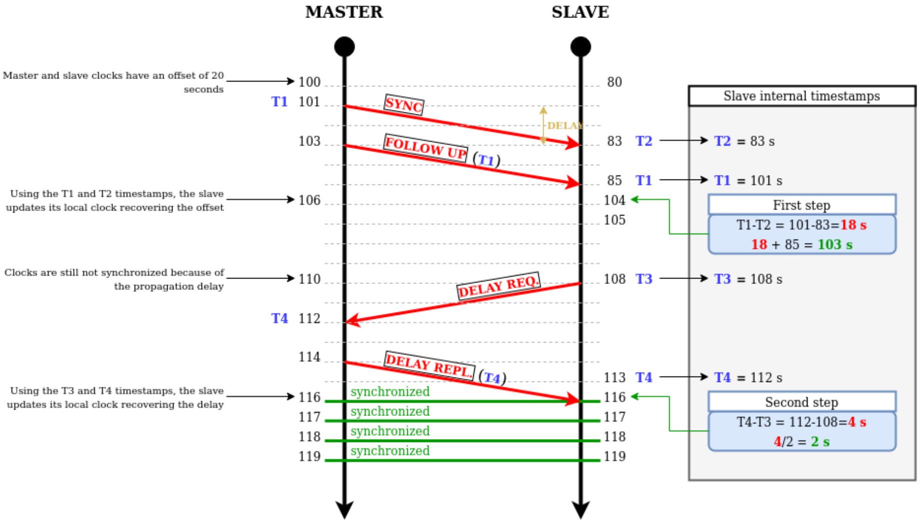

Figure 6.5: PTP steps taken to synchronize the slave clock to that of the master ("two-steps" operation mode).

the main ones are UDP over IPv4, UDP over IPv6 and Ethernet. There are two types of PTP messages: *Event Messages* and *General Messages*. Event messages are timed messages whereby an accurate timestamp is generated at both transmission and receipt of the message. General messages do not require timestamps but may contain timestamps for their associated event message. Fig. 6.5 shows a PTP use case to provide time synchronization between slave and master devices. In this example, the slave clock starts with an offset of 20 time units (seconds as for instance) with respect to master. Note that of course such values are just for explanation purposes and they do not represent the effective network performance. The master and slave PTP clocks configured for end-to-end delay mechanism use the following PTP messages (as defined in the ITU-T G.8275.1 profile [160]): Sync, Follow Up, Delay Request and Delay

Response.

- The master clock sends a Sync message to the slave and registers the transmit timestamp (T1);
- The slave clock receives the Sync message and registers the receive timestamp (T2);
- The slave clock receives a Follow Up message from the master clock with timestamp (T1);

After this first sequence, the slave can use the two stored timestamps to recover the initial offset from master. Now, it must measure and correct the propagation delay:

- The slave clock sends a Delay Request message to the master clock and registers the timestamp (T3) when the packet was sent.
- The master clock receives the Delay Request message from the slave clock and registers the received timestamp (T4).
- The master clock conveys to the given slave clock the timestamp T4 by embedding the timestamp into a Delay Response message.
- The slave clock receives a Delay Response message from the master clock with timestamp (T4).

After this sequence, the slave possesses all four timestamps that can be used to compute the offset of the slave relative to the master and the propagation time between the two clocks. Such offset calculation is based on the assumption that the uplink and downlink propagation times are the same which is not actually the real scenario. However, as explained above, the use of hardware timestamps remove the PDV issue.

6.2.2 PTP Profiles

IEEE 1588-2008 offers a very flexible framework as it does not prescribe use cases or target any specific application either, allowing for very different ways of using the protocol. The application of the protocol for the specific use case is within the domain of the corresponding standard body, such as ITU-T. To facilitate enforcing network architecture and limitations, and in order to achieve performance targets, PTP introduces the concept of *PTP Profiles*.

A PTP profile is a set of required options, prohibited options, ranges and defaults of configurable attributes aimed at supporting a given application. The purpose of a PTP profile is to allow organizations to define specific selections of attribute values and optional features of PTP aimed at supporting a given set of applications. Since such profiles are intended to either allow or forbid a number of PTP features, these are not interoperable with each other as they offer different performance levels and involve different requirements for the network. Typical profiles are:

- Default profiles, defined in IEEE 1588-2008;
- Power profiles (IEEE C37.238-2011);
- Enterprise profiles, currently and IETF draft;
- Telecom profiles.

In the context of *Telecom profiles*, ITU-T is in charge to develop recommendations relative to architecture and requirements for packet-based time, phase and frequency distribution. ITU-T is split into a number of Study Groups, including the SG15 responsible for transport standardization and it sets up a number of working groups called Questions (Q) that focus on different topics. Q13 is responsible for time, phase and frequency distribution through three PTP Telecom profiles:

- **ITU-T G.8265.1**: PTP Telecom profile for frequency;
- **ITU-T G.8275.1**: PTP Telecom profile for time and phase with full timing support from the network;
- **ITU-T G.8275.2**: PTP Telecom profile for time and phase with partial timing support from the network.

ITU-T G.8275.1 Profile

ITU-T Recommendation G.8275.1 defines the "Precision time protocol telecom profile for phase/time synchronization with full timing support from the network" [160]. It defines the options and attributes from IEEE 1588-2008 to be used to deliver phase/time synchronization to the end application.

This recommendation allows for proper network operation for phase and time synchronization distribution through PTP when network equipment, Telecom BC (T-BC) or Telecom Time Slave clock (T-TSC), is timed from another T-BC or a Telecom Grandmaster clock (T-GM). It addresses only the distribution of phase and time synchronization with the full timing support architecture as defined in ITU-T G.8275, therefore non-participant devices, that is devices that only forward PTP packets (non-PTP-aware devices), are not allowed. In addition, Telecom TC (T-TC) are not considered for this profile. Only T-BC with hardware timestamping at the related interfaces are allowed. Moreover, in this profile the use of Synchronous Ethernet (SyncE), defined in ITU-T G.8262 [161], is mandatory. SyncE is a physical layer technology that uses the bit

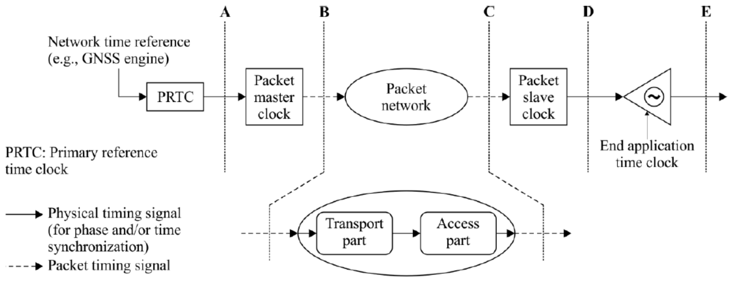

Figure 6.6: ITU-T G.8275.1 network reference model [160].

clock of the Ethernet physical layer to provide frequency synchronization from a traceable PRTC. T-BCs must be syntonized by such frequency reference. This type of support is expected to provide phase/time holdover capacities, enabling phase/time local reference to be maintained during periods of failure of the phase and time distribution protocol.

Fig. 6.6 describes the network reference model used to define the time and phase synchronization performance objectives. A packet master clock function in a T-GM clock device, having access to a reference timing signal compliant with a PRTC, originates the packet timing distribution. It provides timing to all other devices of the network and it does not synchronize its local clock with any other network element other than the PRTC. The T-BC synchronizes its local clock to a T-GM or an upstream T-BC, and provides timing information to downstream T-BCs or T-TSCs. If, at a given point in time, there are no higher-quality clocks available to a T-BC to synchronize to, it may act as a T-GM. The timing distribution ends to a packet slave clock, corresponding to a T-TSC, which is in charge to provide synchronization to the end application. The T-TSC synchronizes its local clock to another PTP clock (in most cases, the T-BC), and does not provide synchronization through PTP to any other device. ITU-T G.8275.1 profile classifies the applications into classes of requirements, according to the level of accuracy as reported in Table 6.1. In this work the class of accuracy is set to 6A (260 ns).

In addition to the timing distribution interfaces, needed to connect PTP devices in the distribution chain, T-GM, T-BC and T-TSC are also equipped with measurement interfaces. In order to allow network operators to measure the quality of the phase/time synchronization distributed along the synchronization chain, each PRTC, T-GM, T-BC and T-TSC must have a dedicated external phase/time output interface implemented. A one pulse-per-second (1PPS) interface is an adequate measurement interface, and should be implemented according to one of the interfaces specified in Annex A of [162].

Finally, this profile was developed for phase/time synchronization and therefore it needs to measure the propagation delay, in order to do that the use of

Table 6.1: Time and phase requirement classes

Class	**Maximum relative time error**
1	500 ms
2	100-500 μs
3	5 μs
4	1.5 μs
5	1 μs
6A	260 ns
6B	130 ns
6C	65 ns

two-steps time transfer mode is mandatory (see Fig. 6.5).

6.3 ZCU111 FPGA Project

To provide solutions for their networks, operators need to draw upon a broad range of radio hardware. Equipment manufacturers desire scalable and flexible platform solutions to minimize design effort, cost and time-to-market. Scalability also helps to minimize test time and inventory, and maximize design reuse. Scalable platform solutions are also advantageous because they allow operators to quickly adopt to changing standards and to the evolving performance requirements characteristic of modern wireless communications.

Field Programmable Gate Arrays (FPGA) and System on Chip (SoC), that is the integration of a number of CPU cores inside an FPGA, with the characteristics of dynamic reprogrammability and the ability to perform at higher rates, are convenient solutions for designing various building blocks of RANs' architecture. The possibility of reprogramming the FPGAs means that even after the circuit has been designed and implemented, FPGAs can still be modified, updated, and completely change its functionality to perform a completely different task than before, reducing the efforts and costs required for the long-term maintenance of these chips. Reprogrammability makes them the perfect choice for prototyping purposes, allowing to perform test runs by manipulating the programming and determining the ideal configuration on one chip only. Even after the product has been finalized, developed, and delivered, updates and adaptations can be carried out directly at the customer. Moreover, FPGAs can perform processing and calculation at a faster rate since algorithms and processing are embedded into the hardware and designed in parallel. This also makes them ideal for real-time processing.

For these reasons, FPGAs and SoC have become a very attractive solution in telecommunication field providing flexible, cost-effective and scalable plat-

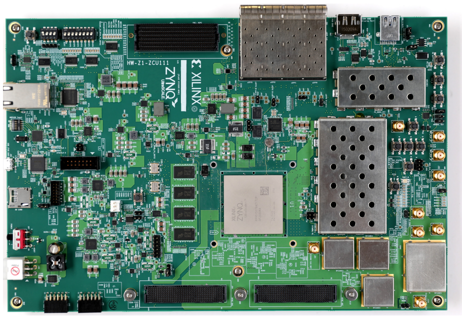

(a) ZCU111 evaluation board.

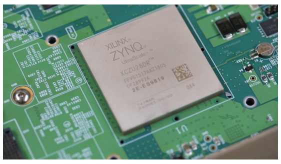

(b) Zynq UltraScale+ RFSoC FPGA.

Figure 6.7: Xilinx ZCU111 evaluation board (6.7a) and the Zynq UltraScale+ RFSoC FPGA installed (6.7b).

form, along with reduced time-to-market. In particular, Multi-Processor SoCs (MPSoC), which combine a powerful processing system (PS) and programmable logic (PL) in the same device, enable heterogeneous (software and hardware) multi-processing features.

In this work it is presented an FPGA implementation of the Synchronization Plane for an O-RAN-compliant RU. The objective is to achieve time synchronization through the PTP protocol on an O-RU according to the ITU-T G.8275.1 Telecom profile, outlined in the previous section.

6.3.1 Setup description

The target O-RU under test, to be synchronized, is developed through the ZCU111 Xilinx evaluation board, depicted in Fig. 6.7a. The ZCU111 evaluation board is equipped with many of the common board-level features needed for design development, such as DDR4 memory, networking interfaces, FMC expansion ports, PS MIO peripherals, JTAG, USB and Ethernet ports, SD card interface, leds, buttons and so on. The key component is the FPGA, which is a Zynq UltraScale+ (US+) RFSoC [163] (differing by the integration of DAC/ADC components from traditional MPSoC), shown in Fig. 6.7b. The PS side features the ARM Cortex A53 64-bit quad-core processor and Cortex-R5 dual-core real-time processor.

The complete setup is shown in Fig. 6.8. An external T-GM clock, which acts as the root of timing reference and already synchronized with the International

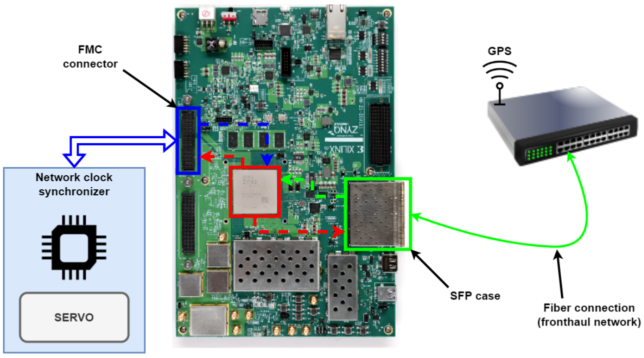

Figure 6.8: Project setup.

Atomic Time (TAI), is connected through a fiber segment (the fronthaul) to the ZCU111 evaluation board, which acts as a T-TSC. The T-GM gives the correct Time of Day (ToD) to the O-RU, which must align its internal ToD to such reference via PTP. Such T-GM is a common Ethernet switch, equipped with a GPS which provides synchronization to the TAI. Finally, a second third-party chip is installed on the ZCU111 evaluation board and acts as a network synchronizer clock for the T-TSC operation, compliant with ITU-T G.8275.1 Telecom profile. This T-TSC is also compliant with ITU-T G.8262 specification [161], as indicated in the relative datasheets, for SyncE operation. Such chip is mounted on a FPGA Mezzanine Card (FMC) plugged onto the ZCU111 FMC connector.

To summarize, taking into account both Fig. 6.6 and Fig. 6.8: the Ethernet switch operates as a packet master clock (T-GM), already synchronized with the PRTC reference clock (through GPS); it synchronizes the packet slave clock (T-TSC) by sending PTP messages through the fronthaul network (the fiber). The T-TSC, integrated in the O-RU (the ZCU111 board), is in charge to give the correct time and phase reference to the radio (the end application time clock indicated in Fig. 6.6).

6.3.2 FPGA design description

All O-RU functionalities implementing the Split Option 7-2x (the Low-PHY section of Fig. 6.1) in the Zynq US+ RFSoC FPGA have been designed with the Vivado Suite, which is a software tool produced by Xilinx for synthesis and analysis of Hardware Description Language (HDL) designs and SoC development. After the FPGA design has been developed by writing the relative HDL code, Vivado converts this high-level description in a synthesized netlist, which is a digital gate-level description. Finally, it places this logical gate description in the FPGA by generating the relative bitstream. The bitstream is a file that contains the programming information for an FPGA. The design is written in

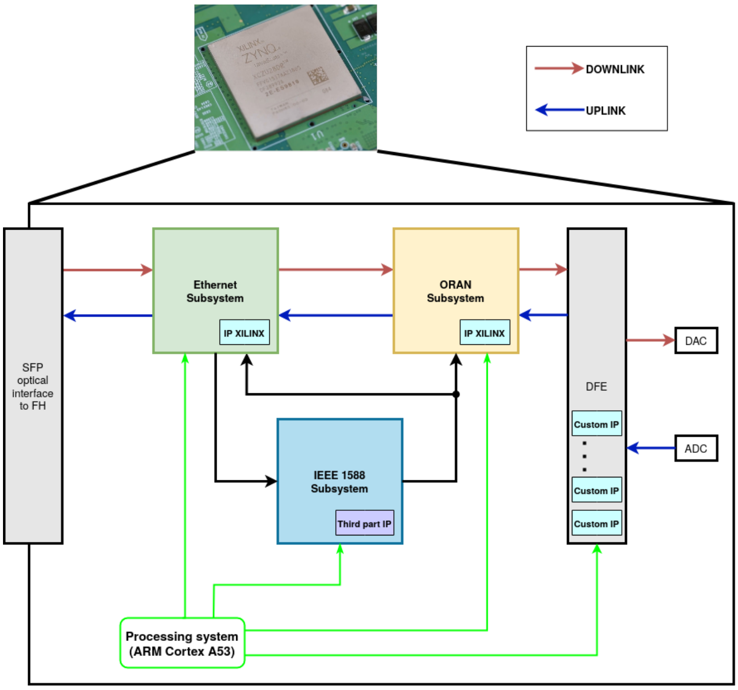

Figure 6.9: O-RU FPGA design: the optical interface to the fronthaul (FH) on the left is the SFP interface for fiber connection to the O-DU; the DFE block on the right is the signal processing chain for transmitting/receiving signal to/from the radio interface.

VHDL language, which is an HDL that can model the behavior and structure of digital systems at multiple levels of abstraction, ranging from the system level down to that of logic gates.

The high-level view of the FPGA project is shown in Fig. 6.9. The CU planes of O-RAN specification are handled by the *Ethernet Subsystem* and *ORAN Subsystem*, and they are out of the scope of this work. The ethernet subsystem implements the 10G/25G MAC layer with a Physical Coding Sublayer (PCS) and Physical Medium Attachment (PMA) operation as specified by the IEEE 802.3 [164]. It receives the fronthaul traffic from the O-DU through the SFP case where a fiber segment is connected to. The serial I/Q downlink flow coming from the SFP is converted into a data stream to be sent to the ORAN subsystem, which is in charge to handle the CU-plane to be transmitted to the radio interface through the Digital Front End (DFE). On the other side, the uplink radio signal is received and sent to the DFE which performs the reversed operations backwards. Both Ethernet and ORAN subsystems take timing reference from the *IEEE 1588 subsystem*, described in the next subsection.

All the above mentioned blocks are implemented in the PL. However, it is

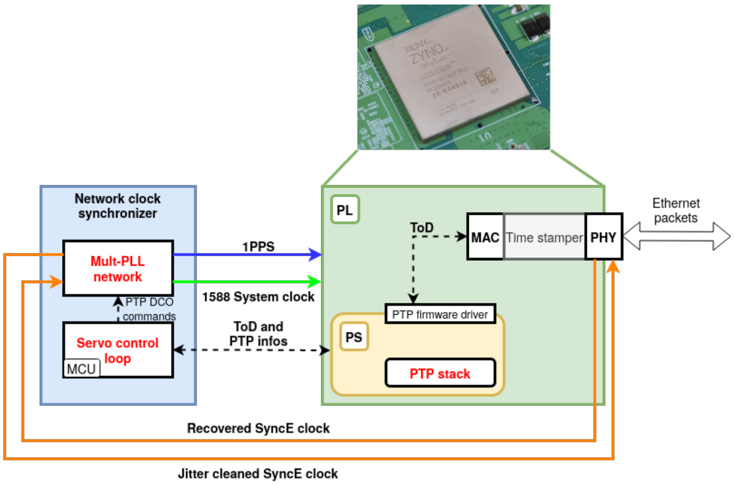

Figure 6.10: Synchronization architecture design.

useful to have access to such blocks for configuration and monitoring purposes through the PS. The operating system running on the ARM Cortex A53 CPU is based on Linux kernel, particularly suitable for embedded system and SoC, known as *Petalinux*. PL and PS are interconnected through the AXI interface [165], which is a parallel, high-performance and synchronous, communication interface, designed for on-chip communication. The AXI interface allows the OS to have access to configuration and status registers of PL blocks.

6.3.3 S-plane design description

The focus of this work is on the synchronization aspects of the O-RU under test. The detailed description of the synchronization-related part is shown in Fig. 6.10. It consists of three components highlighted in red: the IEEE 1588 protocol stack (*PTP stack*); a packet synchronizer servo algorithm (*servo control loop*); a network synchronizer clock (*multi-PLL network*). The third-party chip installed on the ZCU111 integrates the servo control loop and multi-PLL network, while the PTP stack is running on top of the Petalinux OS inside the FPGA and interacts with hardware components through its driver (the firmware), which has been developed in C language.

The synchronizer clock offers a number of PLLs that can be independently configured and controlled through the serial SPI interface to generate some reference clocks, such as the 1588 system clock, which drives the PTP subsystem, and a 1 Hz clock to support 1PPS. Such clocks are generated by this multi-PLL network and steered by the servo through DCO-controlled PTP commands. Moreover, it recovers the SyncE clock from the PHY removing jitter and wander issues, for physical support from the network in compliance with ITU-T

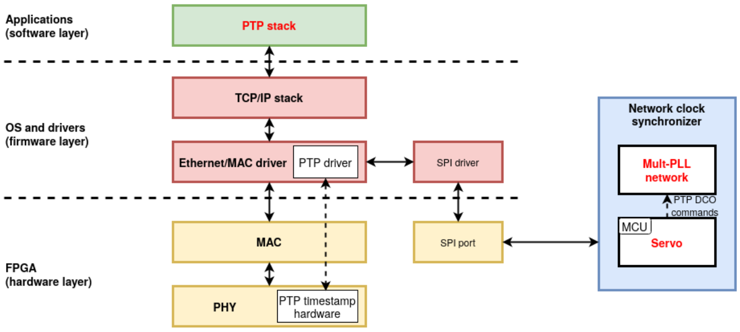

Figure 6.11: Synchronization architecture layers.

G.8275.1.

The PTP stack receives Ethernet packets from the MAC layer implemented in the FPGA, processes PTP packets and sends timestamp data to the servo algorithm (implemented in an integrated MCU within the third-party chip) through SPI commands. Based on these, the servo algorithm is used to steer the frequency and phase of the 1588 system clock and 1PPS clock that runs the timestamper unit in the Ethernet PHY, which maintains the ToD. Based on 1PPS clock adjustment, the timestamper is driven to align to the master ToD. The PTP firmware interfaces the hardware with the software stack where PTP events are processed and then passed to the servo control loop over a SPI port driver as shown in Fig. 6.11.

6.3.4 Synchronization results

There is more than one way to test the quality of time synchronization and each approach provides different information. There are three approaches for testing time synchronization: software testing, 1PPS signal comparison, and output clock comparison.

Software testing relies on the results reported by the PTP stack to show the quality of the time synchronization by giving the time offset between the ToD of the local equipment (T-TSC) and the master TAI. When analyzing software results the reported error is always taken just before the time synchronization. Since the process is reporting an error that is essentially due to the drift between two clocks, the software error represents a worst case picture of the average time synchronization.

The most common way to analyze time synchronization comes from looking at the 1PPS signal. It is a very easy way of assessing the accuracy of synchronization, given also the fact that all PTP-aware devices in the network should be equipped with an output 1PPS test interface. The primary limit to this measurement is that this effectively samples the error every second.

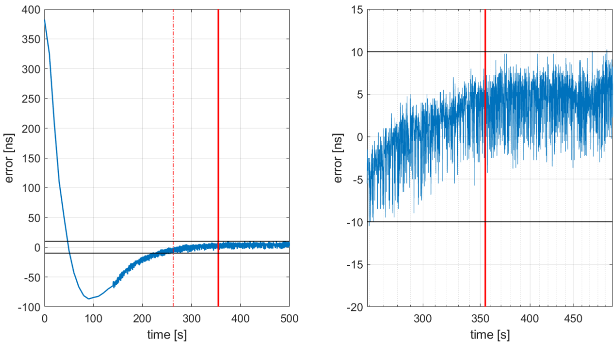

Figure 6.12: Software test results of O-RU synchronized to T-GM. The right plot is a zoomed view after the dashed, red line of the left plot.

The most accurate method to measure clock synchronization is set both the master and slave to generate a clock output at a known frequency and then compare those two clock signals. This provides the error at many more times a second, allowing a more accurate view of the time synchronization. As an additional benefit, the clock output can be handled through an analog output that will not add additional synchronization error.

In this primary test work, we assessed the quality of time synchronization considering the first two approaches.

Software reported results

Fig. 6.12 represents a typical plot of the clock synchronization error, as reported by the software, between the T-GM and the O-RU under test when they are synchronized. On the y-axis it is reported the ToD offset between the local equipment (T-TSC) and the T-GM, while in the x-axis it is reported the test timeline, about 8 minutes long. The black lines set the absolute threshold within which the O-RU is considered synchronized to the master T-GM, that is: ToD offset $\leq |10|$ns. Considering time applications of class 6A reported in Table 6.1, requirements are largely met. At the beginning of the test, the ToD offset is very high (370 ns), so the software applies very large time corrections. After this initial 'large-scale synchronization', it starts applying smaller corrections. From Fig. 6.12 it is clear the error minimization mechanism. The software is in a *not synchronized* state until it reaches the threshold value, occurring after 4 minutes (indicated by the dashed, red line in Fig. 6.12). Here, the software state switch into a *synchronizing* state until the ToD is locked to that of the master, occurring after 6 minutes (indicated by the solid, red line in Fig. 6.12). After this the O-RU is in *synchronized state.* Fig. 6.13 describes the statistical values of ToD offset when the target O-RU is in the synchronized state. Results

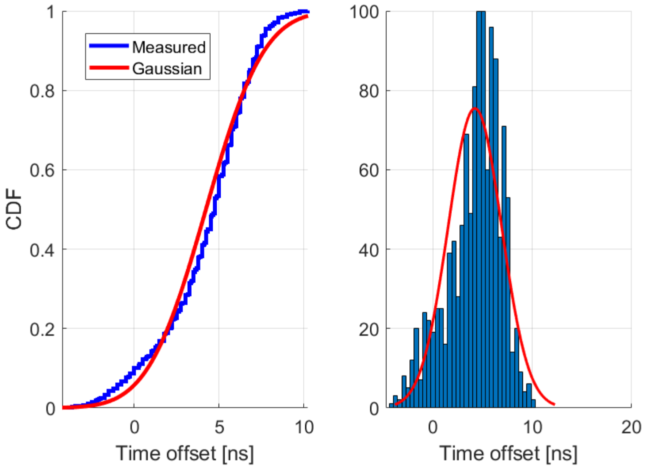

Figure 6.13: Cumulative Distribution Function (CDF), on the left) and histogram fitted by a scaled normal density function (on the right), for ToD offset in synchronization state.

shows a mean value of 4.2258 ns with a standard deviation of 2.6840 ns, which is an excellent achievement.

1PPS test results

Testing the 1PPS signal time synchronization was achieved by analyzing the 1PPS signals from both the T-GM and T-TSC devices. Fig. 6.14 represents a typical histogram plot of the 1PPS output signal comparison between the master and slave devices when they are time synchronized. The clock to clock synchronization is within a 1.3077 ns standard deviation and a mean difference of only 5.0676. This performance represents a significant starting point for further development in future works.

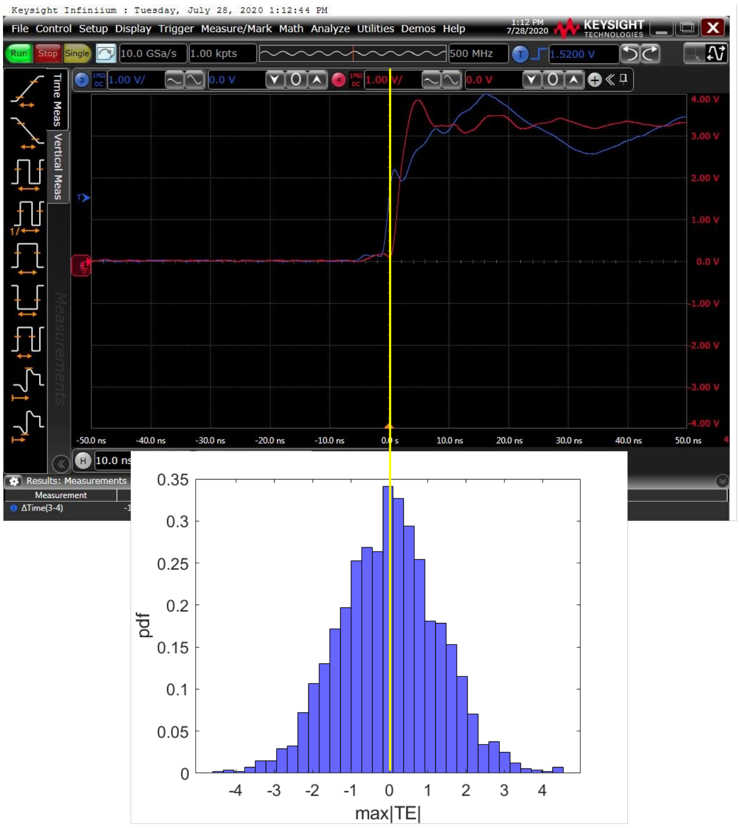

Figure 6.14: Histogram of offset values between master and slave 1PPS clocks; the histogram is center-aligned with an oscilloscope screenshot, showing the alignment of the two 1PPS signals.

Conclusions

IMT-2020 technologies are envisioned to enable a networked society, where information can be accessed and shared anywhere and anytime, by anyone and anything. 5G systems are expected to boost the performance of current wireless mobile networks, not only in terms of throughput and capacity, but also in latency, reliability, scalability and connectivity. The background and the context in which the forthcoming 5G technologies are emerging have been outlined in chapter 1, along with the International Telecommunication Union vision, which embraces the Enhanced Mobile Broadband, Massive Machine Type Communications and Ultra-Reliable and Low-Latency Communications scenarios. In order to support the different usage scenarios, along with the current and future trends, 3GPP is developing a flexible and scalable 5G physical layer aiming at an unified and more capable air interface whose elements are briefly described in chapter 1.

One of the principal 5G enabling technology is the exploitation of millimeter wave spectrum, which is outlined in chapter 2 with its properties and advantages. The primary motivation for using mmWave spectrum is its ability to provide extremely high data rates due to the large bandwidth available. However, the higher isotropic path loss and exposure to shadowing set more stringent limits on coverage. The mmWave channel is highly time-variant due to the higher Doppler spread and, in combination with the higher exposure to shadowing and blockage, is often intermittent and discontinuous. Moreover, at mmWave frequencies the channel has a quasi-optical behavior, being often spatially sparser and more specular. Since such characteristics differ a lot from those of the sub-6 GHz spectrum, it is important to develop new radio channel models which include the new challenges and requirements. In particular, ray-based radio channel models, such as Ray-Tracing described in chapter 2, are drawing attention with respect to conventional stochastic models, due to their qualities as frequency-agility, scenario-independence and spatial consistency.

Map-based models rely on the digital description of the environment referring to both geometrical and electromagnetic properties. Therefore, the knowledge of the electromagnetic properties of construction materials is crucial for the design of future wireless systems. In chapter 3 it is presented a new simple and fast technique for the characterization of low-loss materials based on the Fabry-Pérot resonance. Instead of performing multiple measurements, a wide measurement bandwidth is used to extract the same information using a very simple setup. This is an important feature since common materials are often heterogeneous compounds, exhibiting large variability between different samples and an accurate characterization is hardly possible. Rather than accuracy, simplicity and speed of execution are important features. Such method has been developed, assessed and validated throughout the chapter 3. Different setups, including a portable spectrum analyzer for on-site measurements have been used to show the flexibility of the method. Results achieved with a VNA are compared with those obtained from a light, portable and easy-to-use measurement kit. The comparison shows a good agreement between the two measurement chains. The combination of the simplicity of the method with the portability of the second kit, is an interesting solution for on-field electromagnetic characterization of different materials. Interesting results for several different common use materials have been obtained at several mmWave and sub-THz frequencies at which the method appears quite suitable. The method provides reliable results if applied to materials that can be considered relatively homogeneous; for grainy materials such as sandstone or chipboard, grains must be significantly smaller than the wavelength in order to prevent severe diffuse scattering from hampering Fabry-Pérot resonance. Future works target the evaluation of the complex relative permittivity, through the proposed Fabry-Pérot method, of various materials for which there is still no or few literature at mmWave frequencies.

Thanks to the knowledge of both the electromagnetic characteristics of different items, directional simulations of both indoor and outdoor environments have been performed at two frequencies of interest for 5G: 27GHz and 38 GHz. In chapter 4 it is also reported the measurement campaign carried out at the University of Bologna, with the objective of investigating the large-scale spatial characteristics of both indoor and outdoor channels. Here, a comparison between simulation results and measured data has been accomplished, achieving good Ray-Tracing predictions. After the validation of the predicted results by simulation, Ray-Tracing is used to get an idea of the principal propagation mechanisms at mmWave frequencies. Results shows that reflection is the main propagation mechanism for NLOS receivers, being always above the 60% in indoor scenario. Scattering has a major contribution for deep NLOS reveivers (the RX7 in indoor scenario as for instance). For LOS receivers almost the 100% of the received power comes from the direct ray. For outdoor scenario instead, reflection is important also for LOS receivers. Here diffraction has a higher impact with respect to the indoor case, and also scattering is important for NLOS receivers as well. The work described in this thesis set the basis for future activities targeting the evaluation of Ray-Tracing as a real-time prediction channel tool to assist future beamforming techniques, known as RT-assisted beamforming, which rely on the map-based channel model to perform real-time prediction of the channel's directional characteristics.

Another consequence of reduced coverage due to the higher frequencies is that, already starting from LTE systems, cellular networks have been evolving towards pico- and femto-cell heterogeneous networks. In 5G systems, network densification sets an increase in costs and consumptions, as mobile operators must deploy many more mmWave small cells than LTE in order to achieve similar wide-area coverage. In chapter 5 the challenges the current C-RAN architectures are facing, especially for the higher bandwidths requirements, have been outlined leading to the concept of functional split. Moreover, current CPRI-based C-RAN suffer from various limitation set by the forthcoming 5G systems. Among these, the CPRI protocol is not anymore suitable for fronthaul networks extended in the range of kms. In addition, CPRI does not deliver a full interface standardization that would allow a true interoperability among different vendors and do not sufficiently prescribe specification for fronthaul interfaces.

For these reasons, new advanced Open RAN specifications have been proposed to overcome the bandwidths problem and to enable multi-vendor RAN. O-RAN specification prescribes Control, User, Synchronization and Management planes. In chapter 6 it is described the FPGA project of the O-RAN Synchronization Plane for a target Remote Unit, based on the new O-RAN functional split specifications and ITU-T G.8275.1 Telecom Profile. The complete setup and the working principles are outlined in detail. The objective is to achieve time synchronization between a master reference clock and a target slave clock by means of the Precision Time Protocol. Results show a good synchronization design, with a mean time error between the master and slave clock of only 5.1 ns and a 1.31 standard deviation. This achievement represent an important starting point for the next work on Control and User planes.

Bibliography

[1] Cisco. *Cisco Visual Networking Index: Global Mobile Data Traffic Forecast Update, 2017–2022.* 2019. URL: `https://s3.amazonaws.com/media.mediapost.com/uploads/CiscoForecast.pdf`.

[2] George R. MacCartney and Theodore S. Rappaport. "73 GHz millimeter wave propagation measurements for outdoor urban mobile and backhaul communications in New York City". In: (2014), pp. 4862–4867. DOI: `10.1109/ICC.2014.6884090`.

[3] Afif Osseiran et al. "The Foundation of the Mobile and Wireless Communications System for 2020 and Beyond: Challenges, Enablers and Technology Solutions". In: (2013), pp. 1–5. DOI: `10.1109/VTCSpring.2013.6692781`.

[4] Jeffrey G. Andrews et al. "What Will 5G Be?" In: *IEEE Journal on Selected Areas in Communications* 32.6 (2014), pp. 1065–1082. DOI: `10.1109/JSAC.2014.2328098`.

[5] Zekeriyya Esat Ankarali, Berker Peköz, and Hüseyin Arslan. "Flexible Radio Access Beyond 5G: A Future Projection on Waveform, Numerology, and Frame Design Principles". In: *IEEE Access* 5 (2017), pp. 18295–18309. DOI: `10.1109/ACCESS.2017.2684783`.

[6] Caner Kilinc et al. "New Radio 5G User Plane Design Alternatives: One 5G Air Interface Framework Supporting Multiple Services and Bands". In: (2016), pp. 1–6. DOI: `10.1109/GLOCOMW.2016.7848970`.

[7] ITU-R. *IMT Vision – Framework and overall objectives of the future development of IMT for 2020 and beyond.* Recommendation ITU-R M.2083-0. International Telecommunication Union, 2015.

[8] ITU-R. *Guidelines for evaluation of radio interface technologies for IMT-2020.* Report ITU-R M.2412-0. International Telecommunication Union, 2017.

[9] ITU-R. *Minimum requirements related to technical performance for IMT-2020 radio interface(s).* Report ITU-R M.2410-0. International Telecommunication Union, 2017.

[10] ITU-R. *Detailed specifications of the terrestrial radio interfaces of International Mobile Telecommunications-Advanced (IMT Advanced).* Recommendation ITU-R M.2012. International Telecommunication Union, 2012.

[11] Xi Zhang et al. "On the Waveform for 5G". In: *IEEE Communications Magazine* 54.11 (2016), pp. 74–80. DOI: `10.1109/MCOM.2016.1600337CM`.

[12] ETSI. *5G; NR; User Equipment (UE) radio transmission and reception; Part 1: Range 1 Standalone.* Technical Specification 38.101-1. European Telecommunications Standards Institute, 2018.

[13] ETSI. *5G; NR; User Equipment (UE) radio transmission and reception; Part 2: Range 2 Standalone.* Technical Specification 38.101-2. European Telecommunications Standards Institute, 2018.

[14] ETSI. *5G; NR; Physical channels and modulation.* Technical Specification 38.211. European Telecommunications Standards Institute, 2018.

[15] Taewon Hwang et al. "OFDM and Its Wireless Applications: A Survey". In: *IEEE Transactions on Vehicular Technology* 58.4 (2009), pp. 1673–1694. DOI: `10.1109/TVT.2008.2004555`.

[16] ETSI. *5G; NR; Physical layer; General description.* Technical Specification 38.201. European Telecommunications Standards Institute, 2018.

[17] Ali A. Zaidi et al. "Waveform and Numerology to Support 5G Services and Requirements". In: *IEEE Communications Magazine* 54.11 (2016), pp. 90–98. DOI: `10.1109/MCOM.2016.1600336CM`.

[18] Ali A. Zaidi et al. "OFDM Numerology Design for 5G New Radio to Support IoT, eMBB, and MBSFN". In: *IEEE Communications Standards Magazine* 2.2 (2018), pp. 78–83. DOI: `10.1109/MCOMSTD.2018.1700021`.

[19] Xingqin Lin et al. "5G New Radio: Unveiling the Essentials of the Next Generation Wireless Access Technology". In: *IEEE Communications Standards Magazine* 3.3 (2019), pp. 30–37. DOI: `10.1109/MCOMSTD.001.1800036`.

[20] Gerard J. Foschini. "Layered space-time architecture for wireless communication in a fading environment when using multi-element antennas". In: *Bell Labs Technical Journal* 1.2 (1996), pp. 41–59. DOI: `10.1002/bltj.2015`.

[21] G.J. Foschini et al. "Analysis and performance of some basic space-time architectures". In: *IEEE Journal on Selected Areas in Communications* 21.3 (2003), pp. 303–320. DOI: `10.1109/JSAC.2003.809456`.

[22] N. Chiurtu, B. Rimoldi, and E. Telatar. “On the capacity of multi-antenna Gaussian channels”. In: *Proceedings. 2001 IEEE International Symposium on Information Theory (IEEE Cat. No.01CH37252).* 2001, pp. 53–. DOI: `10.1109/ISIT.2001.935916`.

[23] T.L. Marzetta and B.M. Hochwald. “Capacity of a mobile multiple-antenna communication link in Rayleigh flat fading”. In: *IEEE Transactions on Information Theory* 45.1 (1999), pp. 139–157. DOI: `10.1109/18.746779`.

[24] A. Goldsmith et al. “Capacity limits of MIMO channels”. In: *IEEE Journal on Selected Areas in Communications* 21.5 (2003), pp. 684–702. DOI: `10.1109/JSAC.2003.810294`.

[25] Shu Sun et al. “Mimo for millimeter-wave wireless communications: beamforming, spatial multiplexing, or both?” In: *IEEE Communications Magazine* 52.12 (2014), pp. 110–121. DOI: `10.1109/MCOM.2014.6979962`.

[26] David J. Love et al. “An overview of limited feedback in wireless communication systems”. In: *IEEE Journal on Selected Areas in Communications* 26.8 (2008), pp. 1341–1365. DOI: `10.1109/JSAC.2008.081002`.

[27] Theodore S. Rappaport et al. *Millimeter wave wireless communications.* Jan. 2014.

[28] Erik Dahlman, Stefan Parkvall, and Johan Skold. *5G NR: the next generation wireless access technology.* Sept. 2020.

[29] Farooq Khan and Zhouyue Pi. “mmWave mobile broadband (MMB): Unleashing the 3–300GHz spectrum”. In: (May 2011). DOI: `10.1109/SARNOF.2011.5876482`.

[30] Philip Pietraski et al. “Millimeter Wave and Terahertz Communications: Feasibility and Challenges”. In: *ZTE communications* 10 (2012), pp. 3–12.

[31] Sooyoung Hur et al. “Millimeter Wave Beamforming for Wireless Backhaul and Access in Small Cell Networks”. In: *IEEE Transactions on Communications* 61.10 (2013), pp. 4391–4403. DOI: `10.1109/TCOMM.2013.090513.120848`.

[32] Samsung. *Samsung announces worlds first 5G mmwave mobile technology.* 2013. URL: `https://news.samsung.com/global/samsung-announces-worlds-first-5g-mmwave-mobile-technology`.

[33] Jannat Laskar et al. “The next wireless wave is a millimeter wave”. In: *Microwave Journal* 50 (Aug. 2007), pp. 22–32.

[34] Salam Akoum, Omar Ayach, and Robert Heath. “Coverage and capacity in mmWave cellular systems”. In: Nov. 2012, pp. 688–692. ISBN: 978-1-4673-5050-1. DOI: `10.1109/ACSSC.2012.6489099`.

[35] Theodore S. Rappaport et al. "Millimeter Wave Mobile Communications for 5G Cellular: It Will Work!" In: *IEEE Access* 1 (2013), pp. 335–349. DOI: `10.1109/ACCESS.2013.2260813`.

[36] Federico Boccardi et al. "Five disruptive technology directions for 5G". In: *IEEE Communications Magazine* 52.2 (2014), pp. 74–80. DOI: `10.1109/MCOM.2014.6736746`.

[37] Dennis Roddy. *Satellite Communications.* 2006.

[38] Jonas Hansryd et al. "Non-line-of-sight microwave backhaul for small cells". In: *Ericsson Review* (2013).

[39] NGMN Alliance. *Small Cell Backhaul Requirements.* 2012. URL: `https://ngmn.org/wp-content/uploads/NGMN_Whitepaper_Small_Cell_Backhaul_Requirements.pdf`.

[40] Theodore S. Rappaport, James N. Murdock, and Felix Gutierrez. "State of the Art in 60-GHz Integrated Circuits and Systems for Wireless Communications". In: *Proceedings of the IEEE* 99.8 (2011), pp. 1390–1436. DOI: `10.1109/JPROC.2011.2143650`.

[41] Eldad Perahia et al. "IEEE 802.11ad: Defining the Next Generation Multi-Gbps Wi-Fi". In: *2010 7th IEEE Consumer Communications and Networking Conference.* 2010, pp. 1–5. DOI: `10.1109/CCNC.2010.5421713`.

[42] Robert C. Daniels et al. "60 GHz Wireless: Up Close and Personal". In: *IEEE Microwave Magazine* 11.7 (2010), pp. 44–50. DOI: `10.1109/MMM.2010.938581`.

[43] ITU-R. *Calculation of free-space attenuation.* Recommendation ITU-R P.525-4. International Telecommunication Union, 2019.

[44] Franco Fuschini et al. "Item level characterization of mm-wave indoor propagation". In: *EURASIP Journal on Wireless Communications and Networking* 2016 (2016), pp. 1–12.

[45] Hang Zhao et al. "28 GHz millimeter wave cellular communication measurements for reflection and penetration loss in and around buildings in New York city". In: *2013 IEEE International Conference on Communications (ICC).* 2013, pp. 5163–5167. DOI: `10.1109/ICC.2013.6655403`.

[46] C.R. Anderson and T.S. Rappaport. "In-building wideband partition loss measurements at 2.5 and 60 GHz". In: *IEEE Transactions on Wireless Communications* 3.3 (2004), pp. 922–928. DOI: `10.1109/TWC.2004.826328`.

[47] Zhouyue Pi and Farooq Khan. "An introduction to millimeter-wave mobile broadband systems". In: *IEEE Communications Magazine* 49.6 (2011), pp. 101–107. DOI: `10.1109/MCOM.2011.5783993`.

[48] Jonathan Lu et al. "Modeling Human Blockers in Millimeter Wave Radio Links". In: *ZTE Communications Magazine* 2012 (Dec. 2012), pp. 23–28.

[49] ITU-R. *Multipath propagation and parameterization of its characteristics.* Recommendation ITU-R P.1407-6. International Telecommunication Union, 2017.

[50] Wei Fan et al. "Measured wideband characteristics of indoor channels at centimetric and millimetric bands". In: *EURASIP Journal on Wireless Communications and Networking* 58 (2016). DOI: `10.1186/s13638-016-0548-x`.

[51] Katsuyuki Haneda. "Channel Models and Beamforming at Millimeter-Wave Frequency Bands". In: *IEICE Transactions on Communications* E98.B (May 2015), pp. 755–772. DOI: `10.1587/transcom.E98.B.755`.

[52] Jonas Medbo et al. "Directional channel characteristics in elevation and azimuth at an urban macrocell base station". In: *2012 6th European Conference on Antennas and Propagation (EUCAP).* 2012, pp. 428–432. DOI: `10.1109/EuCAP.2012.6206081`.

[53] Theodore S. Rappaport et al. "Broadband Millimeter-Wave Propagation Measurements and Models Using Adaptive-Beam Antennas for Outdoor Urban Cellular Communications". In: *IEEE Transactions on Antennas and Propagation* 61.4 (2013), pp. 1850–1859. DOI: `10.1109/TAP.2012.2235056`.

[54] Stephan Hafner et al. "Characterisation of Channel Measurements at 70GHz in Indoor Femtocells". In: vol. 2015. May 2015, pp. 1–5. DOI: `10.1109/VTCSpring.2015.7145739`.

[55] Andreas Richter. "Estimation of Radio Channel Parameters: Models and Algorithms". Ph.D thesis. Technische Universität Ilmenau, 2005.

[56] Diego Dupleich et al. "Directional characterization of the 60 GHz indoor-office channel". In: *2014 XXXIth URSI General Assembly and Scientific Symposium (URSI GASS).* 2014, pp. 1–4. DOI: `10.1109/URSIGASS.2014.6929648`.

[57] Katsuyuki Haneda et al. "A Statistical Spatio-Temporal Radio Channel Model for Large Indoor Environments at 60 and 70 GHz". In: *IEEE Transactions on Antennas and Propagation* 63.6 (2015), pp. 2694–2704. DOI: `10.1109/TAP.2015.2412147`.

[58] J. Medbo et al. "Channel modelling for the fifth generation mobile communications". In: *The 8th European Conference on Antennas and Propagation (EuCAP 2014).* 2014, pp. 219–223. DOI: `10.1109/EuCAP.2014.6901730`.

[59] Christina Larsson, Bengt-Erik Olsson, and Jonas Medbo. "Angular Resolved Pathloss Measurements in Urban Macrocell Scenarios at 28 GHz". In: *2016 IEEE 84th Vehicular Technology Conference (VTC-Fall)*. 2016, pp. 1–5. DOI: `10.1109/VTCFall.2016.7880907`.

[60] Sana Salous et al. "Millimeter-Wave Propagation: Characterization and modeling toward fifth-generation systems. [Wireless Corner]". In: *IEEE Antennas and Propagation Magazine* 58.6 (2016), pp. 115–127. DOI: `10.1109/MAP.2016.2609815`.

[61] Wonil Roh et al. "Millimeter-wave beamforming as an enabling technology for 5G cellular communications: theoretical feasibility and prototype results". In: *IEEE Communications Magazine* 52.2 (2014), pp. 106–113. DOI: `10.1109/MCOM.2014.6736750`.

[62] Erik G. Larsson et al. "Massive MIMO for next generation wireless systems". In: *IEEE Communications Magazine* 52.2 (2014), pp. 186–195. DOI: `10.1109/MCOM.2014.6736761`.

[63] Fredrik Rusek et al. "Scaling Up MIMO: Opportunities and Challenges with Very Large Arrays". In: *IEEE Signal Processing Magazine* 30.1 (2013), pp. 40–60. DOI: `10.1109/MSP.2011.2178495`.

[64] Sylvain Ranvier, Suiyan Geng, and Pertti Vainikainen. "Mm-wave MIMO systems for high data-rate mobile communications". In: *2009 1st International Conference on Wireless Communication, Vehicular Technology, Information Theory and Aerospace Electronic Systems Technology*. 2009, pp. 142–146. DOI: `10.1109/WIRELESSVITAE.2009.5172439`.

[65] Eric Torkildson, Upamanyu Madhow, and Mark Rodwell. "Indoor Millimeter Wave MIMO: Feasibility and Performance". In: *IEEE Transactions on Wireless Communications* 10.12 (2011), pp. 4150–4160. DOI: `10.1109/TWC.2011.092911.101843`.

[66] Cheng-Xiang Wang et al. "Cellular architecture and key technologies for 5G wireless communication networks". In: *IEEE Communications Magazine* 52.2 (2014), pp. 122–130. DOI: `10.1109/MCOM.2014.6736752`.

[67] Zheng Ma et al. "Key techniques for 5G wireless communications: Network architecture, physical layer, and MAC layer perspectives". In: *Science China Information Sciences* 58 (Apr. 2015), pp. 1–20. DOI: `10.1007/s11432-015-5293-y`.

[68] A.S.Y. Poon, D.N.C. Tse, and R.W. Brodersen. "Impact of scattering on the capacity, diversity, and propagation range of multiple-antenna channels". In: *IEEE Transactions on Information Theory* 52.3 (2006), pp. 1087–1100. DOI: `10.1109/TIT.2005.864478`.

[69] Christopher L. Holloway et al. “An Overview of the Theory and Applications of Metasurfaces: The Two-Dimensional Equivalents of Metamaterials”. In: *IEEE Antennas and Propagation Magazine* 54.2 (2012), pp. 10–35. DOI: `10.1109/MAP.2012.6230714`.

[70] Syed S. Bukhari, J (Yiannis) Vardaxoglou, and William Whittow. “A Metasurfaces Review: Definitions and Applications”. In: *Applied Sciences* 9.13 (2019). ISSN: 2076-3417. DOI: `10.3390/app9132727`. URL: `https://www.mdpi.com/2076-3417/9/13/2727`.

[71] Y. Okumura. “Field strength and its variability in VHF and UHF land-mobile radio service”. In: *Rev. Electr. Commun. Lab.* 16 (1968), pp. 825–873. URL: `https://ci.nii.ac.jp/naid/10010001461/en/`.

[72] R. H. Clarke. “A statistical theory of mobile-radio reception”. In: *The Bell System Technical Journal* 47.6 (1968), pp. 957–1000. DOI: `10.1002/j.1538-7305.1968.tb00069.x`.

[73] William C. Jakes. *Microwave Mobile Communications.* 1994.

[74] European Commission, general direction of information, and media society. *COST 207 : Digital land mobile radio communications.* Publications Office, 1990.

[75] J.P. Kermoal et al. “A stochastic MIMO radio channel model with experimental validation”. In: *IEEE Journal on Selected Areas in Communications* 20.6 (2002), pp. 1211–1226. DOI: `10.1109/JSAC.2002.801223`.

[76] A.F. Molisch. “A generic model for MIMO wireless propagation channels in macro- and microcells”. In: *IEEE Transactions on Signal Processing* 52.1 (2004), pp. 61–71. DOI: `10.1109/TSP.2003.820144`.

[77] George Calcev et al. “A Wideband Spatial Channel Model for System-Wide Simulations”. In: *IEEE Transactions on Vehicular Technology* 56.2 (2007), pp. 389–403. DOI: `10.1109/TVT.2007.891463`.

[78] ETSI. *Spatial channel model for Multiple Input Multiple Output (MIMO) simulations.* Technical Report 25.996. European Telecommunications Standards Institute, 2020.

[79] ITU-R. *Guidelines for evaluation of radio interface technologies for IMT-Advanced.* Report ITU-R M.2135-1. International Telecommunication Union, 2009.

[80] ETSI. *Study on 3D channel model for LTE.* Technical Report 36.873. European Telecommunications Standards Institute, 2018.

[81] Jonas Medbo et al. “Radio propagation modeling for 5G mobile and wireless communications”. In: *IEEE Communications Magazine* 54.6 (2016), pp. 144–151. DOI: `10.1109/MCOM.2016.7498102`.

[82] METIS. *METIS Channel Models.* Deliverable D1.4. Mobile and wireless communications Enablers for the Twenty-twenty Information Society, 2015.

[83] ITU-R. *Technical feasibility of IMT in bands above 6 GHz.* Report ITU-R M.2376-0. International Telecommunication Union, 2015.

[84] Aalto University et al. *White paper on 5G Channel Model for bands up to100 GHz.* 2015. URL: `http://www.5gworkshops.com/2016/5G_Channel_Model_for_bands_up_to100_GHz(2015-12-6).pdf`.

[85] Xiang Gao et al. "Massive MIMO Performance Evaluation Based on Measured Propagation Data". In: *IEEE Transactions on Wireless Communications* 14 (July 2015), pp. 1–1. DOI: `10.1109/TWC.2015.2414413`.

[86] Pekka Kyösti et al. "IST-4-027756 WINNER II D1.1.2 v1.2 WINNER II channel models". In: *Inf. Soc. Technol* 11 (Feb. 2008).

[87] Lingfeng Liu et al. "The COST 2100 MIMO channel model". In: *IEEE Wireless Communications* 19 (Dec. 2012), pp. 92–99. DOI: `10.1109/MWC.2012.6393523`.

[88] ETSI. *Study on channel model for frequencies from 0.5 to 100 GHz.* Technical Report 38.901. European Telecommunications Standards Institute, 2018.

[89] K Haneda et al. *Cooperative Radio Communications for Green Smart Environments - COST Action IC1004.* Jan. 2016, pp. 71–119. ISBN: 9788793379152.

[90] NIST. *5G mmWave channel model alliance.* 2017. URL: `https://www.nist.gov/ctl/nextg-channel-model-alliance`.

[91] FP7-ICT-608637-MiWEBA. *Millimetre-wave evolution for backhaul and access.* 2015. URL: `https://cordis.europa.eu/project/id/608637`.

[92] H2020-ICT-671650-mmMAGIC. *mm-Wave based mobile radio access network for 5G integrated communications.* 2017. URL: `https://cordis.europa.eu/project/id/671650`.

[93] Ming Xiao et al. "Millimeter Wave Communications for Future Mobile Networks". In: *IEEE Journal on Selected Areas in Communications* 35.9 (2017), pp. 1909–1935. DOI: `10.1109/JSAC.2017.2719924`.

[94] Kan Zheng, Suling Ou, and Xuefeng Yin. "Massive MIMO channel models: A survey". In: *International Journal of Antennas and Propagation* 2014 (June 2014), pp. 1–10. DOI: `10.1155/2014/848071`.

[95] S.Y. Seidel and T.S. Rappaport. "Site-specific propagation prediction for wireless in-building personal communication system design". In: *IEEE Transactions on Vehicular Technology* 43.4 (1994), pp. 879–891. DOI: `10.1109/25.330150`.

[96] Huan Cong Nguyen et al. “Evaluation of Empirical Ray-Tracing Model for an Urban Outdoor Scenario at 73 GHz E-Band”. In: *2014 IEEE 80th Vehicular Technology Conference (VTC2014-Fall)*. 2014, pp. 1–6. DOI: `10.1109/VTCFall.2014.6965971`.

[97] Enrico Maria Vitucci et al. “Ray Tracing RF Field Prediction: An Unforgiving Validation”. In: *International Journal of Antennas and Propagation* 2015 (2015), pp. 1–11.

[98] Franco Fuschini et al. “Ray tracing propagation modeling for future small-cell and indoor applications: A review of current techniques”. In: *Radio Science* 50.6 (2015), pp. 469–485. DOI: `10.1002/2015RS005659`.

[99] Leonardo Possenti et al. “Transmission loss evaluation for Fabry-Perot materials’ characterization”. In: *2020 14th European Conference on Antennas and Propagation (EuCAP)*. 2020, pp. 1–5. DOI: `10.23919/EuCAP48036.2020.9136075`.

[100] L. Possenti et al. “E.M. Characterization of Common Construction Materials Using the Fabry-Pérot resonance method”. In: *2019 International Symposium on Antennas and Propagation (ISAP)*. 2019, pp. 1–3.

[101] L. Possenti et al. “Improved Fabry-Pérot Electromagnetic Material Characterization: Application and Results”. In: *Radio Science* 55 (Nov. 2020). DOI: `10.1029/2020RS007164`.

[102] Klaus David and Hendrik Berndt. “6G Vision and Requirements: Is There Any Need for Beyond 5G?” In: *IEEE Vehicular Technology Magazine* 13.3 (2018), pp. 72–80. DOI: `10.1109/MVT.2018.2848498`.

[103] Ali A. Zaidi. “Designing for the future: the 5G NR physical layer”. In: *Ericsson Technology Review* (2017).

[104] Theodore S. Rappaport et al. “Wireless Communications and Applications Above 100 GHz: Opportunities and Challenges for 6G and Beyond”. In: *IEEE Access* 7 (2019), pp. 78729–78757. DOI: `10.1109/ACCESS.2019.2921522`.

[105] Sana Salous et al. “Millimeter-wave propagation characterization and modelling towards 5G systems”. English. In: *IEEE Antennas and Propagation Magazine* 58.6 (Dec. 2016), pp. 115–127. ISSN: 1045-9243. DOI: `10.1109/MAP.2016.2609815`.

[106] A.-H. Boughriet, C. Legrand, and A. Chapoton. “Noniterative stable transmission/reflection method for low-loss material complex permittivity determination”. In: *IEEE Transactions on Microwave Theory and Techniques* 45.1 (1997), pp. 52–57. DOI: `10.1109/22.552032`.

[107] Antoni Josep Canós Marín et al. “Improvement in the Accuracy of Dielectric Measurement of Open-Ended Coaxial Resonators by an Enhanced De-Embedding of the Coupling Network”. In: *IEEE Transactions on Microwave Theory and Techniques* 61.12 (2013), pp. 4636–4645. DOI: `10.1109/TMTT.2013.2285359`.

[108] T.M. Hirvonen et al. “Measurement of dielectrics at 100 GHz with an open resonator connected to a network analyzer”. In: *IEEE Transactions on Instrumentation and Measurement* 45.4 (1996), pp. 780–786. DOI: `10.1109/19.516996`.

[109] C.N. Works, T.W. Dakin, and F.W. Boggs. “A Resonant-Cavity Method for Measuring Dielectric Properties at Ultra-High Frequencies”. In: *Proceedings of the IRE* 33.4 (1945), pp. 245–254. DOI: `10.1109/JRPROC.1945.233876`.

[110] D.K. Ghodgaonkar, V.V. Varadan, and V.K. Varadan. “A free-space method for measurement of dielectric constants and loss tangents at microwave frequencies”. In: *IEEE Transactions on Instrumentation and Measurement* 38.3 (1989), pp. 789–793. DOI: `10.1109/19.32194`.

[111] J. Baker-Jarvis, E.J. Vanzura, and W.A. Kissick. “Improved technique for determining complex permittivity with the transmission/reflection method”. In: *IEEE Transactions on Microwave Theory and Techniques* 38.8 (1990), pp. 1096–1103. DOI: `10.1109/22.57336`.

[112] Paolo Corona, Giuseppe Ferrara, and Claudio Gennarelli. “A new technique for free-space permittivity measurements of lossy dielectrics”. In: *IEEE Transactions on Instrumentation and Measurement* IM-36.2 (1987), pp. 560–563. DOI: `10.1109/TIM.1987.6312740`.

[113] Vittorio Degli-Esposti et al. “A Method for the Electromagnetic Characterization of Construction Materials Based on Fabry–Pérot Resonance”. In: *IEEE Access* 5 (2017), pp. 24938–24943. DOI: `10.1109/ACCESS.2017.2767278`.

[114] W. Burnside and K. Burgener. “High frequency scattering by a thin lossless dielectric slab”. In: *IEEE Transactions on Antennas and Propagation* 31.1 (1983), pp. 104–110. DOI: `10.1109/TAP.1983.1143019`.

[115] SAF Tehnika. URL: `https://www.saftehnika.com/`.

[116] S. Stavrou and S.R. Saunders. “Review of constitutive parameters of building materials”. In: *Twelfth International Conference on Antennas and Propagation, 2003 (ICAP 2003). (Conf. Publ. No. 491).* Vol. 1. 2003, 211–215 vol.1. DOI: `10.1049/cp:20030052`.

[117] Arthur R. Von Hippel. *Dielectric Materials and Applications.* 1966.

[118] ITU-R. *Effects of Building Materials and Structures on Radiowave Propagation above about 100 MHz.* Standard ITU-R P.2040. International Telecommunication Union, 2015.

[119] Jonathan R. Abel and Jon W. Wallace. “4-40 GHz Permittivity Measurements of Indoor Building Materials”. In: *2019 IEEE International Symposium on Antennas and Propagation and USNC-URSI Radio Science Meeting.* 2019, pp. 105–106. DOI: `10.1109/APUSNCURSINRSM.2019.8888911`.

[120] Mohammed Nurul Afsar. “Precision millimeter-wave measurements of complex refractive index, complex dielectric permittivity, and loss tangent of common polymers”. In: *IEEE Transactions on Instrumentation and Measurement* IM-36.2 (1987), pp. 530–536. DOI: `10.1109/TIM.1987.6312733`.

[121] Isam Alawneh, Jan Barowski, and Ilona Rolfes. “Measuring the Permittivity of Dielectric Materials by Using 140 GHz FMCW Radar Sensor”. In: *2019 13th European Conference on Antennas and Propagation (EuCAP).* 2019, pp. 1–4.

[122] Tianying Chang, Xiansheng Zhang, and Xiaoxuan Zhang. “Accurate determination of dielectric permittivity of polymers from 75 GHz to 16 THz using both S-parameters and transmission spectroscopy: publisher’s note”. In: *Applied Optics* 57 (July 2018), p. 6032. DOI: `10.1364/AO.57.006032`.

[123] David Ferreira et al. “A review on the electromagnetic characterisation of building materials at micro- and millimetre wave frequencies”. In: *The 8th European Conference on Antennas and Propagation (EuCAP 2014).* 2014, pp. 145–149. DOI: `10.1109/EuCAP.2014.6901713`.

[124] Behnam Ghassemiparvin and Nima Ghalichechian. “Permittivity and dielectric loss measurement of paraffin films for mmW and THz applications”. In: *2016 International Workshop on Antenna Technology (iWAT).* 2016, pp. 48–50. DOI: `10.1109/IWAT.2016.7434797`.

[125] Hirokazu Kawabata et al. “Multi-Frequency Measurements of Complex Permittivity of Dielectric Plates using Higher-Order Modes of a Balanced-Type Circular Disk Resonator”. In: *2006 European Microwave Conference.* 2006, pp. 388–391. DOI: `10.1109/EUMC.2006.281355`.

[126] Alireza Kazemipour et al. “Design and Calibration of a Compact Quasi-Optical System for Material Characterization in Millimeter/Submillimeter Wave Domain”. In: *IEEE Transactions on Instrumentation and Measurement* 64.6 (2015), pp. 1438–1445. DOI: `10.1109/TIM.2014.2376115`.

[127] Jerzy Krupka. "Measurements of the Complex Permittivity of Low Loss Polymers at Frequency Range From 5 GHz to 50 GHz". In: *IEEE Microwave and Wireless Components Letters* 26.6 (2016), pp. 464–466. DOI: `10.1109/LMWC.2016.2562640`.

[128] V. Degli-Esposti. "A diffuse scattering model for urban propagation prediction". In: *IEEE Transactions on Antennas and Propagation* 49.7 (2001), pp. 1111–1113. DOI: `10.1109/8.933491`.

[129] E. M. Vitucci et al. "A Study on Dual-Directional Mm-wave Indoor Channel Characteristics". In: *2019 13th European Conference on Antennas and Propagation (EuCAP)*. 2019, pp. 1–5.

[130] Vittorio Degli-Esposti et al. "Ray-Tracing-Based mm-Wave Beamforming Assessment". In: *IEEE Access* 2 (2014), pp. 1314–1325. DOI: `10.1109/ACCESS.2014.2365991`.

[131] Aleksandra Checko et al. "Cloud RAN for Mobile Networks—A Technology Overview". In: *IEEE Communications Surveys Tutorials* 17.1 (2015), pp. 405–426. DOI: `10.1109/COMST.2014.2355255`.

[132] CPRI Consortium. *CPRI Specification V7.0 Common Public Radio Interface (CPRI)*. Interface Specification. Common Public Radio Interface Consortium, 2015.

[133] *Open Base Station Architecture Initiative*. BTS System Reference Document Version 2.0. Common Public Radio Interface Consortium, 2006.

[134] ETSI. *Open Radio equipment Interface (ORI); Requirements for Open Radio equipment Interface (ORI)*. Group Specification. European Telecommunications Standards Institute, 2014.

[135] Ming Ding et al. "Will the Area Spectral Efficiency Monotonically Grow as Small Cells Go Dense?" In: Dec. 2015, pp. 1–7. DOI: `10.1109/GLOCOM.2015.7416981`.

[136] Yonghua Lin. "Wireless network cloud: Architecture and system requirements". In: *Ibm Journal of Research and Development* 54 (Jan. 2010).

[137] Ian F. Akyildiz et al. "5G roadmap: 10 key enabling technologies". In: *Comput. Networks* 106 (2016), pp. 17–48.

[138] Gianluca Camillo Valastro, Daniela Panno, and Salvatore Riolo. "A SDN/NFV based C-RAN architecture for 5G Mobile Networks". In: *2018 International Conference on Selected Topics in Mobile and Wireless Networking (MoWNeT)*. 2018, pp. 1–8. DOI: `10.1109/MoWNet.2018.8428882`.

[139] Mamta Agiwal, Abhishek Roy, and Navrati Saxena. "Next Generation 5G Wireless Networks: A Comprehensive Survey". In: *IEEE Communications Surveys Tutorials* 18.3 (2016), pp. 1617–1655. DOI: `10.1109/COMST.2016.2532458`.

[140] China Mobile Research Institute. *C-RAN: The Road Towards Green RAN,* 2011.

[141] Conor Sexton et al. “5G: Adaptable Networks Enabled by Versatile Radio Access Technologies”. In: *IEEE Communications Surveys Tutorials* 19.2 (2017), pp. 688–720. DOI: `10.1109/COMST.2017.2652495`.

[142] Line M. P. Larsen, Aleksandra Checko, and Henrik L. Christiansen. “A Survey of the Functional Splits Proposed for 5G Mobile Crosshaul Networks”. In: *IEEE Communications Surveys Tutorials* 21.1 (2019), pp. 146–172. DOI: `10.1109/COMST.2018.2868805`.

[143] Tukmanov Anvar et al. “Fronthauling for 5G and beyond”. In: *Access, Fronthaul and Backhaul Networks for 5G and Beyond.* 2017.

[144] Anil Umesh et al. “Special Articles on 5 G Standardization Trends Toward 2020 5 G Radio Access Network Standardization Trends Radio”. In: 2017.

[145] Jay Kant Chaudhary et al. “C-RAN Employing xRAN Functional Split: Complexity Analysis for 5G NR Remote Radio Unit”. In: *2019 European Conference on Networks and Communications (EuCNC).* 2019, pp. 580–585. DOI: `10.1109/EuCNC.2019.8801953`.

[146] SCF. *Small cell virtualization functional splits and use cases.* Technical Report TR-06-2015. Small Cell Forum, 2015.

[147] NGMN. *Further study on critical C-RAN technologies.* Technical Report TR-03-2015. next generation mobile networks, 2015.

[148] IEEE. *IEEE 1914.1-2019 - IEEE Standard for Packet-based Fronthaul Transport Networks.* IEEE Std 1914.1. Institute of Electrical and Electronics Engineers, 2020.

[149] ETSI. *5G; Study on new radio access technology.* Technical Report 38.912. European Telecommunications Standards Institute, 2017.

[150] 3GPP. *Study on new radio access technology: Radio access architecture and interfaces.* Technical Report 38.801. Third-Generation Partnership Project, 2017.

[151] ITU-T. *Transport network support of IMT-2020/5G.* Technical Report. International Telecommunication Union, 2018.

[152] NGMN Alliance. *5G End-to-End Architecture Framework.* Next Generation Mobile Networks Alliance, 2017.

[153] Yang Li and Sana Salous. “What to expect in next generation RAN architecture: A survey”. In: *2017 IEEE 17th International Conference on Communication Technology (ICCT).* 2017, pp. 427–431. DOI: `10.1109/ICCT.2017.8359675`.

[154] O-RAN Alliance. *O-RAN Architecture and Specifications.* 2021. URL: `https://www.o-ran.org/`.

[155] O-RAN Alliance. *Control, User and Synchronization Plane Specification.* ORAN-WG4.CUS.0-v02.00 Technical Specification. Open RAN Alliance, 2019.

[156] *Common Public Radio Interface: eCPRI Interface Specification.* Interface Specification V2.0. Ericsson AB, Huawei Technologies, NEC Corporation, Nokia, 2019.

[157] IEEE. *IEEE Standard for Radio over Ethernet Encapsulations and Mappings.* IEEE Std 1914.3. Institute of Electrical and Electronics Engineers, 2018.

[158] IETF. *Network Configuration Protocol (NETCONF).* RFC 6241. Internet Engineering Task Force (IETF), 2011.

[159] IEEE. *IEEE Standard for a Precision Clock Synchronization Protocol for Networked Measurement and Control Systems.* IEEE Std 1588-2008. Institute of Electrical and Electronics Engineers, 2008.

[160] ITU-T. *Precision time protocol telecom profile for phase/time synchronization with full timing support from the network.* G.8275.1/Y.1369.1. International Telecommunication Union Standardization sector, 2016.

[161] ITU-T. *Timing characteristics of synchronous Ethernet equipment slave clock.* G.8262/Y.1362. International Telecommunication Union Standardization sector, 2015.

[162] ITU-T. *Time and phase synchronization aspects of telecommunication networks.* G.8271/Y.1366. International Telecommunication Union Standardization sector, 2017.

[163] Xilinx. *ZCU111 Evaluation Board.* User Guide 1271 v1.2. Xilinx, 2018.

[164] IEEE. *IEEE Standard for Ethernet.* IEEE std 802.3-2018. Institute of Electrical and Electronics Engineers, 2018.

[165] Xilinx. *AXI Reference Guide.* User Guide 761 v13.1. Xilinx, 2011.